

# **Wind Tunnel Aeroacoustic Tests of Six Airfoils for Use on Small Wind Turbines**

**Period of Performance:  
August 23, 2002 through March 31, 2004**

Stefan Oerlemans  
*Nationaal Lucht-en Ruimtevaartlaboratorium  
National Aerospace Laboratory NLR  
Emmeloord, The Netherlands*



**NREL**

**National Renewable Energy Laboratory**  
1617 Cole Boulevard, Golden, Colorado 80401-3393  
303-275-3000 • [www.nrel.gov](http://www.nrel.gov)

Operated for the U.S. Department of Energy  
Office of Energy Efficiency and Renewable Energy  
by Midwest Research Institute • Battelle

Contract No. DE-AC36-99-GO10337

# Wind Tunnel Aeroacoustic Tests of Six Airfoils for Use on Small Wind Turbines

**Period of Performance:  
August 23, 2002 through March 31, 2004**

Stefan Oerlemans  
*Nationaal Lucht-en Ruimtevaartlaboratorium  
National Aerospace Laboratory NLR  
Emmeloord, The Netherlands*

NREL Technical Monitor: Paul Migliore

Prepared under Subcontract No. AAM-2-32237-01



**NREL**

**National Renewable Energy Laboratory**  
1617 Cole Boulevard, Golden, Colorado 80401-3393  
303-275-3000 • [www.nrel.gov](http://www.nrel.gov)

Operated for the U.S. Department of Energy  
Office of Energy Efficiency and Renewable Energy  
by Midwest Research Institute • Battelle

Contract No. DE-AC36-99-GO10337

## NOTICE

This report was prepared as an account of work sponsored by an agency of the United States government. Neither the United States government nor any agency thereof, nor any of their employees, makes any warranty, express or implied, or assumes any legal liability or responsibility for the accuracy, completeness, or usefulness of any information, apparatus, product, or process disclosed, or represents that its use would not infringe privately owned rights. Reference herein to any specific commercial product, process, or service by trade name, trademark, manufacturer, or otherwise does not necessarily constitute or imply its endorsement, recommendation, or favoring by the United States government or any agency thereof. The views and opinions of authors expressed herein do not necessarily state or reflect those of the United States government or any agency thereof.

Available electronically at <http://www.osti.gov/bridge>

Available for a processing fee to U.S. Department of Energy and its contractors, in paper, from:

U.S. Department of Energy  
Office of Scientific and Technical Information  
P.O. Box 62  
Oak Ridge, TN 37831-0062  
phone: 865.576.8401  
fax: 865.576.5728  
email: <mailto:reports@adonis.osti.gov>

Available for sale to the public, in paper, from:

U.S. Department of Commerce  
National Technical Information Service  
5285 Port Royal Road  
Springfield, VA 22161  
phone: 800.553.6847  
fax: 703.605.6900  
email: [orders@ntis.fedworld.gov](mailto:orders@ntis.fedworld.gov)  
online ordering: <http://www.ntis.gov/ordering.htm>



## Foreword

The U.S. Department of Energy (DOE), working through its National Renewable Energy Laboratory (NREL), is engaged in a comprehensive research effort to improve our understanding of wind turbine aeroacoustics. The motivation for this effort is the desire to exploit the large expanse of low wind speed sites that tend to be close to U.S. load centers. Quiet wind turbines are an inducement to widespread deployment, so the goal of NREL's aeroacoustic research is to develop tools that the U.S. wind industry can use in developing and deploying highly efficient, quiet wind turbines at low wind speed sites. NREL's National Wind Technology Center (NWTC) is implementing a multifaceted approach that includes wind tunnel tests, field tests, and theoretical analyses in direct support of low wind speed turbine development by its industry partners. NWTC researchers are working hand in hand with engineers in industry to ensure that research findings are available to support ongoing design decisions.

To that end, wind tunnel aerodynamic tests and aeroacoustic tests have been performed on six airfoils that are candidates for use on small wind turbines. Results are documented in two companion NREL reports:

*Wind Tunnel Aeroacoustic Tests of Six Airfoils for Use on Small Wind Turbines,*  
Stefan Oerlemans, Principal Investigator, the Netherlands National Aerospace Laboratory

*Wind Tunnel Aerodynamic Tests of Six Airfoils for Use on Small Wind Turbines,*  
Michael Selig, Principal Investigator, University of Illinois at Urbana-Champaign (UIUC)

These reports provide a valuable airfoil database for designers who wish to consider the airfoils tested<sup>1</sup>. But inevitably, designers will want to evaluate other airfoils that have not been tested. However, not only are wind tunnel tests expensive, it is also often difficult to schedule the facilities required within the overall time frame of a project development plan. This dilemma begs the question, "Is it really necessary to conduct wind tunnel tests, or can we rely on theoretical predictions?"

Predicting the aeroacoustic emission spectra of a particular airfoil shape is extremely difficult, but predicting the aerodynamic characteristics of a particular airfoil shape is routine practice. Nevertheless, there is always some uncertainty about the accuracy of the predictions in comparison to the results of wind tunnel tests or field performance, and there are questions about the efficacy of the two principal airfoil analysis methods: the Eppler and XFOIL codes. To address these related issues, at least in part, a theoretical analysis was commissioned of the same airfoils tested in the wind tunnel. The results are documented in the following NREL report:

*Theoretical Aerodynamic Analyses of Six Airfoils for Use on Small Wind Turbines Using Eppler and XFOIL Codes,*  
Dan M. Somers and Mark D. Maughmer, Principal Investigators, Airfoils, Incorporated

Possessing both theoretically predicted aerodynamic characteristics and wind tunnel test data for the same six airfoils provides an extraordinary opportunity to compare the performance, measured by energy capture, of wind turbine rotors designed with the different data. This will provide the insight needed to assist designers in deciding whether to pursue wind tunnel tests. Although some differences in the resulting blade planforms (chord and twist distributions) can be expected, a more important question relates to the difference in energy capture and its significance in driving the choices that need to be made during the preliminary design stage. These issues are addressed in a report that compares the differences in Eppler

---

<sup>1</sup> The extensive test data discussed in these reports are provided in electronic format on compact disks (CDs) included with the printed documents. The CDs may also be obtained by calling the NWTC library at 303-384-6963.

and XFOIL predictions to the UIUC wind tunnel tests and examines the planform and energy capture differences in resulting blade designs:

*Comparison of Optimized Aerodynamic Performance of Small Wind Turbine Rotors Designed with Theoretically Predicted versus Experimentally Measured Airfoil Characteristics,*  
Michael Selig, Principal Investigator, University of Illinois at Urbana-Champaign (UIUC)

Another research effort undertaken in support of the U.S. wind turbine industry involves a series of aeroacoustic field tests conducted at the NWTC. Using well documented, consistently applied test procedures, noise spectra were measured for eight small wind turbine configurations. Test results provide valuable information to manufacturers as well as potential users of these turbines. To our knowledge, this is the first comprehensive database of noise data for small wind turbines. The results of this effort are documented in another NREL report:

*Aeroacoustic Field Tests of Eight Small Wind Turbines,*  
J. van Dam and A. Huskey, Principal Investigators, NREL's National Wind Technology Center

Wind tunnel tests, field tests, and theoretical analyses provide useful information for development and validation of NREL's semi-empirical noise prediction code. This effort is described in the following NREL report:

*Semi-Empirical Aeroacoustic Noise Prediction Code for Wind Turbines,*  
Patrick Moriarty, Principal Investigator, NREL's National Wind Technology Center

The code will be continuously improved, but it may ultimately give way to more sophisticated, physics-based computational aeroacoustic codes also being developed by NREL

Each of the documents described above will be published as an NREL report. Undoubtedly, some results will also be presented in various journal articles or conference papers. All of the NREL reports will be available on NREL's web site at <http://www.nrel.gov/publications/>. Collectively, these reports represent a significant compendium of information on the aerodynamics and aeroacoustics of contemporary wind turbines. Therefore, NREL will also publish a CD-ROM containing these reports.

Clearly, this work represents a significant commitment of DOE resources as well as a significant commitment of personnel over an extended period. I am sure I express the sentiments of all the research participants in saying we sincerely hope the results of these efforts prove beneficial to the wind energy community.



Paul G. Migliore  
NREL/NWTC Project Manager

## Abstract

Aeroacoustic wind tunnel tests were performed of six airfoils that are candidates for use on small wind turbines. The acoustic measurements were done in NLR's Small Anechoic Wind Tunnel, for a range of wind speeds ( $U$ ) and angles of attack, with and without boundary layer tripping. Besides the airfoil self-noise measurements in a clean tunnel flow, the models were also tested with a turbulence grid in the nozzle, to investigate airfoil noise associated with inflow turbulence. A 48-microphone out-of-flow acoustic array was used to locate noise sources and to separate airfoil noise from extraneous wind tunnel noise. Besides the six candidate airfoils, one airfoil shape was tested for comparison to existing benchmark data. Before the acoustic tests, the tunnel flow was calibrated in terms of velocities, turbulence intensities, and flow angularity.

The acoustic results indicated that in a clean tunnel flow, trailing edge noise was dominant for all airfoils. In the untripped condition a number of airfoils exhibited intense tones that disappeared after proper tripping was applied. The broadband sound levels were found to scale with  $U^{4.5}$ . In case of inflow turbulence, leading-edge noise was dominant for all airfoils, and no difference was observed between the results with and without tripping. The inflow turbulence noise levels were found to scale with  $U^6$ . Comparison of the acoustic results for different airfoils indicated that inflow turbulence noise levels increased with increasing sharpness of the model leading edge. The directivity of both trailing edge and inflow turbulence noise appeared to be symmetrical around the model chord. Comparison with the benchmark data generally showed a good agreement in terms of spectral shape and levels, although for the tripped condition a discrepancy was observed at low frequencies, for which no clear explanation was found.

One model was tested with eight different Micro Electro Mechanical System (MEMS) simulators, mounted on the pressure side at 95% chord. Although the MEMS were found to have no effect on inflow turbulence noise, broadband trailing-edge noise levels increased by about 5 dB. In addition, the MEMS simulated by solid tabs produced very intense trailing-edge tones, the frequency of which was proportional to the tunnel speed. The directivity of the MEMS noise appeared to be symmetrical around the model chord.

Finally, it was found that a treatment of porous material in the gaps between model and endplates yielded a broadband extraneous noise reduction of up to 10 dB. As a result, the array could look much "deeper", which enabled the detection of very low trailing-edge noise levels.

# Table of Contents

<b>1</b>	<b>Introduction</b>	<b>1</b>
<b>2</b>	<b>Test Set-Up</b>	<b>2</b>
2.1	Small Anechoic Wind Tunnel KAT	2
2.2	Balance	2
2.3	Hot-wires	2
2.4	Microphone array	2
2.5	Models	2
2.6	MEMS	3
<b>3</b>	<b>Measurement And Processing Techniques</b>	<b>4</b>
3.1	Wind-tunnel parameters and balance	4
3.2	Hot-wires	4
3.3	Microphone array	5
	3.3.1 <i>Data acquisition</i>	5
	3.3.2 <i>Array processing</i>	5
	3.3.3 <i>Airfoil noise spectra</i>	5
	3.3.4 <i>Extraneous sources</i>	7
3.4	Measurement Program	7
	3.4.1 <i>Hot-wires</i>	7
	3.4.2 <i>Balance</i>	7
	3.4.3 <i>Microphone array</i>	7
<b>4</b>	<b>Tunnel Calibration</b>	<b>9</b>
<b>5</b>	<b>Airfoil Noise Results</b>	<b>10</b>
5.1	Introduction	10
5.2	Overview of acoustic results for different airfoils	11
	5.2.1 <i>Trailing-edge noise</i>	11
	5.2.2 <i>Inflow turbulence noise</i>	12
5.3	Dependence of airfoil noise levels on speed and angle-of-attack	12
	5.3.1 <i>Trailing-edge noise</i>	13
	5.3.2 <i>Inflow turbulence noise</i>	13
5.4	Pure tones and effect of boundary layer trips	14
5.5	Directivity	14

5.6	Comparison with benchmark data	15
5.7	Comparison of different airfoils	17
5.8	MEMS	17
	5.8.1 <i>Introduction</i>	17
	5.8.2 <i>Tones</i>	18
	5.8.3 <i>Directivity</i>	18
	5.8.4 <i>Inflow turbulence</i>	18
5.9	Corner noise reduction	19
<b>6</b>	<b>Summary and Conclusions</b>	<b>20</b>
<b>7</b>	<b>References</b>	<b>21</b>
	<b>Appendix 1. Test Matrix</b>	<b>91</b>

# 1 Introduction

The U.S. Department of Energy, working through its National Renewable Energy Laboratory (NREL), is engaged in a comprehensive research effort to improve the understanding of wind-turbine aeroacoustics. Motivation for this effort is the desire to exploit the large expanse of low-wind-speed sites that tend to be closer to load centers in the United States. Quiet wind turbines are an inducement to widespread deployment, and so the goal of NREL's aeroacoustic research is to develop tools for use by United States industry in developing and deploying highly efficient, quiet wind turbines at these low-wind-speed sites. NREL's National Wind Technology Center (NWTC) is implementing a multi-faceted approach that includes aerodynamic [1] and aeroacoustic wind-tunnel tests, field tests, and theoretical analyses in direct support of low-wind-speed turbine development by its industry partners.

This report describes aeroacoustic wind-tunnel tests of six airfoils that are candidates for use on small wind turbines. The tests were conducted in the Small Anechoic Wind Tunnel of the National Aerospace Laboratory (NLR) in the Netherlands. The acoustic measurements were done for a range of wind speeds and angles of attack with and without boundary layer tripping in order to assess the effect of blade contamination (e.g., dirt or insects) on the noise production. Besides the airfoil self-noise measurements in a clean tunnel flow, the models were also tested with a turbulence grid in the nozzle, to investigate airfoil noise associated with inflow turbulence. A 48-microphone out-of-flow acoustic array was used to locate noise sources and to separate airfoil noise from extraneous wind-tunnel noise.

Besides the six candidate airfoils, one airfoil shape (the National Advisory Committee for Aeronautics NACA 0012) was acoustically tested for comparison to existing benchmark data from the National Aeronautics and Space Administration (NASA). Furthermore, with cooperation and support from Lawrence Livermore National Laboratory (02-ERD-056) and the University of California at Davis, one model was tested with Micro Electro Mechanical System (MEMS) simulators. These measurements aimed to assess the aeroacoustic effect of these devices, which can be used on wind-turbine blades to improve the aerodynamic performance.

Before the acoustic tests, hot-wire measurements were done in the empty test section to determine the turbulence intensity and flow angularity, with and without turbulence grid. The lift characteristics of the different airfoils were measured using a balance.

## 2 Test Set-Up

### 2.1 Small Anechoic Wind Tunnel KAT

The tests were carried out in NLR's Small Anechoic Wind Tunnel KAT (Figure 1). The KAT is an open-circuit wind tunnel, with its test section surrounded by a 5 x 5 x 3-m room that is completely covered with 0.5-m foam wedges, yielding more than 99% absorption above 500 Hz. Two horizontal endplates (0.90 x 0.70-m) were mounted to the upper and lower sides of the rectangular 0.38 x 0.51-m nozzle, providing a semi-open test section for airfoil self-noise measurements (Figure 2 and Figure 3). To suppress reflections, the endplates were acoustically lined with a 5.5-cm layer of sound-absorbing foam covered by a 5% open-perforated plate. In case of inflow turbulence measurements, a turbulence grid was installed in the nozzle. The turbulence grid consisted of diagonally oriented, cylindrical, 12-mm bars with a mesh width of 60 mm.

### 2.2 Balance

The forces on the model were measured using a six-component balance placed below the lower side-plate on a turntable (Figure 4). The balance components were defined as follows:

- K1: gravity (max. 500 N, accuracy 0.25 N)
- K2: drag (max. 100 N, accuracy 0.3 N)
- K3: moment exerted by the drag (max. 50 Nm, accuracy 0.1 Nm)
- K4: lift (max. 500 N, accuracy 0.25 N)
- K5: torsion (max. 50 Nm, accuracy 0.1 Nm)
- K6: moment exerted by the lift (max. 500 Nm, accuracy 0.25 Nm)

### 2.3 Hot-wires

For the hot-wire measurements (in the empty test section) an automatic XYZ traverse system was used, to which a DANTEC cross-wire probe was attached (Figure 5). The cross wires were placed in the horizontal plane (at 45 degrees to the mean flow) to allow measurement of turbulent velocity fluctuations in the  $x$  and  $y$  direction. This enabled the determination of the angle between the vertical plane and the average flow direction. In this way, the turbulence components that determined the variation in angle of attack were measured. The cross-wire probes were connected to DANTEC hot-wire signal conditioning and data-acquisition equipment.

### 2.4 Microphone Array

The microphone array consisted of 48 0.5-in. microphones (type LinearX M51) mounted in an open grid and was designed for maximum side-lobe suppression at frequencies between 1 and 20 kHz. To obtain high resolution at low frequencies, the array dimensions needed to be rather large (0.8 x 0.6 m). The array was placed outside the tunnel flow at a distance of 0.6 m from the tunnel axis, on either the suction or the pressure side of the model (Figure 2). The relatively short distance between the array and the model was chosen to obtain maximum signal-to-noise ratio. The center of the array was placed at the same height as the tunnel axis.

### 2.5 Models

The airfoil shapes, accuracy, and a picture of the tested models are given in Figure 6 and Figure 7. In addition to the six candidate airfoils, a NACA 0012 airfoil was tested for later comparison to benchmark

data from NASA [2]. The models were provided by NREL (chord = 0.2286 m [9 in.], span = 0.509 m [20.039 in.], trailing-edge thickness less than 0.225 mm [0.009 in.]). Tripping of the models was done with zigzag tape over the complete span, at 2% chord on the suction sides of the airfoils and 5% chord on the pressure sides of the airfoils. The streamwise peak-to-peak length of the zigzag tape was 11 mm. The standard trip thickness was 0.25 mm, but for a number of conditions thicker trips were used (up to 0.5 mm). These cases will be indicated explicitly in the results.

In some cases, a stethoscope was used to verify whether the trip induced the desired boundary-layer transition. The stethoscope was attached to an L-shaped total-pressure tube (Figure 8), which was traversed manually over the surface of the model. By listening, the transition from a laminar to turbulent boundary layer could be discerned.

## 2.6 MEMS

The S822 model was also tested with Micro Electro Mechanical Systems (MEMS) simulators (Figure 9). These devices were mounted at 95% chord on the pressure side of the airfoil, using double-stick tape and Scotch<sup>®</sup> tape. Two sets of four MEMS were tested, A1-A4 and B1-B4. The tab height  $h$  was 3.18 mm for the A-MEMS and 4.76 mm for the B-MEMS. The gap size was 0 (solid tab),  $2h$ ,  $1h$ , and  $0.5h$  for MEMS #1 to #4, respectively.

## 3 Measurement and Processing Techniques

### 3.1 Wind-Tunnel Parameters and Balance

The wind-tunnel parameters (pressure, temperature) and balance signals were acquired and pre-processed by the tunnel data-acquisition system EGOIST [3]. For the calculation of the forces and moments, the tunnel data-processing software APROPOS [4] was used. Detailed backgrounds about balance measurements and their results are given in [5]. The performance of the balance was checked with weights before the test.

The model angle of attack was automatically measured and recorded. Because of the open-jet set-up, the *effective* angle of attack was smaller than the *geometrical* angle of attack. The magnitude of this “open-jet effect” depends upon the dimensions of the wind tunnel and the model chord. The effective angle of attack was calculated according to the method of Ref. 2, which for the present test implies that the geometrical angle of attack was divided by 2.26 to arrive at the effective angle of attack.

### 3.2 Hot-wires

Cross hot-wires were used to measure the turbulence intensity and flow angularity in the empty test section (i.e., no model), with and without turbulence grid. The DANTEC equipment was used for conditioning and filtering the hot-wire signals. The low-pass filter of the DANTEC equipment was set to 10 kHz. After this, the signals passed through an RMS (root-mean-square) converter. The further processing of the RMS signal was done using the SPTM module [6] of the NLR tunnel data-processing software APROPOS [4]. The cross-wire probe was calibrated before and after each run. These calibrations were performed in the center of the test section, for two wind speeds. The exact angle between the flow and the cross-wire probe (during calibration) was determined by rotating the probe over 180 degrees and carrying out a second measurement. The hot-wire processing included a correction for temperature drift during testing. The main results of the DANTEC hot-wire data processing were mean velocities, flow angles, and turbulence intensities in the  $x$  and  $y$  directions.

To determine turbulence *spectra* and identify spurious wire signals (e.g., probe holder vibrations), the unsteady wire signals were fed to the VIPER data-acquisition system [7]. On this system the unsteady signals were further processed to turbulence spectra. The acquisition and online processing parameters were as follows:

Sample frequency:	49.152 kHz
Measurement time:	20 s
High-pass filter:	none (DC mode)
Low-pass filter:	24 kHz
Block size:	32768
Window:	Hanning
Overlap:	50%
Number of averages:	60
Frequency resolution:	1.5 Hz

To reduce the scatter in the narrowband ( $\Delta f = 1.5$  Hz) spectral levels, the turbulence spectra shown in this report had a frequency resolution of 24 Hz, which was obtained by adding groups of 16 narrowband levels. The energy in each band was normalized by the nominal tunnel speed and divided by 24 so that the spectral levels represent the Power Spectral Density.

### 3.3 Microphone Array

#### 3.3.1 Data Acquisition

The acoustic data from the array microphones were synchronously measured using the VIPER data-acquisition system [7]. The acquisition and processing parameters were as follows:

Sample frequency:	51.200 kHz
Measurement time:	30 s
High-pass filter:	500 Hz
Low-pass filter:	25.600 kHz
Block size:	2048
Window:	Hanning
Overlap:	50%
Number of averages:	1500
Frequency resolution:	25 Hz

The raw time-data were stored on the SCSI disks of the VIPER system and on an IDE hard disk. Before the measurements, the sensitivity at 1 kHz was determined for all array microphones using a calibrated piston phone. Frequency-dependent sensitivities of individual microphones were taken from calibration sheets. No corrections were applied for microphone directivity, because this effect was the same for all airfoils and amounted to less than 2 dB for angles up to 45° and frequencies up to 15 kHz. Phase matching of the microphones was checked before the measurements were taken using a calibration source at a known position.

#### 3.3.2 Array Processing

The array data were processed using the computer program SOLACAN 4.5 [8], which produced acoustic “source plots” in 1/3-octave bands using conventional sum-and-delay beam forming. In this way, noise originating from the model was separated from background noise. To improve the resolution and further suppress background noise from the tunnel, the main diagonal in the cross-power matrix (auto powers) was discarded. The effect of sound refraction by the tunnel shear layer was corrected using the Amiet method [9], where the shear-layer center was assumed to be at the same  $y$  location as the edge of the tunnel nozzle. Furthermore, a spatial window was applied to the microphone signals, in order to correct for the variation in microphone density over the surface of the array. Finally, another spatial window was applied that reduced the effective array aperture with increasing frequency, in order to reduce coherence loss effects. The array scan plane was placed in the plane of the model and rotated in accordance with the angle of attack. The scan resolution was 0.5 cm in both directions, and the scan levels were normalized to a distance of 0.282 m  $[(4\pi)^{-1/2}]$ , so that for a monopole source the peak level in the source plot corresponded to the Sound Power Level.

#### 3.3.3 Airfoil Noise Spectra

For quantitative comparison of different airfoils and conditions, the array results were further processed using the computer program POWINT [10], which produced narrowband or 1/3-octave band spectra for specific source regions. Similar to the array processing described in the previous section, the main diagonal in the cross power matrix was discarded, and spatial windows were applied to the microphone signals to reduce coherence loss effects. Thus, the levels measured by the array represented noise levels radiated in the average direction of the array microphones, including the weighting as a result of the spatial win-

dows. Because the source directivity for trailing edge and inflow turbulence noise was expected to be the same for all airfoils, the comparison of noise from different airfoils was valid.

By defining an integration contour around the mid-span area of the model, extraneous noise sources at the model-endplate junctions were suppressed. As will be shown in the results, for the measurements without turbulence grid, the noise was radiated from the trailing edge of the model. Therefore, in these cases, the mid-span integration area was centered on the trailing edge. For the measurements *with* turbulence grid, the (dominant) noise source was found to be located at the leading edge of the model, so in these cases the integration contour was centered on the leading edge. This procedure is schematically shown in Figure 10. The size of the integration area was 0.2 m in the chordwise direction and 0.1 m in the spanwise direction, and the scan resolution was 1 cm in both directions.

Because the integration area “cuts” through the line source region at the leading or trailing edge, “leakage” from source regions outside the integration area into the integration contour, and vice versa, will occur. The magnitude of this effect depends on array resolution and, therefore, on frequency. To account for this effect, a “line source correction” was applied to the POWINT levels, which was determined from simulations of a 0.5-m span-line source in the present test set-up (similar to Ref. 11). The numerical values of this line correction are given in Table 1. The resulting spectral levels were Sound Power Levels produced by 10 cm of span.

**Table 1. Line Corrections Applied to POWINT Values**

Frequency band	Line correction (dB)
630	-6.1
800	-5.7
1000	-5.1
1250	-4.3
1600	-3.4
2000	-2.4
2500	-1.5
3150	-0.8
4000	-0.2
5000	0.3
6300	0.7
8000	0.7
10000	0.0
12500	0.3

### 3.3.4 Extraneous Sources

In a number of cases, the airfoil noise levels were so low that, despite the procedures described above, the airfoil noise spectra were dominated by extraneous tunnel noise sources. In order to facilitate rapid judgment of the validity of the measured levels, procedures were developed to indicate the importance of tunnel noise in the spectra.

For a significant number of conditions, the trailing-edge noise levels were influenced by extraneous sources at the model-endplate junctions (“corner sources,” e.g., Figure 10 or Figure 19). Therefore, a routine was developed that determined the importance of these corner sources and that, in case the influence of the corner sources on the trailing-edge noise level was more than 1 dB, calculated an *upper limit* for the 2D trailing-edge noise level. In the trailing-edge noise spectra, these upper limits would be indicated by the absence of a marker at that specific frequency (all spectral levels were connected by lines). If no (important) corner sources were found, this was indicated in the spectrum by a marker.

For the grid measurements, rather than corner sources, background noise from the turbulence grid itself dominated the leading-edge noise levels in a number of cases. Therefore, for these measurements the leading-edge noise levels from the measurement *with* model were compared to the levels obtained in the empty test section (with turbulence grid) for the same speed. In case the “leading-edge” noise level with model was more than 6 dB higher than the background noise level, this was indicated by a marker in the spectrum. Thus, the absence of a marker indicated that the spectral level could be influenced by grid noise.

## 3.4 Measurement Program

### 3.4.1 Hot-wires

Hot-wire traverses were made in  $y$  and  $z$  direction (see Figure 2 for orientation of axes) for two Mach numbers ( $M = 0.12$  and  $M = 0.18$ ) at two axial cross sections ( $x = 200$  mm and  $x = 430$  mm), with and without turbulence grid. The axial values corresponded roughly to the position of the leading- and trailing edge of the tested models ( $x = 218$  mm and  $x = 446$  mm, respectively, at zero angle of attack). The  $y$  and  $z$  traverses were made through the whole test section (i.e., from shear layer to shear layer and from plate to plate, respectively). The step size was 2 cm or smaller if required as a result of large gradients. Furthermore, a calibration was made of the flow velocity at the tunnel axis with the turbulence grid installed in the nozzle. This speed calibration was used to control the tunnel speed for the airfoil measurements with grid.

### 3.4.2 Balance

Balance measurements were done for all airfoils at a tunnel speed of 32 m/s, with and without trip and with and without turbulence grid. Lift and drag coefficients were determined as a function of the (geometrical) angle of attack, ranging from 6 to 20 degrees with an interval of 2 degrees. The resulting lift curves (obtained without turbulence grid in the nozzle) for the different airfoils and for the #1 and #4 MEMS are given in Figure 11 (the difference between geometrical angle-of-attack  $\alpha$  and effective angle-of-attack  $\alpha_{eff}$  is explained in Section 3.1). The lift curves *with* turbulence grid (not shown) were generally similar to the tripped results without turbulence grid. In the course of the test it was found that the measured *drag* coefficients were inaccurate, probably as a result of the gap of about 4 mm between the models and the upper endplate (e.g., [12]). Because the goal of this test was to determine the *acoustic* performance of the airfoils, the balance results will not be discussed further.

### 3.4.3 Microphone Array

Array measurements were done on the suction side of the six candidate airfoils, with and without tripping and with and without turbulence grid, for three angles of attack. The NACA 0012 airfoil was tested for

the same conditions as in [2] (i.e., with and without trip, without turbulence grid, for four Reynolds numbers [from 0.5 to 1.12 million] and five angles of attack). An overview of the measured Reynolds numbers is given in Table 2. For a number of conditions, *pressure-side* array measurements were done as well, to determine directivity effects. Some measurements were repeated with thicker boundary layer trips to assess their effectiveness.

The MEMS were tested on the tripped S822 airfoil. Pressure-side array measurements were done for all eight MEMS types, without turbulence grid, at a Reynolds number of 1 million and (geometrical) angles of attack of  $0^\circ$ ,  $10^\circ$ , and  $18^\circ$ . For MEMS A1, A4, B1, and B4 additional measurements were done at  $Re = 0.5$  and  $0.75$  million and with turbulence grid ( $Re = 1$  million). To assess directivity effects, MEMS A1, A4, B1, and B4 were also tested with the array on *the suction side* of the airfoil ( $Re = 0.5$ ,  $0.75$  and  $1.0$  million, without grid).

A complete overview of all acoustic measurements is given in Appendix 1.

## 4 Tunnel Calibration

The results of the calibration measurements of the empty test section are given in Figure 12 through Figure 15 for  $M = 0.12$  and  $M = 0.18$  and with and without turbulence grid. These figures show horizontal and vertical profiles of axial velocity, axial turbulence intensity, lateral turbulence intensity, and flow angularity, at two axial locations. These plots  $M$  and  $U$  represented the *nominal* tunnel Mach number and speed, using the settings for the empty tunnel without turbulence grid. *The turbulence intensities were also normalized using the nominal tunnel speed, so for the grid measurements the local turbulence intensity was about 20% higher than the values in the plots.* The flow angle  $\beta$  was the angle between the velocity in the  $x$ - $y$  plane and the  $x$ -axis.

The central part of the test section without turbulence grid showed turbulence levels of about 1% or less, whereas *with* turbulence grid the levels increased up to about 9% at  $x = 0.20$  m and 5% at  $x = 0.43$  m. The flow angle could be seen to increase with increasing speed and turbulence level, but remained within 1 degree in the central area for all cases. Typical spectra of the axial and lateral grid turbulence, on the tunnel axis at  $x = 0.2$  m for  $M = 0.12$ , are shown in Figure 16.

**Table 2. Overview of Measured Reynolds Numbers (in millions) with the Array on the Suction Side of the Model\***

	Turbulence grid off		Turbulence grid on	
Airfoil	Trip	No trip	Trip	No trip
S822	0.20/ 0.35/ 0.50/ 0.75/ 1.0	0.20/ 0.35/ 0.50/ 0.75/ 1.0	0.20/ 0.35/ 0.50/ 0.75/ 1.0	0.20/ 0.35/ 0.50/ 0.75/ 1.0
S834	0.20/ 0.35/ 0.50/ 0.75	0.20/ 0.35/ 0.50/ 0.75	0.20/ 0.35/ 0.50/ 0.75	0.20/ 0.35/ 0.50/ 0.75
FX 63-137	0.20/ 0.35/ 0.50/ 0.75	0.20/ 0.35/ 0.50/ 0.75	0.20/ 0.35/ 0.50/ 0.75	0.20/ 0.35/ 0.50/ 0.75
SG 6043	0.11/ 0.20/ 0.35/ 0.50	0.11/ 0.20/ 0.35/ 0.50	0.11/ 0.20/ 0.35/ 0.50	0.5
SH 3055	0.50/ 0.75/ 1.0	0.50/ 0.75/ 1.0	0.50/ 1.0	0.50/ 1.0
SD 2030	0.20/ 0.35/ 0.50	0.20/ 0.35/ 0.50	0.20/ 0.50	0.20/ 0.50
NACA 0012	0.50/ 0.62/ 0.87/ 1.12	0.50/ 0.62/ 0.87/ 1.12	0.50/ 0.62/ 0.87/ 1.12	0.50/ 0.62/ 0.87/ 1.12

*\*For the six candidate airfoils, all Reynolds numbers were measured for geometrical angles of attack of 0°, 10°, and 18°, except the shaded boxes (0°, 5°, and 10°). The NACA 0012 airfoil was measured for geometrical angles of attack of 0°, 4.5°, 9.0°, 12.0° and 16.5°, in order to obtain the same effective angles of attack as in Ref. 2.*

## 5 Airfoil Noise Results

A general introduction to the presentation of the airfoil noise spectra and the way they were obtained is presented in Section 5.1. Section 5.2 then gives an overview of the acoustic results for all models (excluding the MEMS), with and without turbulence grid and with and without trip. In subsequent sections, these results will be further analyzed in terms of speed dependence, tones, and directivity and compared to benchmark data. Section 5.7 presents a comparison between the noises from different airfoils for identical conditions. In Section 5.8, the acoustic results of the MEMS are described, compared to baseline data (S822 airfoil *without* MEMS), and analyzed in terms of directivity. Section 5.9 finally presents a method for physically reducing extraneous noise sources at model-endplate junctions, thus improving the quality of the acoustic airfoil measurements.

### 5.1 Introduction

Typical examples of acoustic source plots for airfoil measurements without and with turbulence grid are shown in Figure 17 and Figure 18, respectively. These acoustic source plots provide the distribution of the noise sources in the plane of the model as a function of frequency (note that the  $y$ -axis in these source plots corresponds to the  $z$ -axis in the tunnel coordinate system, Figure 2). The tunnel flow goes from left to right, and the gray line indicates the airfoil contour. The levels in these plots are Sound Power Levels (see also Section 3.3.2) in dBs (1/3-octave band levels), and the dynamic range of the color scale is always 12 dB. Note that the level of the color scale is adjusted to the maximum level in the plot, so that the same colors do not necessarily correspond to the same levels for different plots.

Figure 17 and Figure 18 illustrate that *without* inflow turbulence the noise was radiated from the trailing edge, while *with* turbulence the (dominant) noise source was located at the model leading edge. This shift of the dominant noise source region from trailing to leading edge after introducing inflow turbulence was observed for practically all measurements and can be explained by the different mechanisms responsible for inflow turbulence and trailing-edge noise [13]. The only cases for which trailing-edge noise was observed in combination with inflow turbulence will be discussed in Section 5.8 (MEMS results).

The array plots also show that the array resolution increased with increasing frequency because the acoustic wavelength became smaller. For some conditions, extraneous noise sources could be observed as well (e.g., the high levels at  $x = 0$  for 2.5 and 3.15 kHz in Figure 18 originated from the turbulence grid in the nozzle).

As explained in Section 3.3.3, these source plots were further processed to airfoil noise levels by integrating the mid-span part of the leading edge (grid measurements) or trailing edge (no-grid measurements). The resulting acoustic spectra gave the Sound Power Level of the airfoil noise produced by 10 cm of span in 1/3-octave bands. For a number of conditions, however, the airfoil was so quiet that extraneous tunnel noise sources, such as the model-endplate junctions (Figure 19) or the turbulence grid (Figure 20 and Figure 45b), became dominant and disturbed the spectral levels. The importance of such extraneous sources for a specific spectral level will be indicated by the presence or absence of a marker (see also Section 3.3.4). For measurements without turbulence grid, the absence of a marker indicated that important corner sources were present and that the level shown was an upper limit for the 2D trailing-edge noise level. For measurements *with* turbulence grid, the absence of a marker indicated that the spectral level was probably influenced by grid noise.

As an example of trailing-edge noise spectra, we can have a look at the data for the NACA 0012 airfoil (Figure 21). The spectra are arranged in two columns (trip and no trip), and each plot gives the data for one angle of attack. Both the geometrical and the effective angle of attack are given above the plot. The effective angle of attack was calculated according to Ref. 2 (Section 3.1). The different lines corresponded to different tunnel speeds. Looking at the tripped data, we see that at intermediate frequencies most data had a marker, indicating that no dominant corner sources were present. At many lower and

higher frequencies, however, often no markers were shown, indicating that dominant corner sources were present and that these values were upper limits for the actual trailing-edge noise (Figure 19). Typically, this effect became more important at higher angles of attack. Note that the presence of a marker did not necessarily mean that the spectral level was a result of trailing-edge noise! To illustrate this, consider the plot for the tripped NACA 0012 airfoil at  $\alpha = 9.1^\circ$  (Figure 21). For the two lowest speeds, a marker was observed at the highest frequency, indicating that no important corner sources were present. However, the acoustic source plots for these frequencies showed that these levels were not caused by trailing-edge noise, but were a result of other background noise (Figure 20).

In principle, all tripped results were measured with a trip thickness of 0.25 mm on both sides of the model (Section 2.5). However, for a number of airfoils, the low-speed measurements were repeated with an increased trip thickness (on both sides) because there were doubts about the effectiveness of the trip. These spectra are indicated by an \*, and the appropriate trip thickness is given in the figure caption (e.g., Figure 22).

As an example of inflow turbulence (or leading-edge) spectra, we can have a look at the data for the S822 airfoil (Figure 31). The arrangement of the plots is similar to the trailing-edge results. Again, the different lines correspond to the (average) tunnel speeds (as obtained from the hot-wire speed calibration at the empty tunnel centerline behind the turbulence grid). For these spectra, the absence of a marker indicated that the spectral levels were probably influenced by grid noise. Here, typically the best data (i.e., highest leading-edge noise levels) were obtained at high speeds and large angles of attack. For low speeds and small angles of attack the inflow turbulence noise level were too low (with respect to grid noise) to be detected.

In general, the measured inflow turbulence noise levels were much higher than the trailing-edge noise levels (for example, compare Figure 22 to Figure 31). It should be realized that this does not imply that in practice inflow turbulence noise would be dominant for these airfoils. On a real wind turbine, the inflow turbulence levels depend on the (atmospheric) turbulence levels in the incoming flow, which might be much lower than the turbulence intensities produced by the grid in the wind tunnel. As a result, trailing-edge noise will be dominant for many wind turbines. Therefore, the grid measurements in the present test should be regarded as a study into the *susceptibility* of the different airfoils to inflow turbulence noise, for a particular level of turbulence in the incoming flow.

## 5.2 Overview of Acoustic Results for Different Airfoils

### 5.2.1 Trailing-Edge Noise

Overview plots of the trailing-edge noise spectra of all airfoils are given in Figure 21 through Figure 27. For most airfoils, the results for the lowest speeds are not shown because no trailing-edge noise was visible in these source plots. The NACA 0012 (Figure 21) results showed a clear difference between tripped and untripped data. Whereas the tripped results exhibited smooth, broadband spectra, which could be associated with turbulent boundary-layer trailing-edge noise, the untripped results showed significant peaks for many speeds and angles of attack. As a result of the thin trailing edge of the models (see Section 2.5), these tones could not be explained by trailing-edge bluntness vortex shedding noise. They *could* be associated, however, with laminar boundary layer vortex shedding [2]. This mechanism involves a feedback loop between noise from the trailing edge and Tollmien-Schlichting instability waves originating at an upstream location in the laminar boundary layer. The frequency of these peaks could be seen to increase with speed and seemed to decrease with angle of incidence. Figure 28 shows the acoustic source plot corresponding to the spectral peak at 1.6 kHz for the untripped NACA 0012 airfoil at 39.6 m/s and  $\alpha = 9.1^\circ$ . This plot confirms that the noise originated from the trailing edge. It can also be seen that, in contrast to the *broadband* trailing-edge noise shown in Figure 17, the source region for the tonal source did not fully extend up to the endplates. This suggests that the feedback loop, which was believed to be responsible for the spectral peaks, was interrupted close to the endplates.

For the S822 airfoil (Figure 22), similar trends were observed (i.e., broadband spectra for the tripped cases and spectral peaks for the untripped cases). Again, the peak frequency for the untripped cases increased with speed, while the peaks were somewhat broader than for the NACA 0012 airfoil. The similarity in results suggests that the mechanisms were the same as for the NACA 0012 airfoil. Indeed, the acoustic source plots for the spectral peaks looked similar to the source plots for the NACA 0012 peak shown in Figure 28. For one condition, an atypical result was found: in contrast to all other tripped S822 (and NACA 0012) results, the spectrum for 32 m/s and  $\alpha = 18^\circ$  showed a “hump” around a frequency of 1.6 kHz. Inspection of the corresponding source plot revealed that this peak was caused by a noise source at the trailing edge, centered slightly above the tunnel axis (Figure 29a). This asymmetric source distribution was different from the generally observed symmetric source regions (e.g., Figure 17 or Figure 28). A possible explanation is that the feedback loop, which was believed to be responsible for the spectral peak in the *untripped* case (Figure 29b, note that the color scale is different from Figure 29a), was partly interrupted by tripping, but not completely. In such an unstable condition, small geometric details of the model or trip might have resulted in different behavior at different spanwise locations. In section 5.5, it was shown that the spectral hump was also measured with the array on the pressure side, illustrating that the mechanism is reproducible.

The results for the S834 airfoil (Figure 23) were similar to the S822 results, although the peaks in the untripped cases seemed to be sharper. The similarity in results suggested that the mechanisms were the same as for the NACA 0012 and the S822 airfoil (i.e., turbulent boundary-layer trailing-edge noise in the tripped cases and laminar boundary-layer vortex-shedding noise for the untripped cases). Again, the acoustic source plots for the spectral peaks looked similar to the source plots for the NACA 0012 peak shown in Figure 28. Similar to the S822 airfoil, atypical spectral peaks were also found for the tripped case at  $\alpha = 18^\circ$ , which were again a result of an asymmetrical source distribution at the trailing edge (Figure 30). A possible explanation might be that the flow was unstable for this condition.

The four remaining airfoils, FX 63-137, SG 6043, SH 3055 and SD 2030 (Figure 24 through Figure 27), all showed broadband spectra without peaks for the tripped condition, although for many cases only an upper limit could be given because of low trailing-edge noise levels with respect to the corner sources. For a number of untripped cases again peaks were found, mainly at the low angles of attack.

The speed and  $\alpha$ -dependence of peak frequencies and spectral levels, as well as the nature of the tones, will be further discussed in Sections 5.3 and 5.4.

### 5.2.2 Inflow Turbulence Noise

Overview plots of the inflow turbulence or leading-edge (Section 5.1) noise spectra of all airfoils are given in Figure 31 through Figure 36. As was the case for the trailing-edge noise spectra, the results for the lowest speeds are not shown because no leading-edge noise was visible in these source plots. For the same reason, only the data up to some maximum frequency are shown. As explained in Section 5.1, the fact that the inflow turbulence noise levels were generally much higher than the trailing-edge noise levels does not imply that in practice inflow turbulence noise will be dominant for these airfoils.

The S822 results (Figure 31) showed broadband inflow turbulence spectra without peaks. Practically no difference was observed between tripped and untripped conditions, and an increase in angle of attack seemed to give higher levels at the higher frequencies. The other airfoils exhibited similar behavior. A further analysis of the speed dependence of the levels, and a comparison of the levels for different airfoils will be given in subsequent sections.

## 5.3 Dependence of Airfoil Noise Levels on Speed and Angle of Attack

In order to analyze the speed dependence of the measured airfoil noise spectra, these were plotted in a normalized way (i.e., normalized levels as a function of Strouhal number  $St = fC/U$ , where  $f$  was frequency,  $C$  was model chord, and  $U$  was tunnel speed). It should be noted that in some studies a Strouhal

scaling based on, for example, boundary-layer thickness was applied. However, because this information was not available, here the model chord was used. The normalized levels were calculated according to  $PWL_{norm} = PWL - 10 \cdot \log_{10}(U^m)$ , where  $PWL$  is the airfoil Sound Power Level determined from the array measurements (Section 3.3.3) and  $m$  denoted the speed dependence of the airfoil noise levels ( $p^2$  proportional to  $U^m$ , with  $p$  the acoustic pressure). Note that in the figures presented below,  $\log_{10}$  was indicated as  $^{10}\log$ .

### 5.3.1 Trailing-Edge Noise

Normalized trailing-edge noise spectra for the NACA 0012 airfoil were produced for values of  $m$  between 4 and 6.5 (with a step size of 0.5), which gave the best results for  $m = 4.5$  (Figure 37). Note that because of the normalization the levels could become negative. A very good data collapse was obtained for the tripped conditions: for a given angle of attack, the trailing-edge noise levels at different speeds coincided within 1 to 2 dB. This showed that the normalization in terms of  $St$  and  $PWL_{norm}$  worked very well for the turbulent boundary layer trailing-edge noise, so that experimental results for a given speed could be easily extrapolated to any other speed. The  $\alpha$ -dependence of the tripped trailing-edge noise spectra is explicitly shown in Figure 38 (left plot). Here it can be clearly seen that the levels at low frequencies increase with increasing  $\alpha$ .

The optimum value of  $m = 4.5$  found here was slightly lower than the value of 5 found in Ref. 2 and Ref. 14. A reason for this discrepancy might be that, despite the use of a spatial window (Section 3.3.2) and the use of an integration contour rather than peak levels (Section 3.3.3), the array levels were still susceptible to coherence loss to some degree. This effect was a result of the propagation of the sound through the wind-tunnel shear layer and resulted in reduced array levels for high speeds and high frequencies [15].

For *untripped* conditions, the peak Strouhal numbers for different speeds coincided within about 30% for each angle of incidence, although they seemed to increase slightly with increasing speed (Figure 37). This suggested that a better collapse of peak frequencies could be obtained by using the boundary-layer thickness as the length scale in  $St$  (rather than chord) because the boundary-layer thickness at the trailing edge would decrease with increasing Reynolds number [2]. The  $\alpha$ -dependence of the untripped trailing-edge noise spectra is explicitly shown in Figure 38 (right plot).

The spectral *levels* for the untripped results in Figure 37 did not collapse as well as for the tripped data. Other values of  $m$  did not significantly improve the collapse. This illustrates that the normalization in terms of  $St$  and  $PWL_{norm}$ , as described above, did not work very well for the complex feedback mechanism associated with laminar boundary-layer vortex-shedding noise. In Section 5.6, these NACA 0012 spectra will be compared to benchmark data [2].

For the other airfoils, similar results were found: again the best collapse for the tripped data was obtained for  $m = 4.5$ . This was illustrated in the normalized trailing-edge noise spectra for the S822 and S834 airfoils (Figure 39 and Figure 40, respectively). As expected, an obvious collapse was not observed for the atypical peaks in the tripped data at  $\alpha = 18^\circ$  (see also Section 5.2.1). The untripped data again showed no good collapse, and the  $\alpha$ -dependence was similar to the NACA 0012 data as well.

### 5.3.2 Inflow Turbulence Noise

Similar to the trailing-edge noise normalization, normalized inflow turbulence noise spectra for the S822 and S834 airfoils were produced for values of  $m$  between 4 and 6.5 (with a step size of 0.5). In this case best, results were obtained for  $m = 6$  (Figure 41). For these measurements, the tripped results were practically the same as untripped; therefore, only the tripped cases are shown. It can be seen that a good data collapse was obtained, indicating that the normalization in terms of  $St$  and  $PWL_{norm}$  also worked well for inflow turbulence noise. The optimum value of  $m = 6$  found here was in good agreement with theoretical predictions for low-frequency inflow turbulence noise [14]. The  $\alpha$ -dependence of the inflow turbulence

noise spectra is shown in Figure 42 for three airfoils. These plots show a high-frequency increase in noise for high angles of attack.

#### 5.4 Pure Tones and Effect of Boundary-Layer Trips

Three of the six candidate airfoils showed intense, narrowband tones in the trailing-edge noise spectra for the untripped condition: S834 ( $\alpha = 10^\circ$ ), SG 6043 ( $\alpha = 0^\circ$ ), and SD 2030 ( $\alpha = 0^\circ$ ). As can be seen in the trailing-edge noise overview plots for these airfoils (Figure 23, Figure 25, and Figure 27, respectively), the tones disappeared after proper tripping. The frequency of the tones appeared to increase with increasing tunnel speed, which is most clearly illustrated in Figure 23. As mentioned before, the thin trailing edge of the models excluded trailing-edge bluntness vortex shedding noise as a possible cause for these tones. As mentioned before, the tones were located at the mid-span part of the trailing edge, similar to the NACA 0012 tone shown in Figure 28. This suggested that the feedback loop, which was believed to be responsible for the spectral peaks, was interrupted close to the endplates.

The nature of these tones was investigated in more detail, and because the tones were most pronounced for the lowest speed, the investigation focused on a tunnel speed of 22.4 m/s. The narrowband spectra for these cases (Figure 43) showed peaks at about 1 and 2 kHz for all three airfoils. The similarity in peak frequencies suggests that the frequencies are related to the model scale. On the other hand, in Ref. 2 the best data collapse was obtained using a Strouhal number based on boundary-layer thickness rather than model chord (for laminar boundary-layer vortex-shedding tones from the NACA 0012 airfoil). The angle-of-attack range for which the tones occurred was estimated by listening in the test section during an  $\alpha$ -sweep. This gave the following ranges:  $7.5^\circ < \alpha < 13^\circ$  for S834,  $-8^\circ < \alpha < 2^\circ$  for SG 6043, and  $-10^\circ < \alpha < 4^\circ$  for SD 2030. By tripping one side of the airfoil at a time, it was determined from which side of the airfoil the tones originated. For the S834 and the SD 2030 airfoils, this turned out to be the pressure side, whereas for the SG 6043 airfoil, the tones originated from the suction side of the airfoil. Stethoscope measurements (Section 2.5) on the pressure side of the S834 model indicated a laminar boundary layer up to about 80% chord without tripping, while after tripping the transition to a turbulent boundary layer occurred directly behind the trip at 5% chord. This observation supports the hypothesis that the tones are caused by laminar boundary-layer vortex-shedding noise.

The sensitivity of the tones to trip thickness was investigated in more detail for the S834 airfoil (Figure 44). The untripped case was the same as in Figure 43 and showed the narrowband peak at 925 Hz and the harmonic at 1850 Hz. It could be seen that the standard trip thickness of 0.25 mm on both sides was not effective: the level of the tones even increased slightly with respect to the untripped case, and an extra harmonic appeared at 2775 Hz. After application of a slightly thicker trip (0.30 mm) on the pressure side only, the spectral levels decreased dramatically, and the 925- and 1850-Hz tones vanished completely (although a less intense peak remained at 2775 Hz). Interestingly, the broadband level decreased even further after the addition of a 0.3-mm trip on the suction side. This suggested that the suction-side boundary layer dominated the broadband noise production, whereas the pressure side might generate tones if it is not properly tripped.

A final interesting observation with regard to the tones is that they disappeared in case of upstream turbulence. This is illustrated in Figure 45, which shows the 1- and 2-kHz source plots for the untripped S834 model at 22.4 m/s and  $\alpha = 10^\circ$ , with and without turbulence grid. It can be seen that the inflow turbulence removed the trailing-edge tones so that grid noise became dominant. Apparently, the inflow turbulence interrupted the feedback mechanism considered to be responsible for the tones.

#### 5.5 Directivity

To assess possible differences in the noise radiated in different directions, certain conditions were measured with the array positioned on the *pressure* side of the model. On the basis of literature [2,13,14] a trailing-edge noise directivity according to  $p^2 \sim \sin^2(\theta)$  was expected for the low frequencies and

$p^2 \sim \sin^2(\theta/2)$  for the higher frequencies (flat-plate approximation, see Figure 46a for definition of  $\theta$ ). Thus, although the contribution of the suction- and pressure-side boundary layers might be different, the total trailing-edge noise radiation was expected to be symmetrical around the chord as a result of scattering at the trailing edge. For lower frequencies, the maximum noise emission was expected in the direction perpendicular to the chord ( $\theta = 90^\circ$ ), whereas for higher frequencies the maximum shifted toward the nose of the airfoil.

The trailing-edge noise radiation in the suction- and pressure-side directions was compared for the NACA 0012 airfoil in Figure 47. This figure shows that the trends for suction- and pressure-side noise radiation were the same for all angles of attack and with and without trip. For zero angle-of-attack, the agreement between both directions was excellent. In addition, the suction-side levels became slightly higher than the pressure-side levels with increasing angle of attack. This might be explained by the difference in measured direction for the suction- and pressure-side arrays for  $\alpha \neq 0$  (Figure 46b). The suction-side array measured in a direction more toward the nose of the airfoil, which results in higher levels according to the  $\sin^2(\theta/2)$  directivity.

The directivity results for the S822 (Figure 48) and S834 (Figure 49) airfoils were similar to those of the NACA 0012 airfoil; the trends for suction and pressure side were the same for all angles of attack, and the suction-side levels became higher than the pressure-side levels with increasing angle of attack. Note in Figure 48 that the atypical hump in the tripped S822 spectrum at  $\alpha = 18^\circ$  (Section 5.2.1) was reproduced on the pressure side.

An example of the directivity of *inflow turbulence* noise is shown in Figure 50. Again, the observed trends were the same for the noise radiated in the suction and pressure-side direction. However, in contrast to the trailing-edge noise directivity plots, here the *pressure-side* levels seemed to become higher with increasing angle of attack. This is consistent with the expected high-frequency directivity for inflow turbulence noise, which had the same  $\sin^2(\theta/2)$  dependency as trailing-edge noise, except that here  $\theta$  was defined with respect to the *leading edge*. This means that highest leading-edge noise levels were expected in the direction of the trailing edge.

## 5.6 Comparison with Benchmark Data

Acoustic measurements were done on the NACA 0012 airfoil, in order to enable direct comparison to existing benchmark data from NASA [2]. The airfoil shape and chord (0.2286 m [9 in.]) were identical, and in both studies the 2D model was mounted between two endplates attached to opposite sides of the rectangular tunnel nozzle. The NLR nozzle (0.38 x 0.51 m<sup>2</sup>) was somewhat larger than NASA's (0.31 x 0.46 m<sup>2</sup>), resulting in a larger model span for the NLR tests (0.51 m versus 0.46 m). Whereas in the present tests tripping was done using 0.25-mm zigzag tape at 2% (suction-side) and 5% (pressure-side) chord, NASA employed a random distribution of grit in strips from the leading edge to 20% chord. The NLR measurements were done at the same tunnel speeds and effective angles of attack (Section 3.1) as in the NASA study.

In the present tests, acoustic data were acquired with a 48-microphone phased array, and trailing-edge noise spectra were determined by integrating the mid-span trailing-edge area in the acoustic source plots (Sections 2.4 and 3.3). The 1/3-octave band levels represented the Sound Power Level produced by 10 cm of span, in the direction of the array. In the NASA tests, cross-correlations between pairs of microphones were used to separate trailing-edge noise from other sources. The data were presented in 1/3-octave band Sound Pressure Levels, as perceived at a distance of 1.22 m from the trailing edge at  $\theta = 90^\circ$  (see Figure 46a for definition of  $\theta$ ). To account for the differences in level definition (PWL produced by 10 cm of span versus SPL at 1.22 m), in the present report 6.14 dB was added to the NASA levels. No correction was made for differences in directivity because the directivity was not exactly known and might have depended on frequency. However, for zero angle of attack the difference in directivity between the NASA

and NLR data was expected to be small (less than 1 dB). For  $\alpha \neq 0$ , directivity effects might have increased (Section 5.5).

A detailed analysis of the NASA data, including comparison with predictions, is given in [2]. The characteristics of the NLR NACA 0012 data were discussed in previous sections: a general introduction to the presentation of the NLR spectra was given in Section 5.1, while Section 5.2.1 presented an overview of the measured NACA 0012 data at different speeds and angles of attack. Section 5.3.1 dealt with the dependence of trailing-edge noise levels on speed and angle of attack, and directivity effects were discussed in Section 5.5.

The comparison between the NASA and NLR data is presented in Figure 51 through Figure 54 for four tunnel speeds. As explained in Sections 3.3.4 and 5.1, the absence of a marker in the NLR data indicated that “corner sources” had a significant (i.e., more than 1 dB) influence on the spectral level, so that this level was an upper limit for the actual 2D trailing-edge noise. The comparison figures showed a consistent picture for the different speeds: the general character of the spectra was well reproduced (i.e., broadband spectra for the tripped cases and spectral humps or tones for a number of untripped cases, depending on angle of attack). The frequencies of these humps corresponded quite well, although differences in level occurred, probably as a result of the sensitivity of the source mechanism to small geometric details. The *tripped* results revealed an interesting difference between the NASA and NLR data: although the spectral levels corresponded quite well for intermediate frequencies (e.g., 2-4 kHz at 31.7 m/s and  $\alpha_{eff} \leq 4^\circ$ , Figure 51), the NASA data showed a dominant hump around 1 kHz with a “shoulder” around 3 kHz. The 1-kHz hump did not appear in the NLR data. Similar differences can be observed in the tripped data for the other speeds.

To understand this discrepancy, we can have a closer look at both data sets. Concerning the NLR data, the acoustic source plots for the 31.7 m/s case at 1 kHz (Figure 55) confirmed that the low-frequency spectral levels in the NLR data were caused by noise from the trailing edge. Furthermore, the normalized trailing-edge noise spectra in Figure 37 showed a good data collapse (for the levels *with* marker), also at the low frequencies. This suggests that the source mechanism was the same for all speeds and could be described by the given normalization. The  $\alpha$ -dependence of the tripped NACA 0012 spectra also showed consistent behavior (Figure 38). With regard to directivity, Figure 47 showed that the spectral shape was the same for both directions. Moreover, comparison of the array-determined airfoil noise spectrum with the absolute sound level on a single-array microphone (for a “noisy” condition, where the airfoil noise dominates tunnel noise) showed a good agreement (within about 1 dB), also for low frequencies.

The NASA data showed the low-frequency hump for most speeds and angles of attack and also for models with a different chord [2]. The peak frequency of the hump seemed to increase with decreasing chord, increasing speed and decreasing angle of attack. However, the speed dependence of the peak frequency did not seem to be linear. In the NASA study, the measured spectra were compared to predictions that included several airfoil self-noise mechanisms. For higher angles of attack, a double hump in the spectrum was explained by (1) a different contribution from the suction- versus pressure-side boundary layer, each with its own peak frequency, and (2) separation of the suction-side boundary layer. However, this did not explain the double hump (i.e., the 1-kHz hump and the “shoulder” around 3 kHz) in the spectrum at  $\alpha = 0^\circ$ ; at zero angle of attack the pressure- and suction-side boundary layers should be identical for the symmetrical NACA 0012 airfoil, so that the noise spectrum should only have a single hump. A possible cause for the 1-kHz hump in the NASA data could be the presence of extraneous noise sources at the junctions between the endplates and the model trailing edge in the NASA tests (their two-microphone source-location method did not allow distinction between corner sources and sources along the span). However, from experience in other tests and with different methods, corner sources were not considered to be present in the NASA results [15]. An alternative explanation for the double humps could be reflections or multi-path-type effects from the endplate corner region [16].

In conclusion, no clear explanation was found for the discrepancy between the NASA and NLR results. A remaining possibility is the difference in trip method; the NASA trips, consisting of a random distribution of grit in strips from the leading edge to 20% chord, were probably more severe than the 0.25-mm zigzag tapes employed by NLR. This might have caused a difference in boundary-layer development and, consequently, in the radiated noise. Another possibility is that, despite numerous calibrations in both tests, the differences in measurement and processing techniques (two-microphone method versus acoustic array) still resulted in different absolute noise levels for some conditions.

## 5.7 Comparison of Different Airfoils

Although the different models were tested for different speed and angle-of-attack ranges, all airfoils were tested at a speed of 32 m/s and  $\alpha = 0^\circ$  and  $10^\circ$ . This enabled a direct comparison of the airfoil noise for identical conditions (the NACA 0012 data were taken at a slightly different speed of 31.7 m/s and angles of attack of  $0^\circ$  and  $9.5^\circ$ ). It should be noted that comparison on the basis of same angle of attack implies that the aerodynamic performance will be different (see lift curves in Figure 11).

The trailing-edge noise spectra of the different airfoils are compared in Figure 56. For the untripped condition, the noisiest airfoils are SD 2030 and SG 6043 at  $0^\circ$  and NACA 0012 and S834 at  $10^\circ$ . After tripping, for most airfoils the noise levels were reduced as a result of elimination of tones. Although the comparison for this condition was hampered because for many frequencies only upper limits were available, it seemed that the FX 63-137 airfoil was relatively noisy, whereas the S834, S822, and SD 2030 levels were rather low. These observations are reflected in Figure 57, which shows A-weighted overall noise levels of the different airfoils for the four different conditions. These levels were obtained by taking the sum of the plotted 1/3-octave band levels between 0.8 and 12.5 kHz. As a result, these overall levels represented an *upper limit* for the actual 2D trailing-edge noise.

Inflow turbulence noise spectra are compared in Figure 58. Because the leading edge noise spectra were identical for tripped and untripped conditions (Section 5.2.2), only tripped results are shown here, and the  $18^\circ$  angle of attack is also included. Clear differences between noise levels, up to more than 5 dB, were observed. By comparing these results with the airfoil shapes in Figure 6, a general trend can be identified: the sharper the airfoil leading edge, the higher the inflow turbulence noise levels. These observations are confirmed in Figure 59, which shows A-weighted overall noise levels of the different airfoils for the three angles of attack. These levels were obtained by taking the sum of the plotted 1/3-octave band levels between 1 and 2.5 kHz.

## 5.8 MEMS

Besides the tests on the six candidate airfoils and the NACA 0012 reference airfoil, acoustic measurements were also performed using MEMS (Micro Electro Mechanical Systems) simulators. These micro-tab devices have been the subject of research [17, 18] on active load control and lift enhancement for airfoils and wind turbine blades. The MEMS simulators were mounted on the S822 model, and a total of eight different types of MEMS were tested (Section 2.6). All MEMS tests were done with standard leading edge tripping, and because the MEMS simulators were mounted on the pressure side of the model, most measurements were done with the array on the pressure side. All MEMS were tested at the most relevant speed of 64 m/s (corresponding to a Reynolds number of 1 million). For the MEMS types A1, A4, B1, and B4, additional measurements were done at lower speeds, with turbulence grid, and with the array on the suction side (to assess the directivity of the MEMS noise).

### 5.8.1 Introduction

Typical acoustic source plots for a MEMS measurement are shown in Figure 60. These plots illustrate that, as expected, the dominant noise source was located in the trailing-edge region for all frequencies. More specifically, the noise seemed to be radiated from the MEMS simulator itself, rather than the model trailing edge. For a number of cases, both the MEMS and the trailing edge could be identified in the

source plots (Figure 61). The acoustic source plots were processed to trailing-edge noise spectra using the same method as for the other airfoils. This method is described in Section 3.3.3 and further explained in Section 5.1. As a result of the axial extent of the integration contour (Figure 10), noise from both the trailing edge and the MEMS itself is included in the trailing-edge noise spectra.

Overview plots of the trailing-edge noise spectra for the baseline (i.e., tripped S822 without MEMS) and #1 and #4 MEMS at three different tunnel speeds are given in Figure 62 through Figure 64. These plots show a general increase in MEMS noise levels with increasing speed and the occurrence of tones and “humps” in the spectra at some conditions. To more clearly bring out the increase in noise with respect to the baseline, Figure 65 shows the trailing-edge noise spectra for all MEMS together with the baseline. The MEMS gave a broadband noise increase of about 5 dB and that for specific conditions very intense tones occurred. The noisiest MEMS configuration was B1, which was the solid tab with the largest height. This configuration produced a tone of almost 95 dB at 1250 Hz for  $\alpha = 0^\circ$ . Figure 66 shows that this tone radiated from the mid-span part of the trailing edge, similar to the tones observed for the NACA 0012, S834, SG 6043, and SD 2030 airfoils (e.g., Figure 28). This suggests that the mechanism responsible for the MEMS tones was interrupted close to the endplates.

### 5.8.2 Tones

Given the relatively high Reynolds number and the fact that the model was tripped, it is not expected that the MEMS tones were a result of laminar boundary-layer vortex shedding, as was the case for the other airfoil tones (Sections 5.2.1 and 5.4). Furthermore, the thin trailing edge of the models excluded trailing-edge bluntness vortex-shedding noise as a possible cause for these tones. The narrowband spectra for the most prominent MEMS tones (B1 and A1 at  $\alpha = 0^\circ$ ) are shown in Figure 67. For both MEMS, the peak frequencies were proportional to the tunnel speeds, which indicated a Strouhal-like dependency of peak frequency on tunnel speed. This suggested that vortex shedding from the MEMS, possibly in combination with an interaction with the trailing edge, was responsible for the tones. At both speeds, the ratio between the peak frequencies of the A- and B-MEMS was about 1.15, which differed from the ratio between tab heights ( $4.76/3.18 = 1.5$ ). So, although the ratio was the same at both speeds, the peak frequency did not simply scale with tab height.

### 5.8.3 Directivity

Because the MEMS were mounted only on the pressure side of the model, an asymmetric radiation pattern might have occurred. Therefore, besides the pressure-side tests, measurements were also done with the array on the suction side of the model. The noise radiation in both directions is compared for the A- and B MEMS in Figure 68 and Figure 69, respectively. These directivity figures show that the trends for the suction- and pressure-side radiation were the same in all cases. Also, the suction-side levels increased with respect to the pressure side levels for increasing angle of attack. This trend was the same as observed for the other airfoils and was probably a result of the change in  $\theta$  for increasing angle of attack (Section 5.5). This would mean that the MEMS noise sources, as such, had a symmetric directivity, despite the fact that they were located on one side only.

### 5.8.4 Inflow Turbulence

To assess possible effects of the MEMS on inflow turbulence noise, measurements with turbulence grid were also conducted. Leading-edge noise spectra were obtained using the same method as for the other airfoils, which was described in Section 3.3.3 and further explained in Section 5.1. The leading-edge noise spectra obtained with and without MEMS are compared in Figure 70. Here it can be seen that the effect of the MEMS on inflow turbulence noise was negligible.

An interesting observation regarding the MEMS measurements with grid is that, because of the inflow turbulence, the *trailing-edge* tone observed for the B1 MEMS shifted to a higher frequency (Figure 71). The 1250-Hz tone was dramatically reduced after mounting the turbulence grid, while at 1600 Hz a new

trailing-edge peak appeared. A similar effect was observed for the A1-MEMS trailing-edge tones. Apparently the inflow turbulence influenced the mechanism responsible for the trailing-edge tones.

## 5.9 Corner Noise Reduction

At the end of the test program, it was attempted to physically suppress the extraneous noise sources at the model-endplate junctions (“corner sources”, Sections 3.3.4 and 5.1). In the standard set-up, small gaps were present between the model and the endplates (about 4 mm on the upper side and about 1 mm on the lower side) in order to enable balance measurements (Figure 4). With the FX 63-137 model installed, several corner noise-reduction techniques were tested, including closing the gap with tape, applying a single serration at the trailing-edge corners, and smoothing the corners with plasticine. Some of these devices were successful at some frequencies, but gave an increase of the extraneous noise sources at other frequencies.

However, a treatment consisting of filling the upper gap with foam and closing the last 10-20% chord with tape (Figure 72) did seem to give broadband corner-noise reductions. Given these promising results, it was decided to mill 4 mm of span off the lower edge of the model and treat the resulting gap the same way as the upper gap. This treatment resulted in a drastic broadband reduction of the corner sources (Figure 73 and Figure 74). Noise reductions up to 10 dB were achieved, which enabled the detection of very low trailing-edge noise levels. This ability to look much “deeper” (i.e., improved dynamic range) is illustrated in Figure 75, which shows the trailing-edge noise spectra for the treated and untreated cases. In the untreated case, only upper limits for the noise levels can be determined because of the dominant corner sources (except at 1.6 kHz). For the treated case, accurate trailing-edge noise levels were determined up to 2 kHz, while the upper limits at higher frequencies were reduced. As an example of the improved dynamic range, at 2-kHz the measured noise levels were approximately 5 dB below the threshold in the untreated case.

## 6 Summary and Conclusions

Aeroacoustic wind-tunnel tests were performed on six airfoils that were candidates for use on small wind turbines. The acoustic measurements were done in NLR's Small Anechoic Wind Tunnel for a range of wind speeds and angles of attack, with and without boundary layer tripping. Besides the airfoil self-noise measurements in a clean tunnel flow, the models were also tested with a turbulence grid in the nozzle to investigate airfoil noise associated with inflow turbulence. A 48-microphone out-of-flow acoustic array was used to locate noise sources and to separate airfoil noise from extraneous wind-tunnel noise. Besides the six candidate airfoils, one airfoil (NACA 0012) was tested for comparison to existing benchmark data from NASA. Before the acoustic tests, the tunnel flow was calibrated in terms of velocities, turbulence intensities, and flow angularity.

The acoustic results indicated that in a clean tunnel flow, trailing-edge noise was dominant for all airfoils. In the untripped condition, several airfoils exhibited intense tones originating from either the suction or the pressure side that could be attributed to laminar boundary-layer vortex-shedding noise. After tripping, the tones disappeared, yielding broadband spectra associated with turbulent boundary-layer trailing-edge noise. Normalizing frequencies and sound levels in terms of  $St = fC/U$  and  $PWL_{norm} = PWL - 10 \cdot \log_{10}(U^m)$  provided the best data collapse for  $m = 4.5$ . This value was slightly lower than the value of  $m = 5$  found in previous studies.

In the case of inflow turbulence, leading-edge noise was dominant for all airfoils, and no difference was observed between the results with and without tripping. Normalization of frequencies and sound levels provided the best data collapse for  $m = 6$ , which was in good agreement with previous studies. Comparison of the acoustic results for different airfoils indicated that inflow turbulence noise levels increased with increasing sharpness of the model leading edge.

From a comparison of array measurements on the suction and pressure side of the model, it appeared that the directivity of both trailing edge and inflow turbulence noise was symmetrical with respect to the model chord. Differences between suction- and pressure-side noise levels that were observed for non-zero angles of attack could be explained by a difference in measurement direction with respect to the chord.

Comparison of the NACA 0012 results with the NASA benchmark data generally showed good agreement in terms of spectral shape and levels. However, the NASA spectra for the tripped condition exhibited a low-frequency hump, which was not observed in the NLR data. No clear explanation was found for this discrepancy, but possible causes might be the difference in trip method or the difference in measurement and processing techniques.

Besides the measurements on the six candidate airfoils and the NACA 0012 reference airfoil, one model was tested with Micro Electro Mechanical System (MEMS) simulators, mounted on the pressure side at 95% chord. Eight different types of MEMS, which can be used on wind-turbine blades to improve the aerodynamic performance, were tested. Although the MEMS were found to have no effect on inflow turbulence noise, broadband trailing-edge noise levels increased by about 5 dB. Depending on frequency, this noise was radiated from the model trailing edge and the MEMS simulator itself. In addition to the broadband increase, the most severe MEMS (solid tabs) produced very intense trailing-edge tones, up to almost 30 dB above the baseline levels. The frequency of these tones was found to be proportional to the tunnel speed. Despite the fact that the MEMS were mounted to the pressure side only, the directivity of the trailing-edge noise appeared to be symmetrical around the model chord.

Finally, a very efficient method was found to suppress extraneous noise from the model-endplate junctions, which in many cases disturbed the measurement of low-level trailing-edge noise. A treatment of porous material in the gaps between the model and the endplates yielded a broadband extraneous noise reduction of up to 10 dB. As a result, the array could look much "deeper," which enabled the detection of very low trailing-edge noise levels.

## 7 References

- 
- 1 M.S. Selig, and B. D. McGranahan: *Wind Tunnel Aerodynamic Tests of Six Airfoils for Use on Small Wind Turbines*, University of Illinois at Urbana-Champaign, NREL SR-500-34515 (2003)
  - 2 T. F. Brooks, D. S. Pope, and M. A. Marcolini: *Airfoil Self-Noise and Prediction*, NASA Reference Publication 1218 (1989)
  - 3 O. de Vries: Handbook LST, Part 1: *Test set-up, data-acquisition and data-processing*, NLR-TR-95129 L (1995)
  - 4 *APROPOS user's guide*, NLR note, AF-96-006 (1996)
  - 5 O. de Vries: Handbook LST, Part 2: *Force measurements and derivation of equations*, NLR-TR-95129 L (1995)
  - 6 O. de Vries: Handbook LST, Part 3: *Pressure measurements; miscellaneous tests*, NLR-TR-95129 L (1995)
  - 7 H. Holthusen and H. Smit: *A new data-acquisition system for microphone array measurements in wind tunnels*, AIAA paper 2001-2169 (2001)
  - 8 P. Sijtsma: *Description and user's guide of the computer program SOLACAN 4.0 and related programs*, NLR-TR-2001-156 (2001)
  - 9 R.K. Amiet: *Refraction of sound by a shear layer*, Journal of Sound and Vibration, Vol. 58, No. 2, pp 467-482 (1978)
  - 10 P. Sijtsma: *Calculating absolute source powers from phased array measurements*, NLR-CR-2002-358, 2002
  - 11 S. Oerlemans and P. Sijtsma: *Determination of absolute levels from phased array measurements using spatial source coherence*, AIAA paper 2002-2464 (2002)
  - 12 A. Pelletier and T. J. Mueller: *Effect of Endplates on Two-Dimensional Airfoil Testing at Low Reynolds Number*, Journal of Aircraft, Vol. 38, No. 6, pp 1056-1059 (2001)
  - 13 S. Wagner, R. Bareiss, and G. Guidati: *Wind Turbine Noise*, Springer-Verlag (1996)
  - 14 W. K. Blake: *Mechanics of Flow-Induced Sound and Vibration*, Academic Press (1986)
  - 15 T. F. Brooks and W. M. Humphreys: *Effect of Directional Array Size on the Measurement of Airframe Noise Components*, AIAA paper 99-1958 (1999)
  - 16 Personal communication with T. F. Brooks (2003)
  - 17 D. T. Yen-Nakafuji, C. P. van Dam, R. L. Smith, and S. D. Collins: *Active Load Control for Airfoils Using Microtabs*, Journal of Solar Energy Engineering, Vol. 123, pp. 282-289 (2001)
  - 18 C. P. van Dam, D. T. Yen, R. L. Smith, and S. D. Collins: *Microfabricated Translational Stages for Control for Aerodynamic Loading*, U.S. Patent Application 20030218102 (2003)

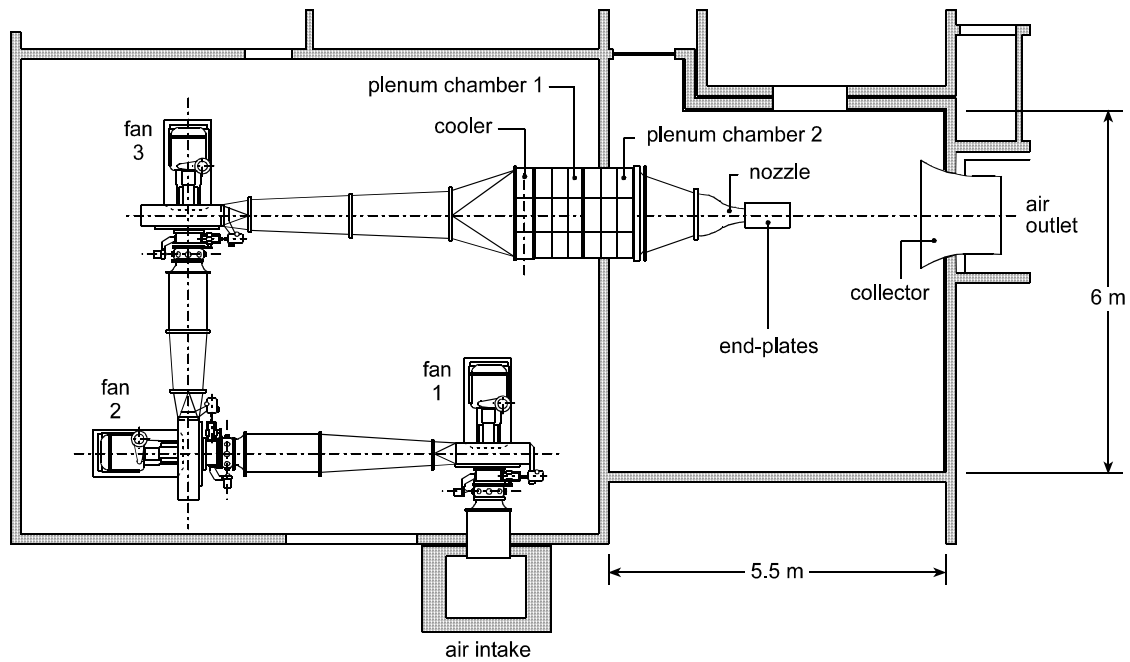


Figure 1. General overview of the Small Anechoic Wind Tunnel KAT

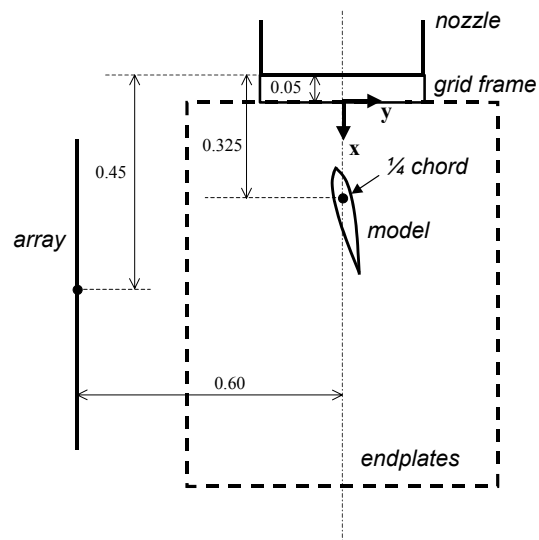


Figure 2. Top view of KAT set up for airfoil noise measurements. The microphone array could be located on both suction (shown) or pressure side of the model. The origin of the z-axis is located at the tunnel axis. Dimensions in meters (not to scale)

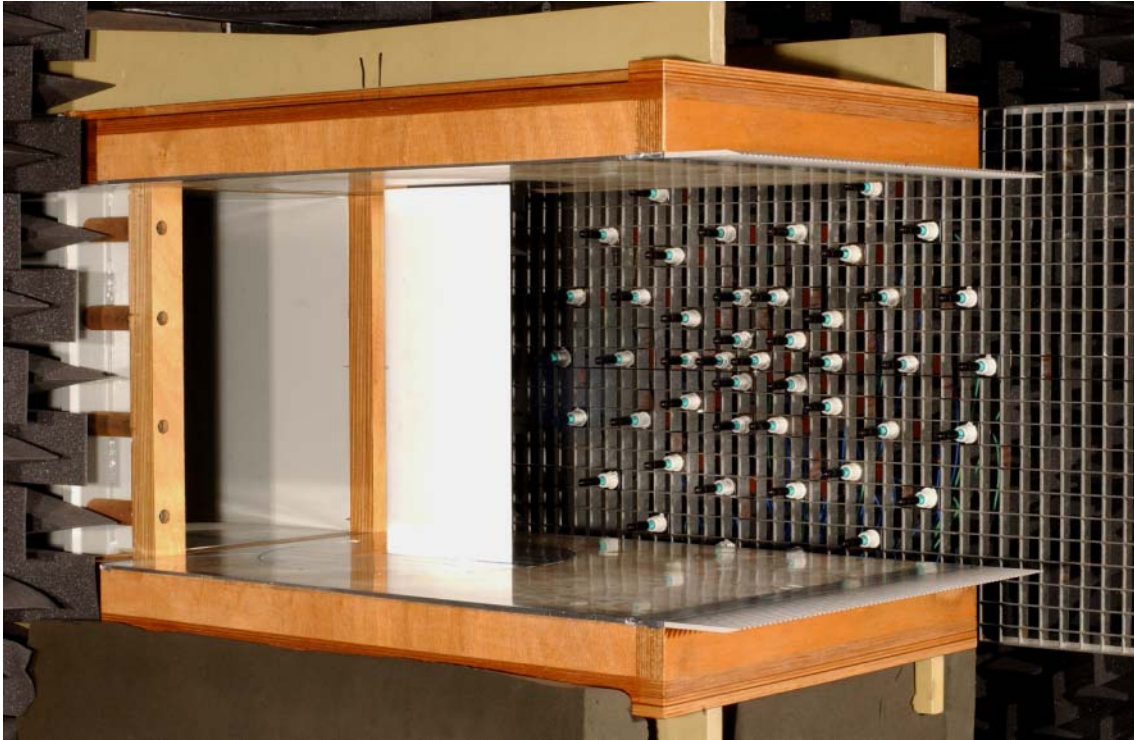


Figure 3. KAT set-up with lined endplates and microphone array (on pressure side)

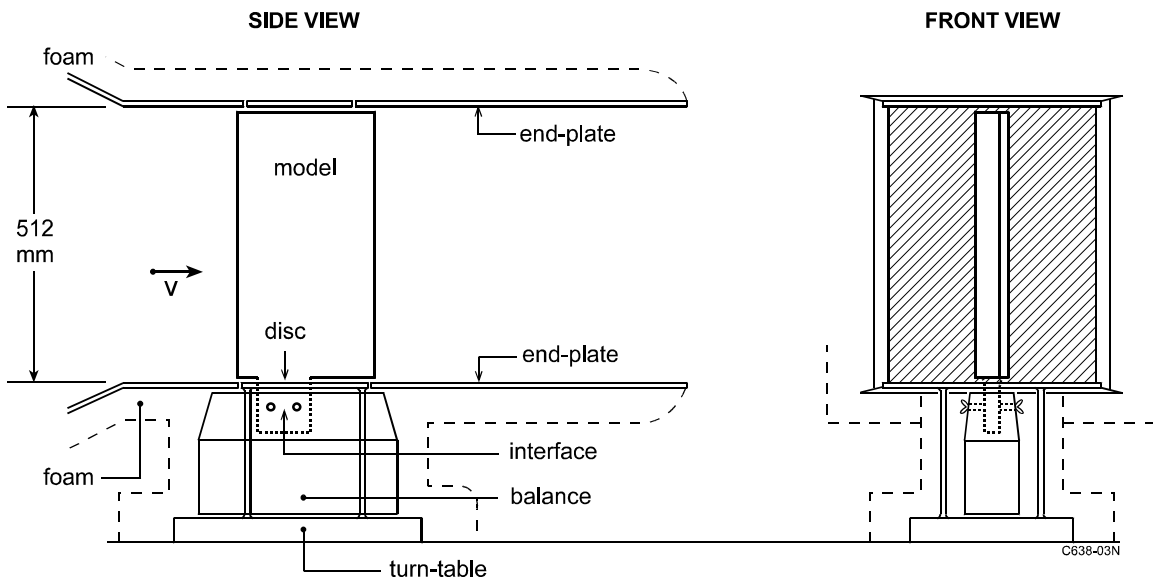


Figure 4. KAT set-up for balance measurements



**Figure 5. Hot-wire probe in empty test section**

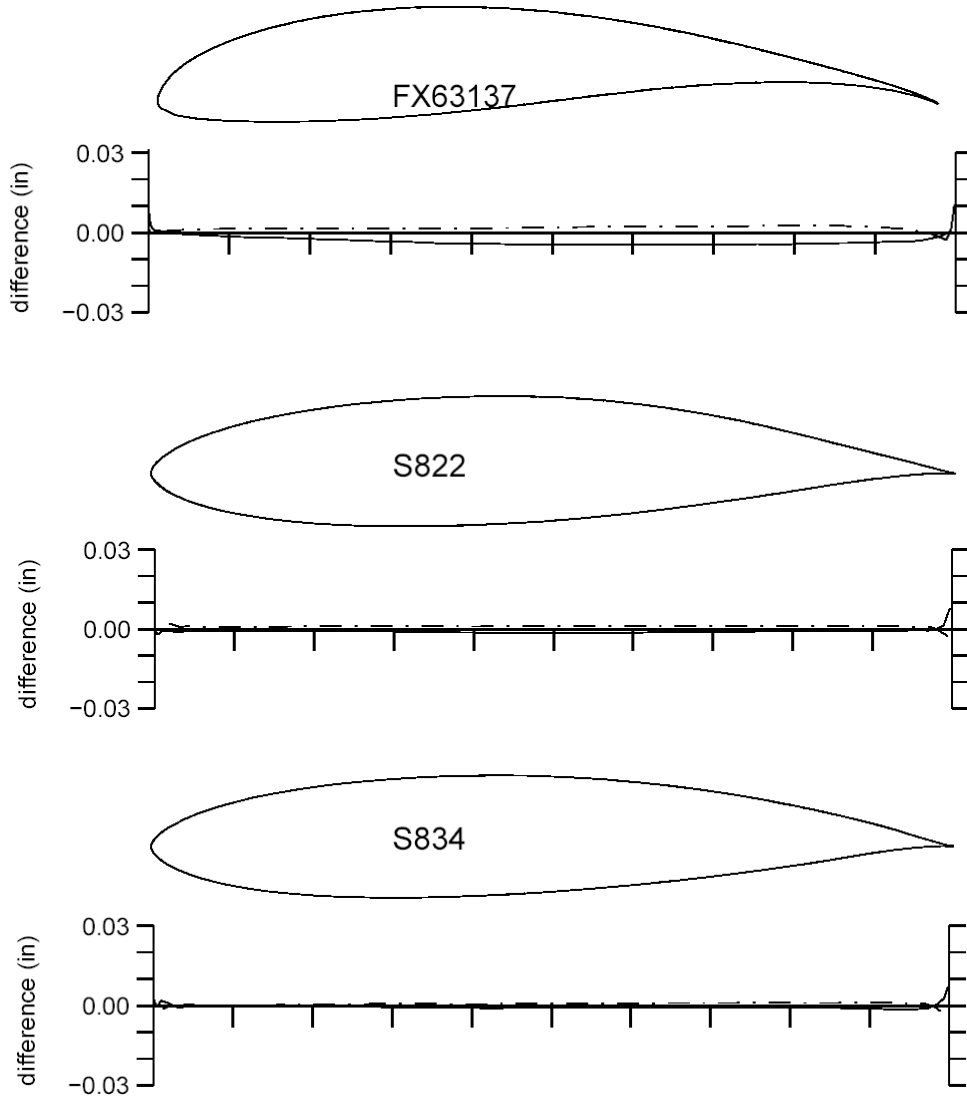
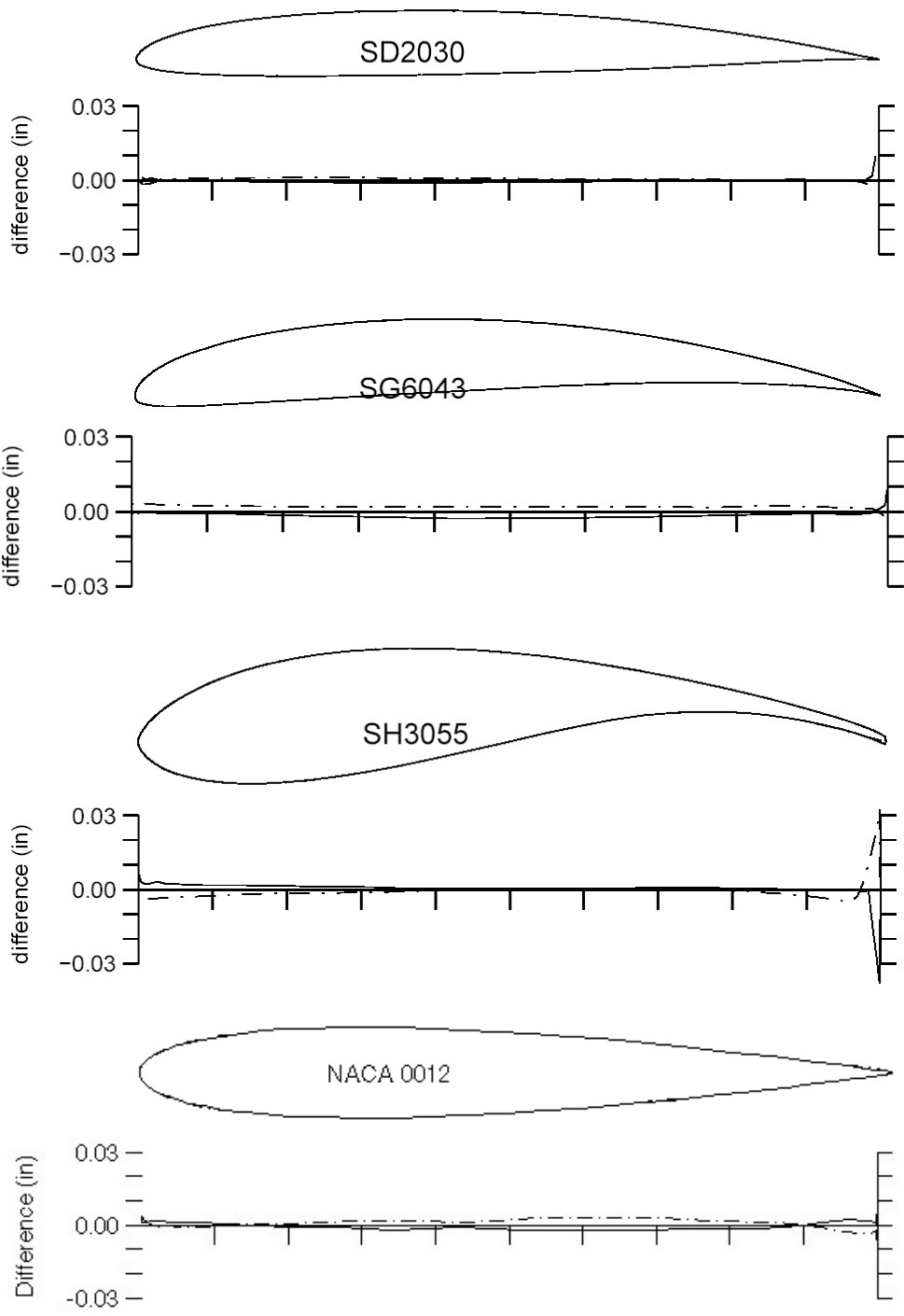


Figure 6 (part 1 of 2). Overview of tested airfoils including deviation from specified coordinates



**Figure 6 (part 2 of 2). Overview of tested airfoils including deviation from specified coordinates**



**Figure 7. Photograph of tested airfoil models (NACA 0012 model in white)**

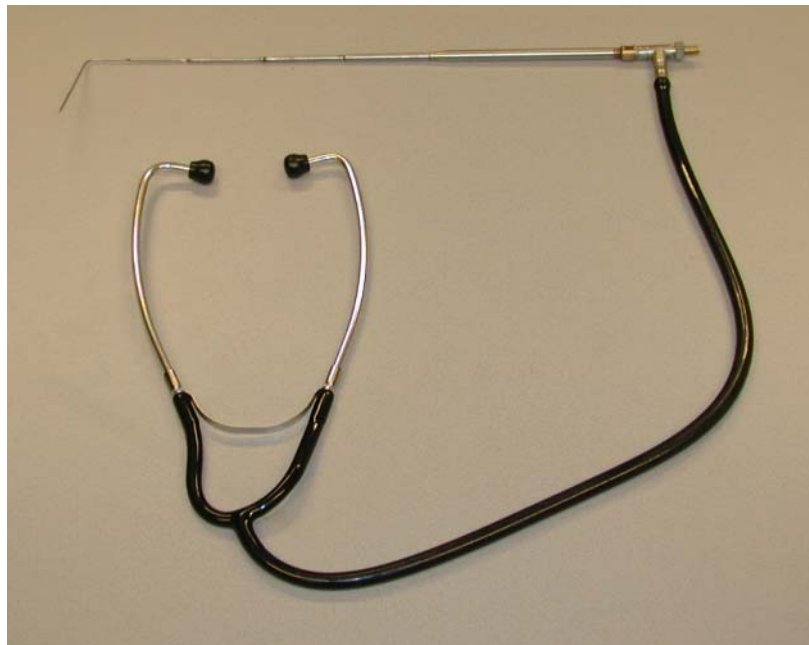


**Figure 8. Stethoscope used for observing boundary-layer transition**

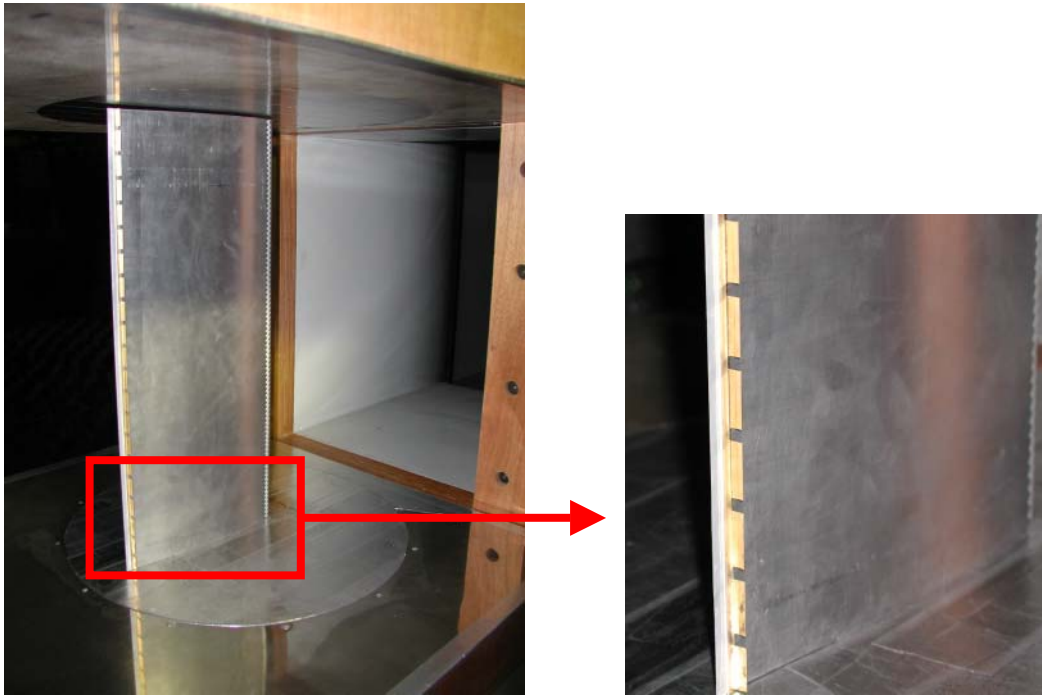


Figure 9. MEMS attached to S822 model

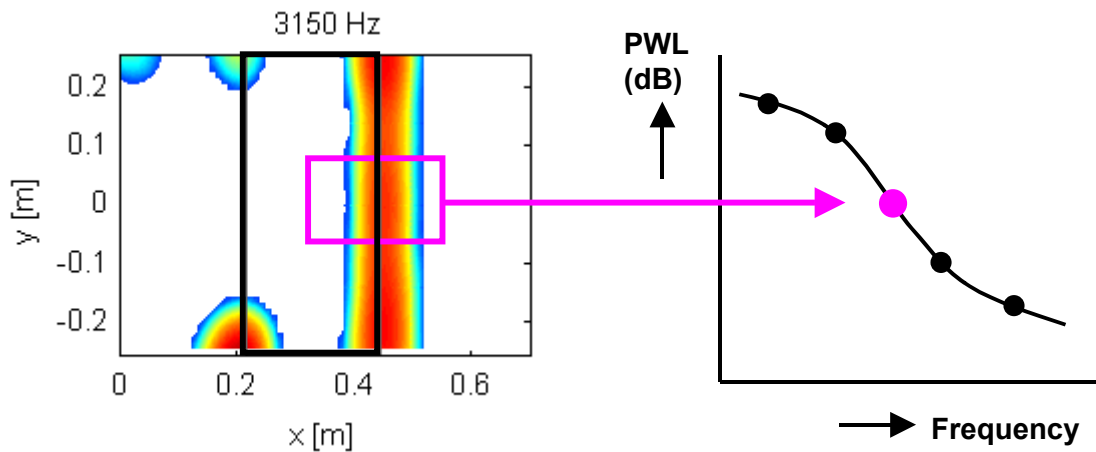


Figure 10. Acoustic source plot (left) indicating noise source locations in the plane of the model. The black line indicates the model contour; flow goes from left to right. The pink line indicates the trailing-edge integration contour that was used to translate acoustic source plots to airfoil noise spectra. For measurements with grid, a leading-edge integration contour was used.

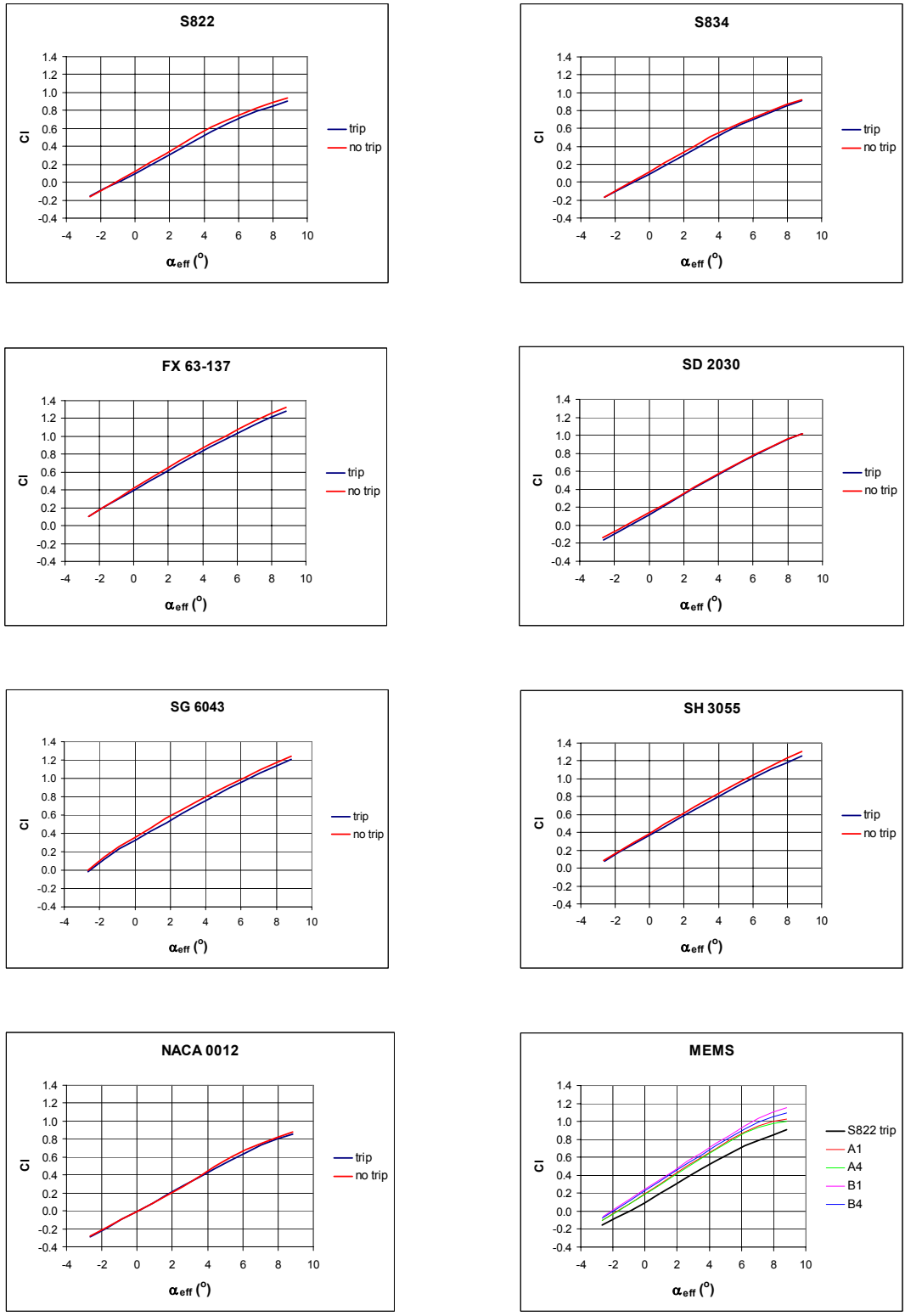


Figure 11. Lift curves for different airfoils (with and without trip) and for #1 and #4 MEMS, obtained without the turbulence grid in the nozzle

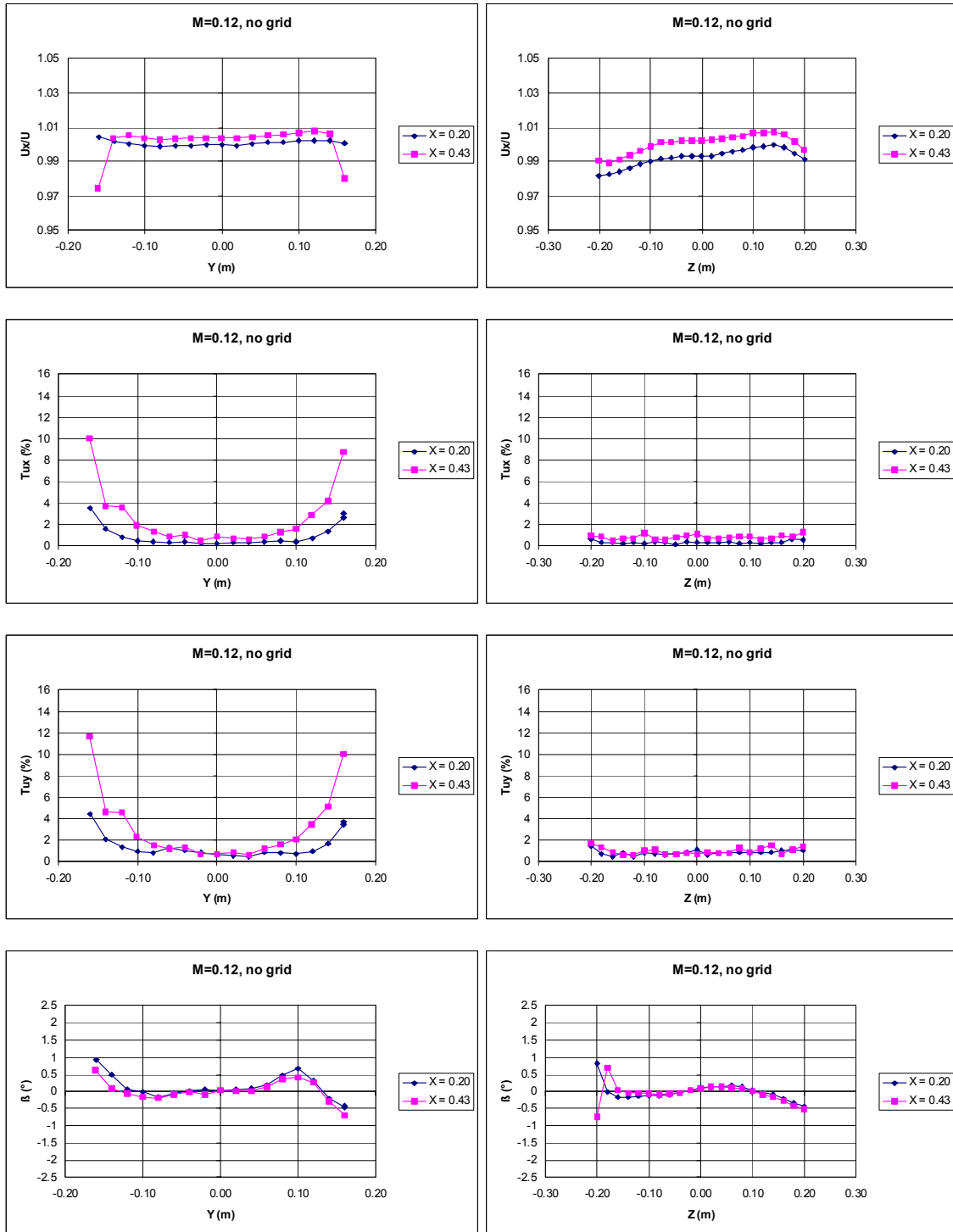


Figure 12. Tunnel calibration results for M = 0.12 without turbulence grid

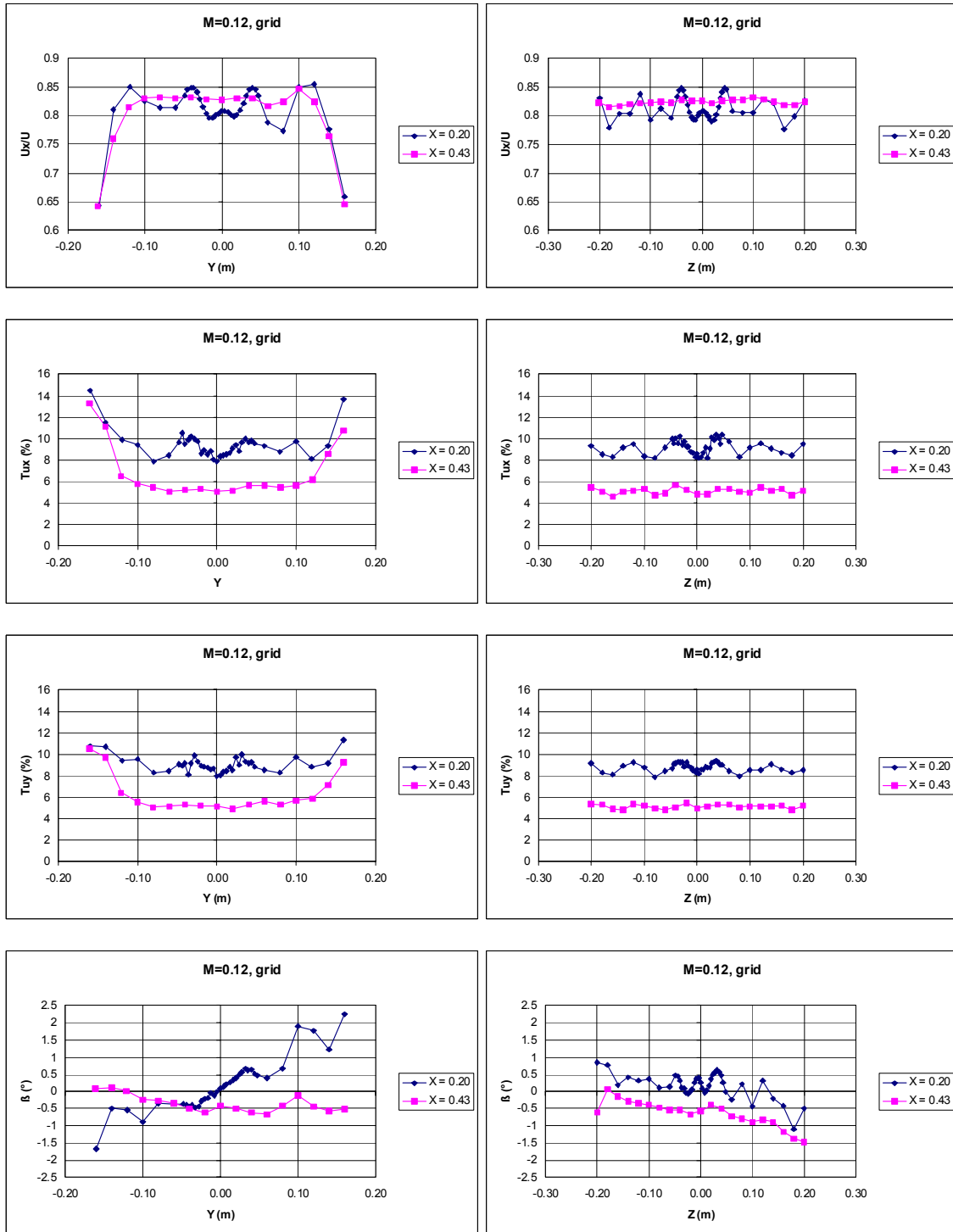


Figure 13. Tunnel calibration results for M = 0.12 with turbulence grid

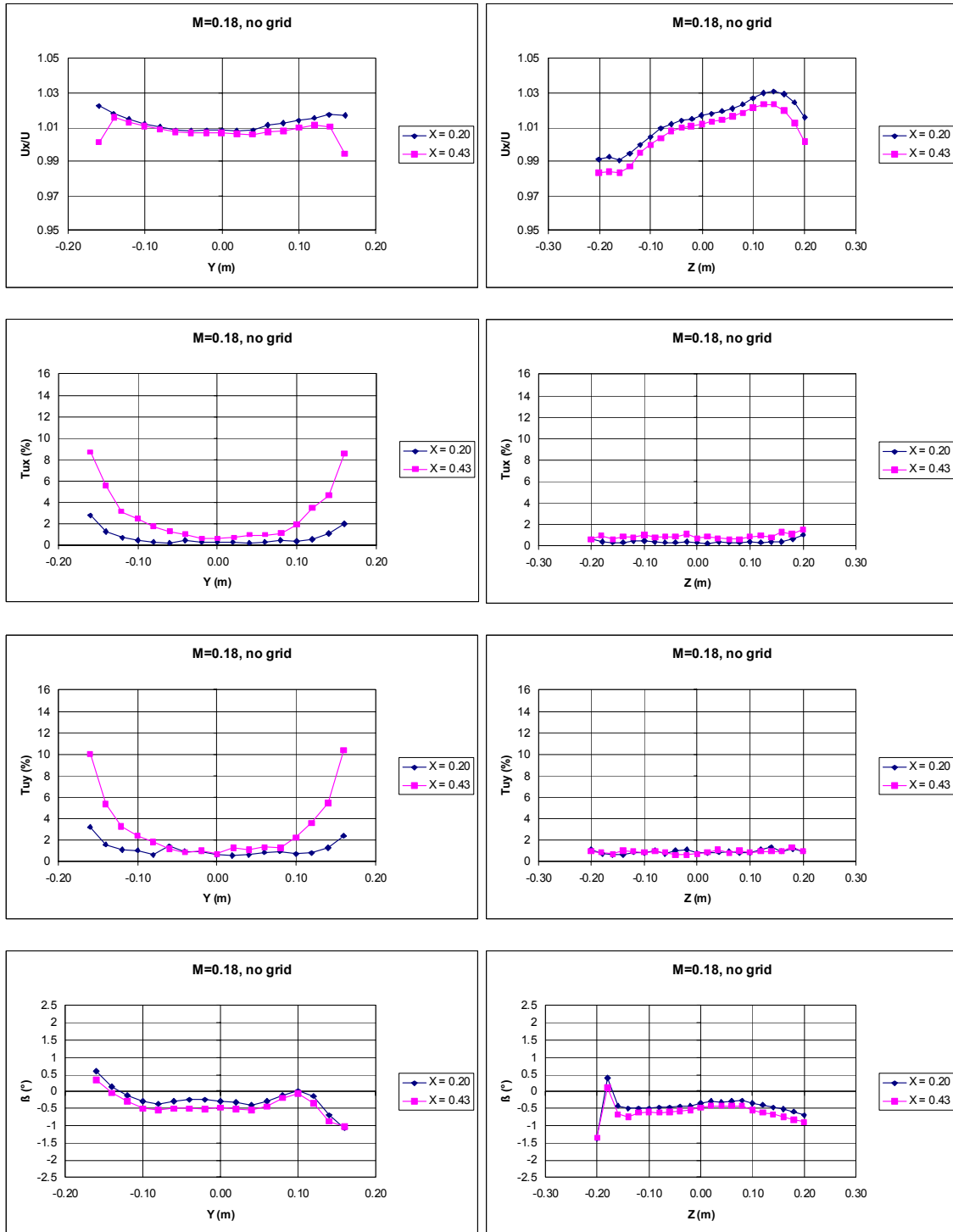


Figure 14. Tunnel calibration results for M = 0.18 without turbulence grid

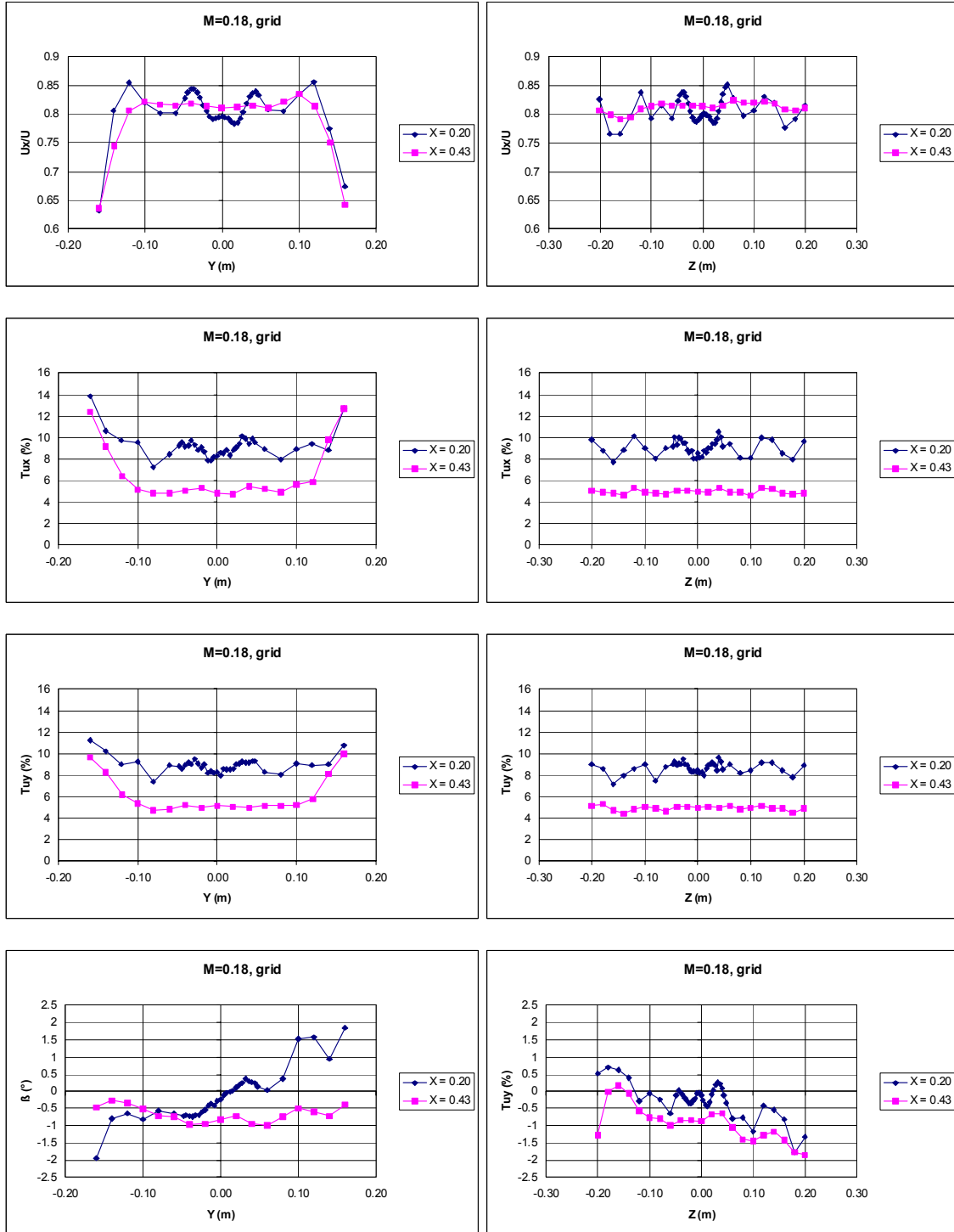
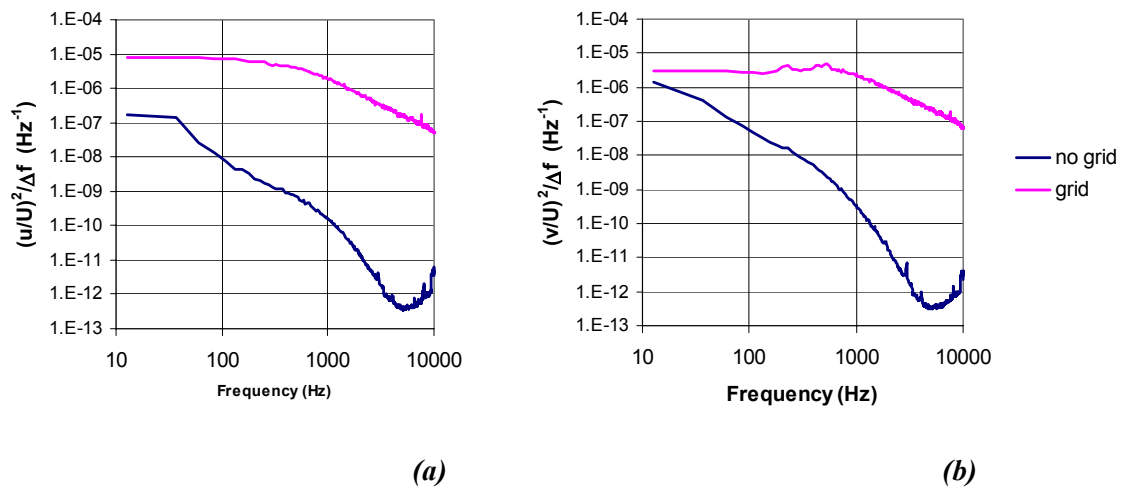


Figure 15. Tunnel calibration results for M = 0.18 with turbulence grid



**Figure 16. Axial (a) and lateral (b) turbulence spectra at  $(x, y, z) = (0.2, 0, 0)$  for  $M = 0.12$**

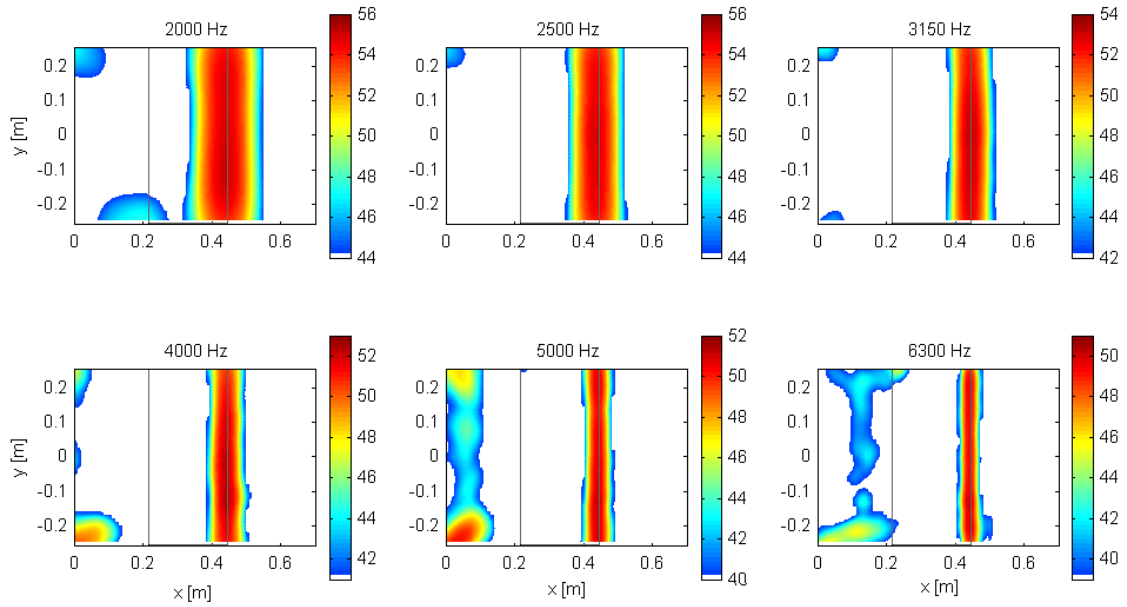


Figure 17. Trailing-edge noise from NACA 0012 airfoil without trip, without turbulence grid, at a tunnel speed of 39.6 m/s and  $\alpha = 0^\circ$  (array on pressure side)

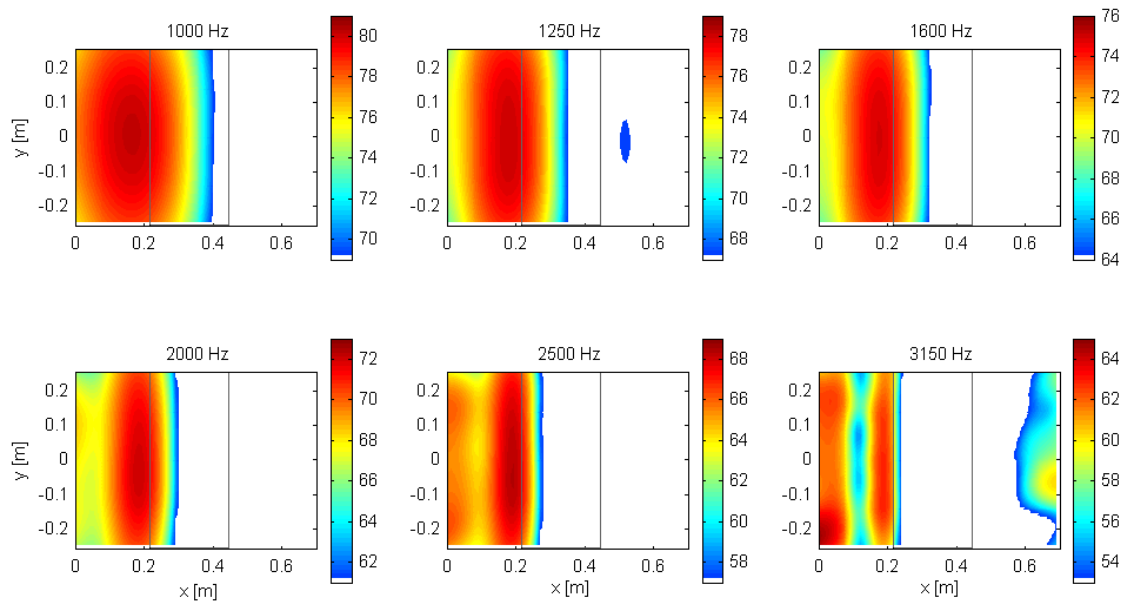


Figure 18. Leading-edge noise from SD 2030 airfoil with trip, with turbulence grid, at a tunnel speed of 32.0 m/s and  $\alpha = 18^\circ$  (array on suction side)

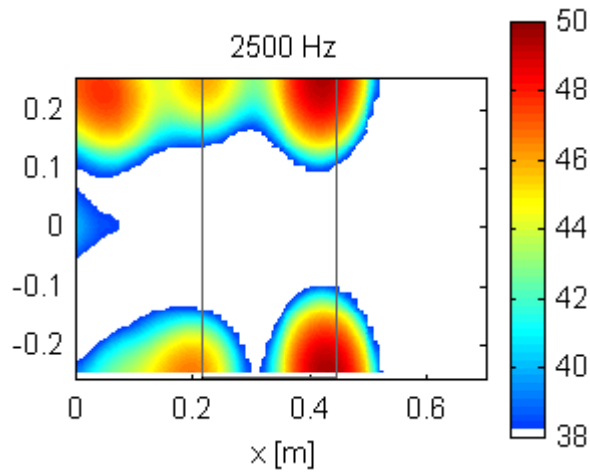


Figure 19. Acoustic source plot for tripped NACA 0012 airfoil at 31.7 m/s and  $\alpha = 16.5^\circ$  (array on suction side), illustrating presence of extraneous sources at model-endplate junctions (“corner sources”)

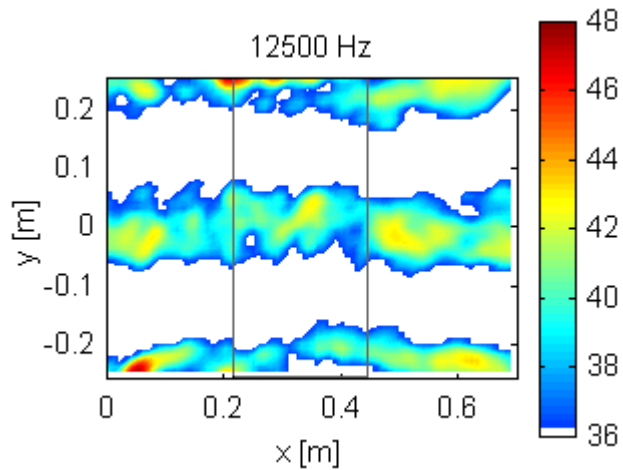


Figure 20. Acoustic source plot for tripped NACA 0012 airfoil at 39.6 m/s and  $\alpha = 9.1^\circ$  (array on suction side), illustrating presence of background noise other than corner sources

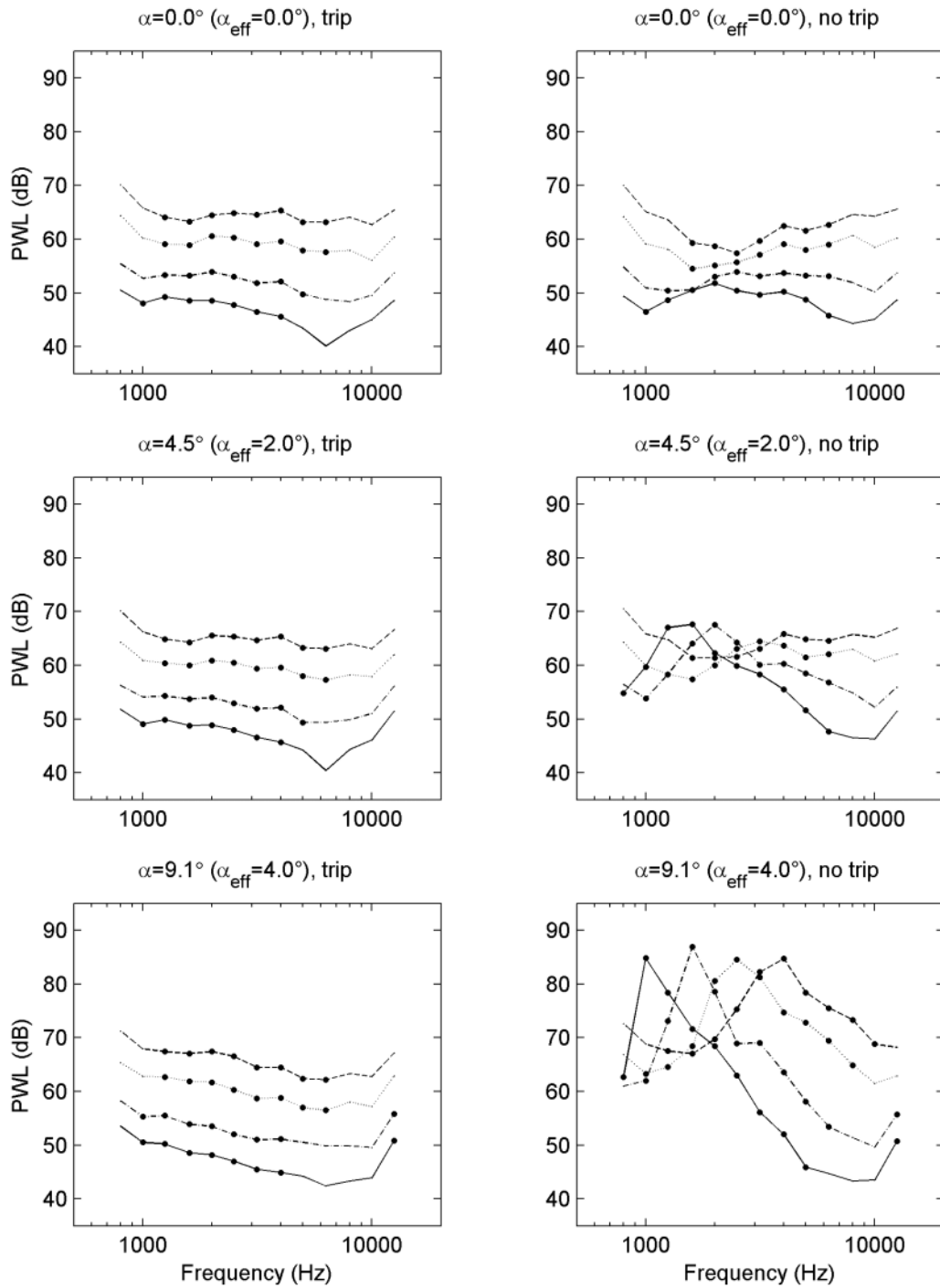


Figure 21 (part 1 of 2). Trailing-edge noise spectra for NACA 0012 airfoil (array on suction side),  $\underline{\quad}$  = 31.7 m/s;  $\underline{\quad}$  = 39.6 m/s;  $\dots$  = 55.5 m/s;  $\underline{\quad}$  = 71.3 m/s

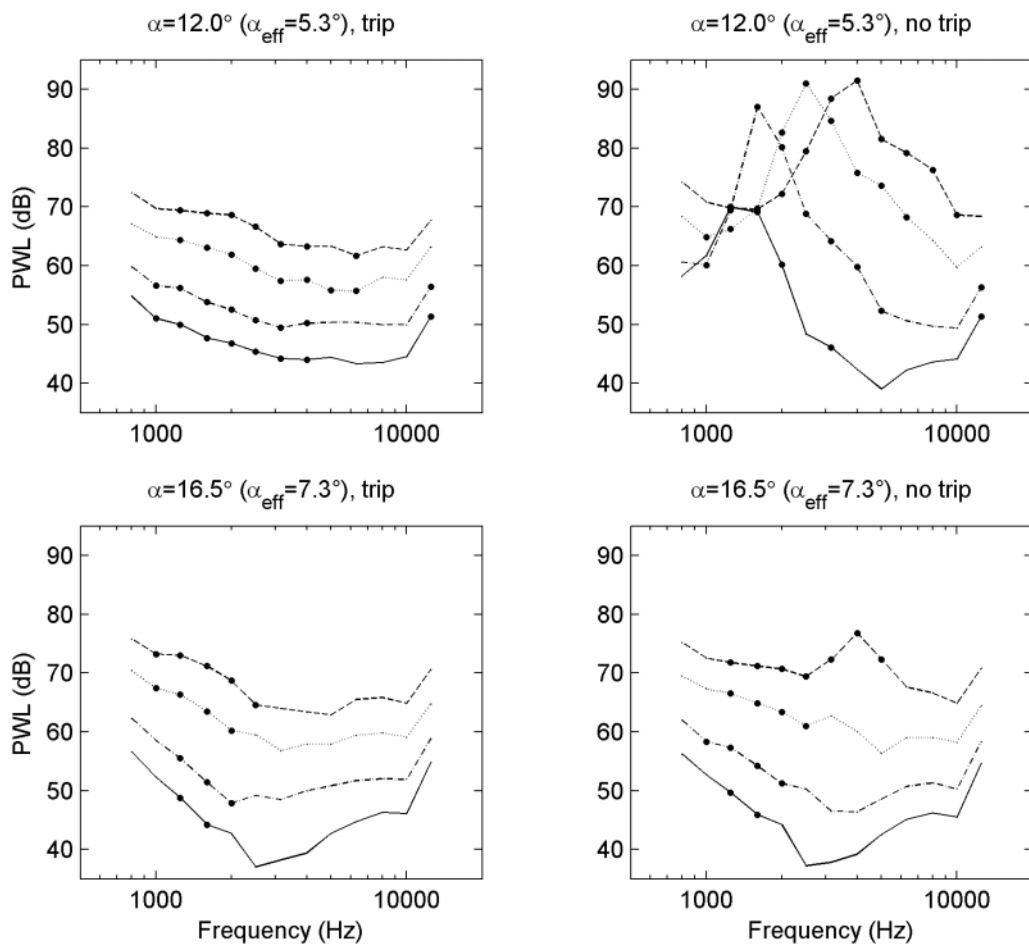


Figure 21 (part 2 of 2). Trailing-edge noise spectra for NACA 0012 airfoil (array on suction side), \_\_\_ = 31.7 m/s; - - = 39.6 m/s; ... = 55.5 m/s; - . = 71.3 m/s

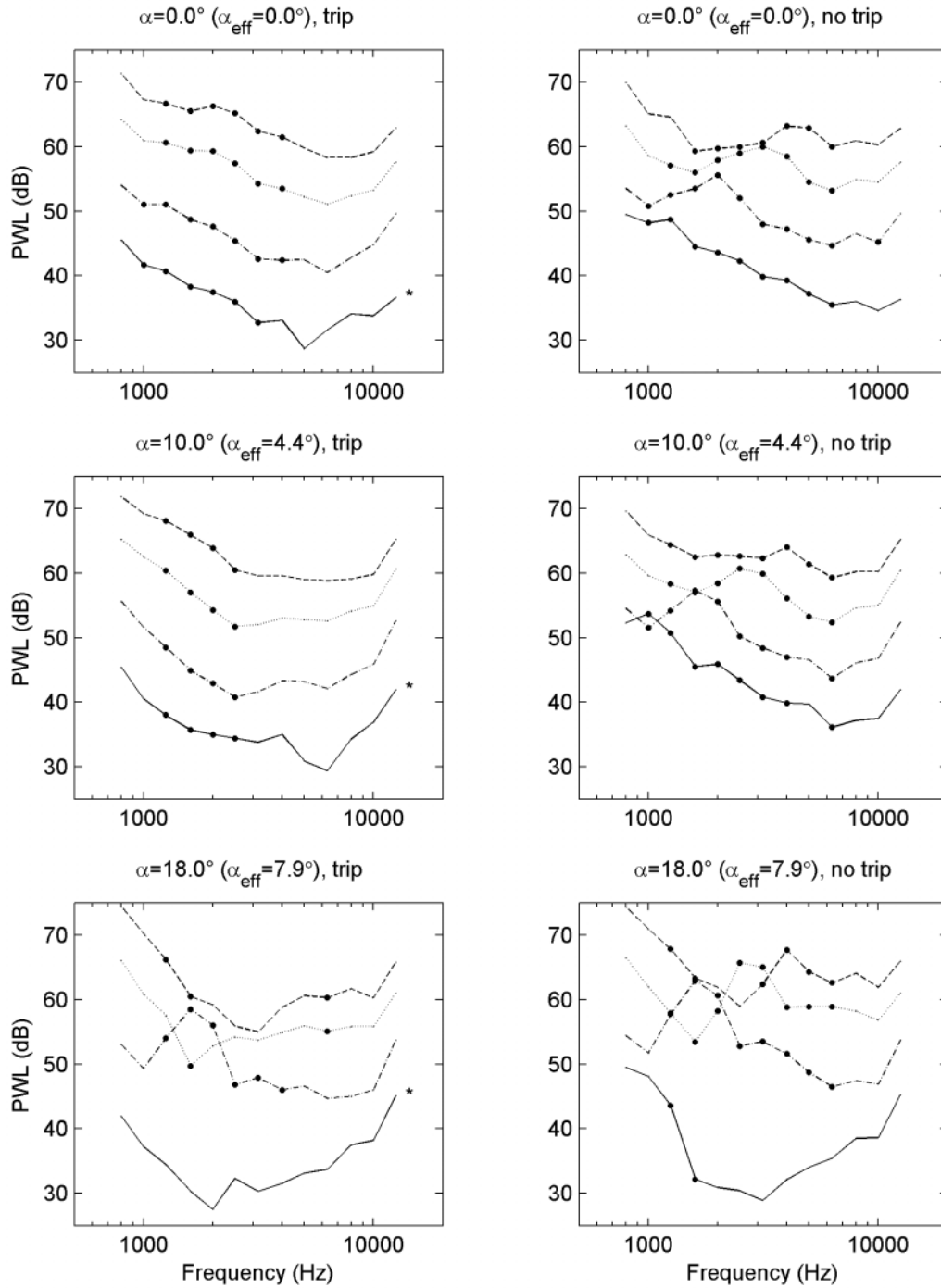


Figure 22. Trailing-edge noise spectra for S822 airfoil (array on suction side)  $\underline{\quad}$  = 22.4 m/s;  $\underline{\quad}$  = 32.0 m/s;  $\dots$  = 47.9 m/s;  $\underline{\quad}$  = 63.9 m/s. \* indicates a trip thickness of 0.5 mm

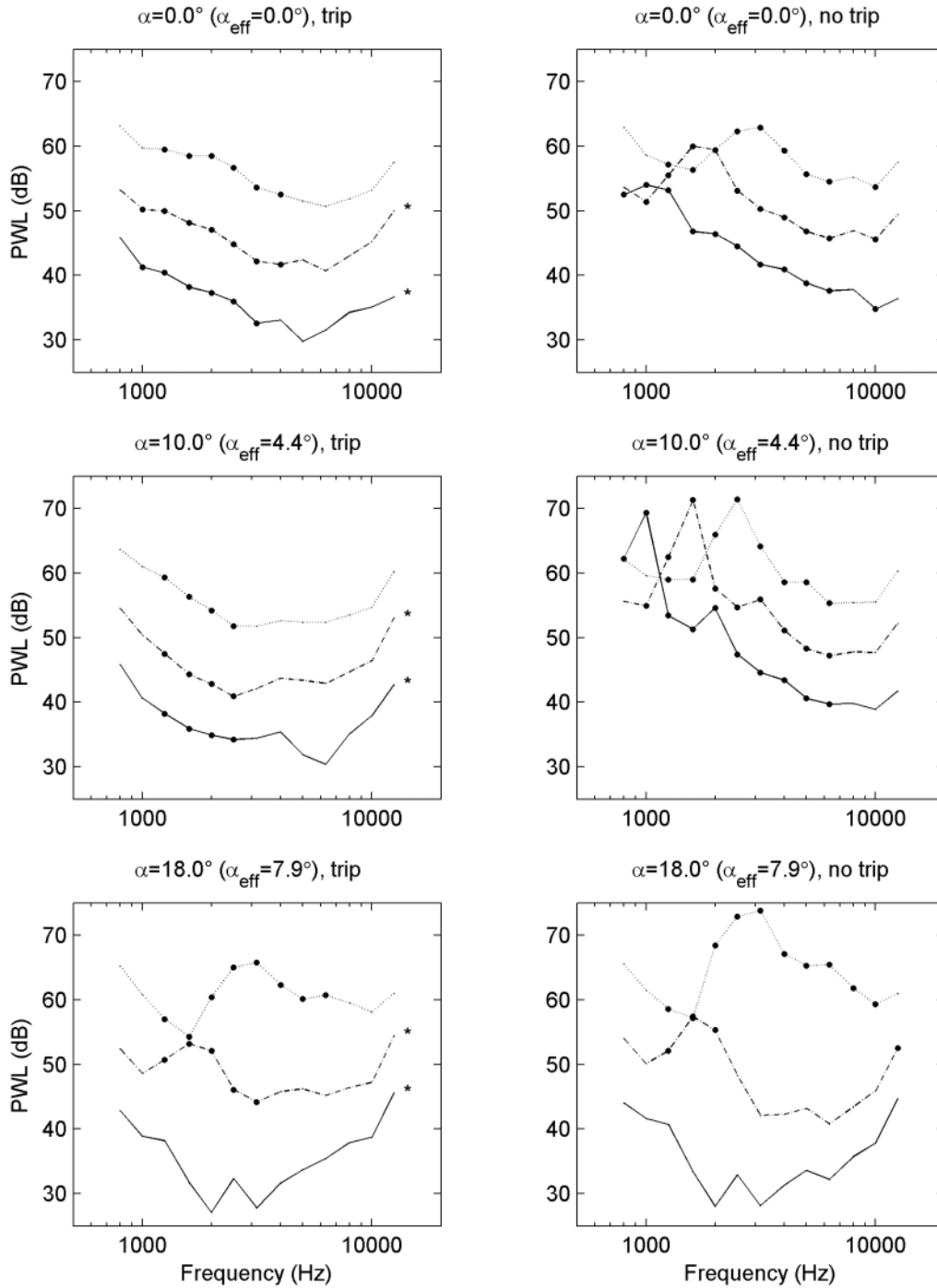


Figure 23. Trailing-edge noise spectra for S834 airfoil (array on suction side)  $\underline{\quad}$  = 22.4 m/s;  $\underline{\quad}$  = 32.0 m/s;  $\dots$  = 47.9 m/s \* indicates a trip thickness of 0.3 mm

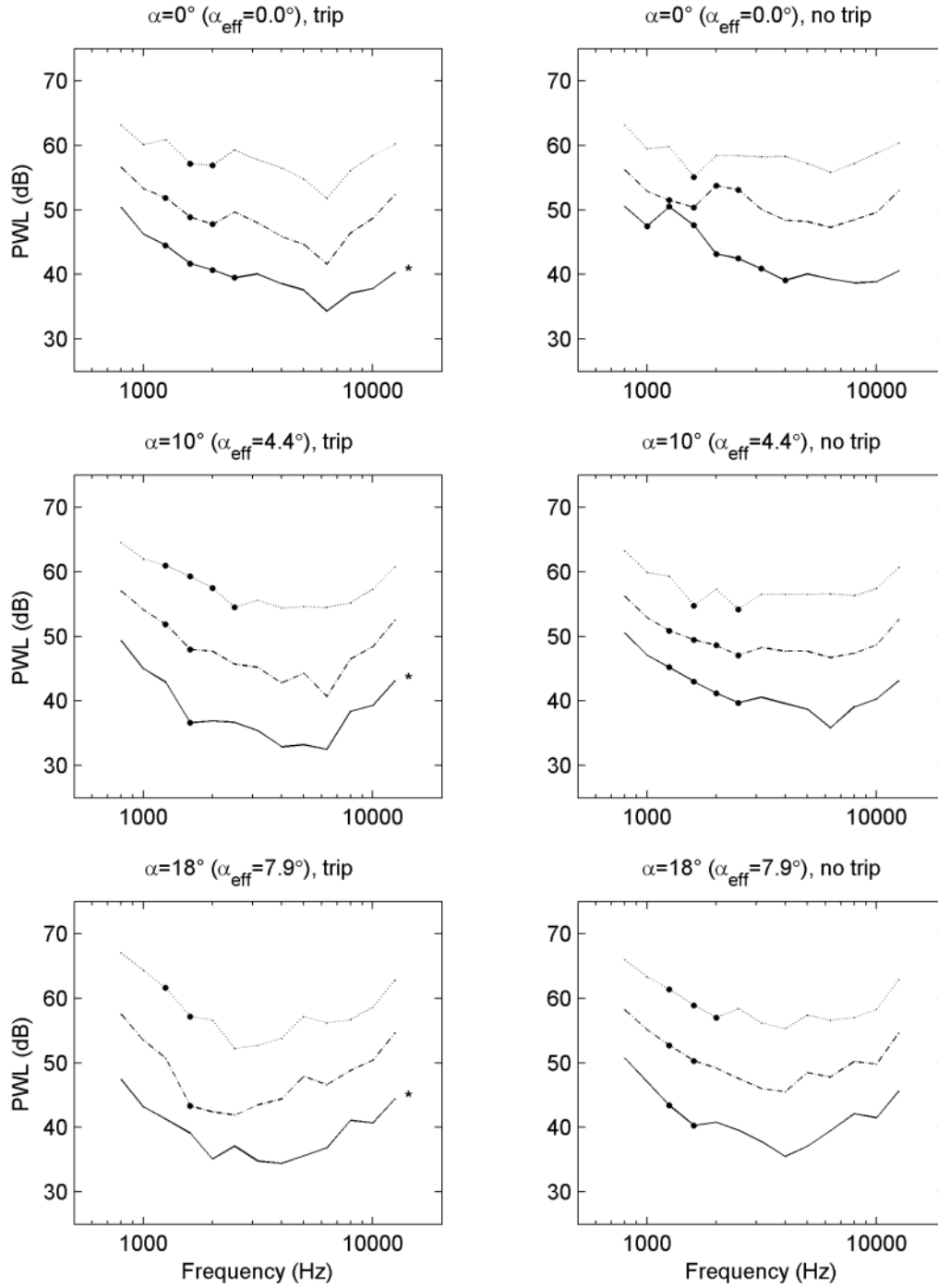


Figure 24. Trailing-edge noise spectra for FX 63-137 airfoil (array on suction side)  $\underline{\quad}$  = 22.4 m/s;  $\underline{\quad}$  = 32.0 m/s;  $\dots$  = 47.9 m/s \* indicates a trip thickness of 0.5 mm

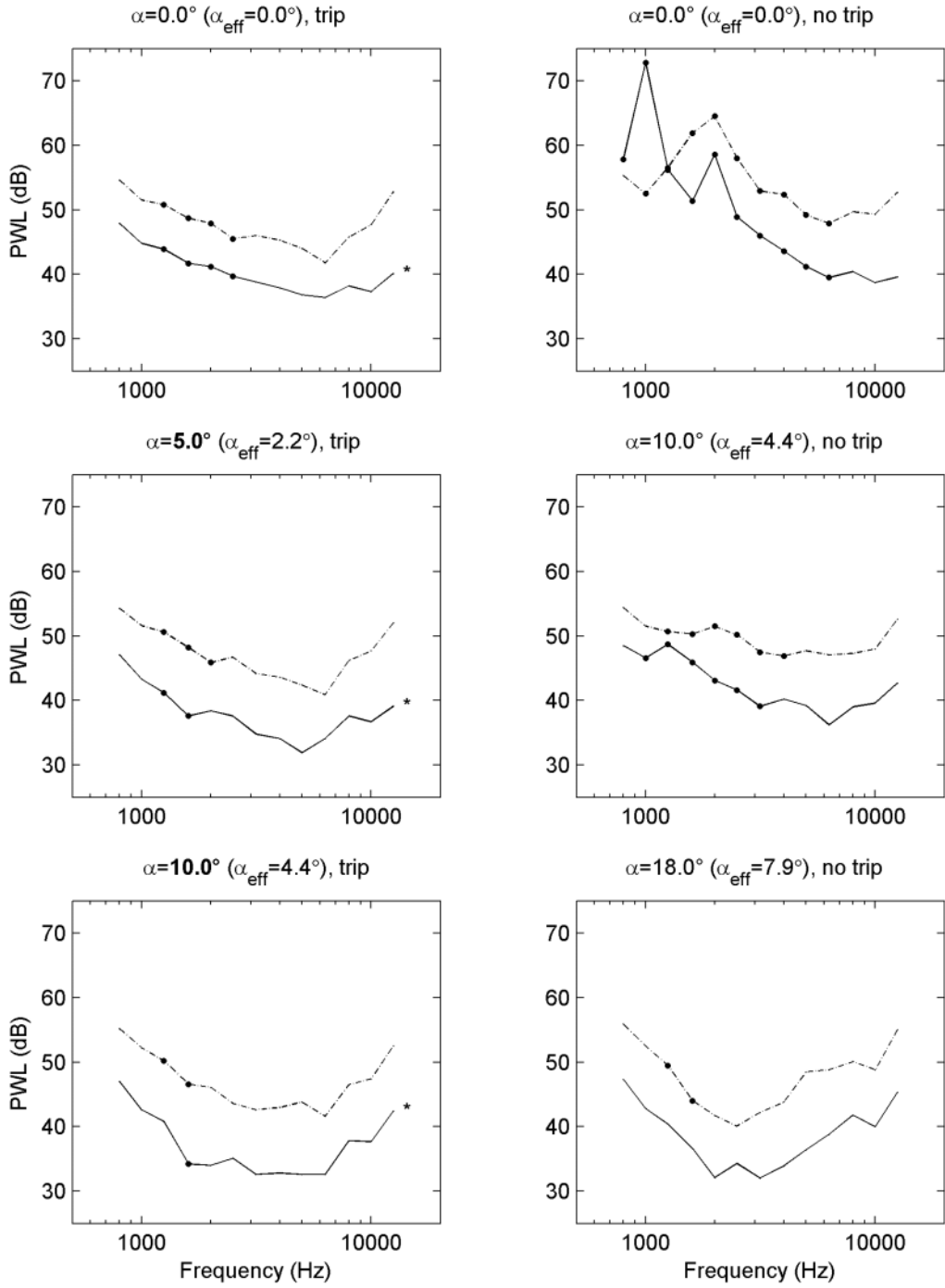


Figure 25. Trailing-edge noise spectra for SG 6043 airfoil (array on suction side)  $\underline{\quad}$  = 22.4 m/s;  $\underline{\quad}$  = 32.0 m/s \* indicates a trip thickness of 0.5 mm

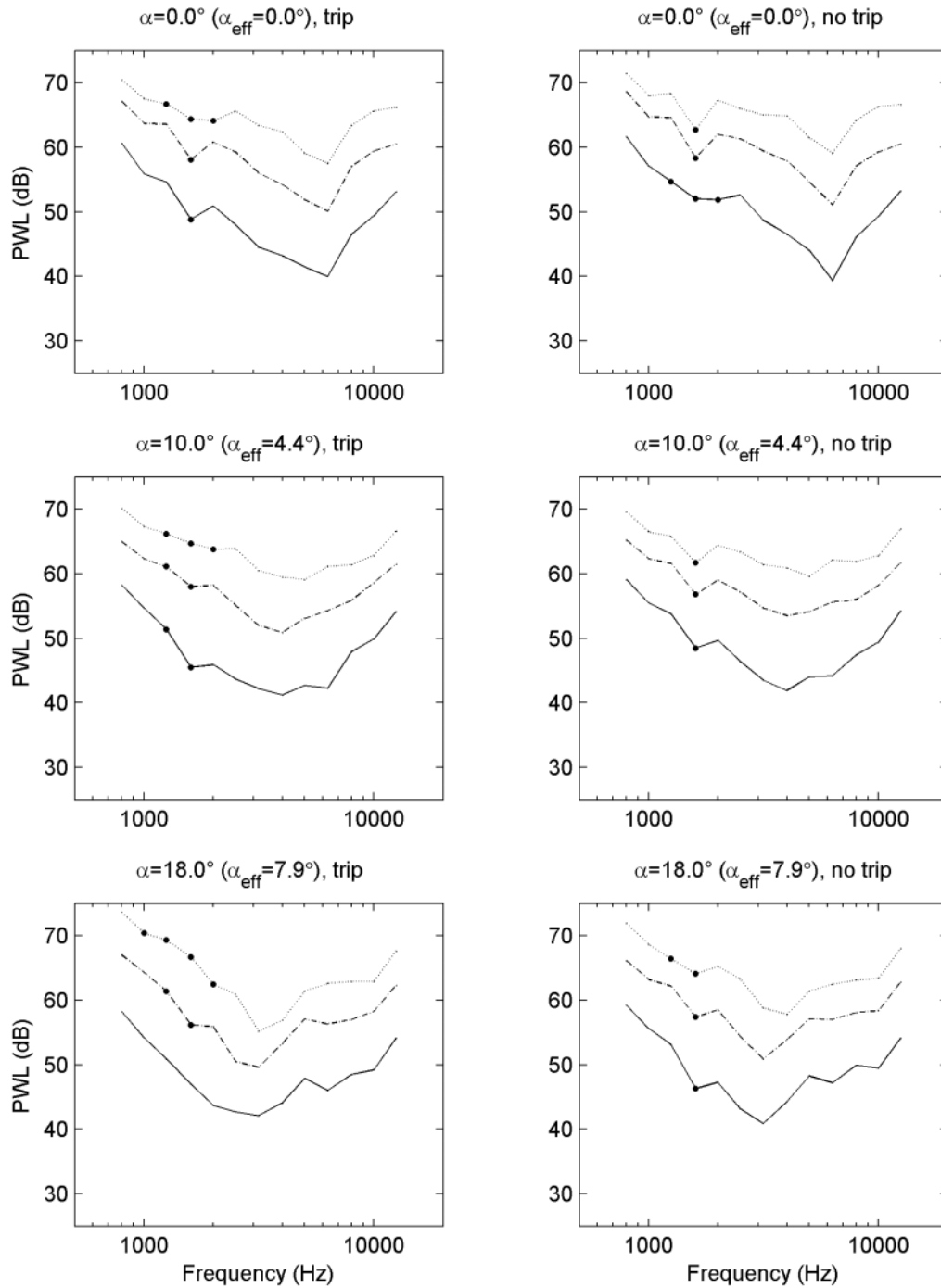


Figure 26. Trailing-edge noise spectra for SH 3055 airfoil (array on suction side)  $\underline{\quad}$  = 32.0 m/s;  $\underline{\quad}$  = 47.9 m/s;  $\dots$  = 64.0 m/s

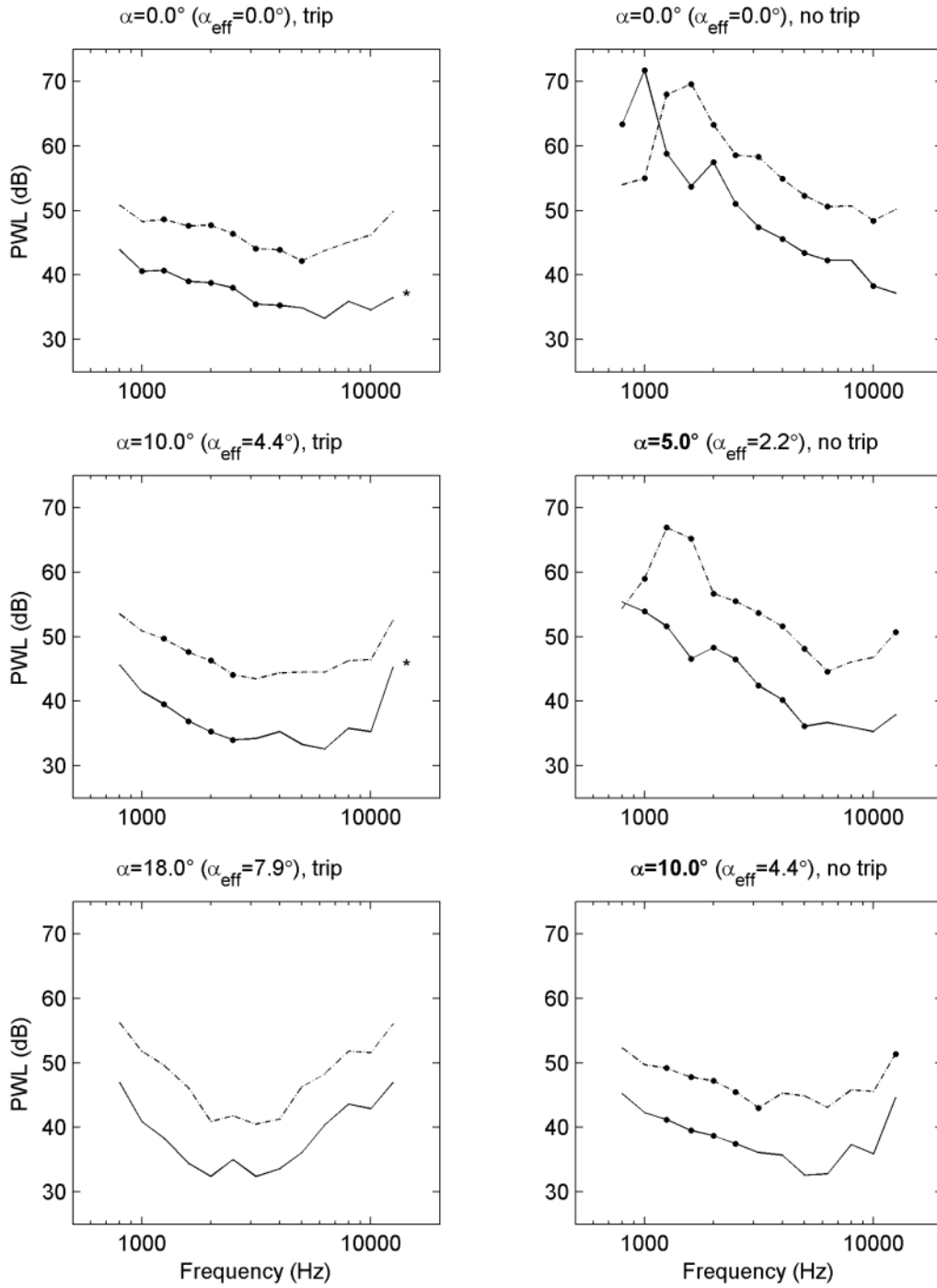


Figure 27. Trailing-edge noise spectra for SD 2030 airfoil (array on suction side)  $\underline{\quad}$  = 22.4 m/s;  $\underline{\quad}$  = 32.0 m/s \* indicates a trip thickness of 0.5 mm

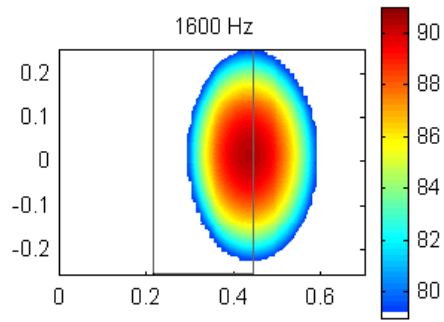


Figure 28. Acoustic source plot for untripped NACA 0012 airfoil at 39.6 m/s and  $\alpha = 9.1^\circ$  (array on suction side), showing the position of the noise source responsible for the spectral peak at 1.6 kHz

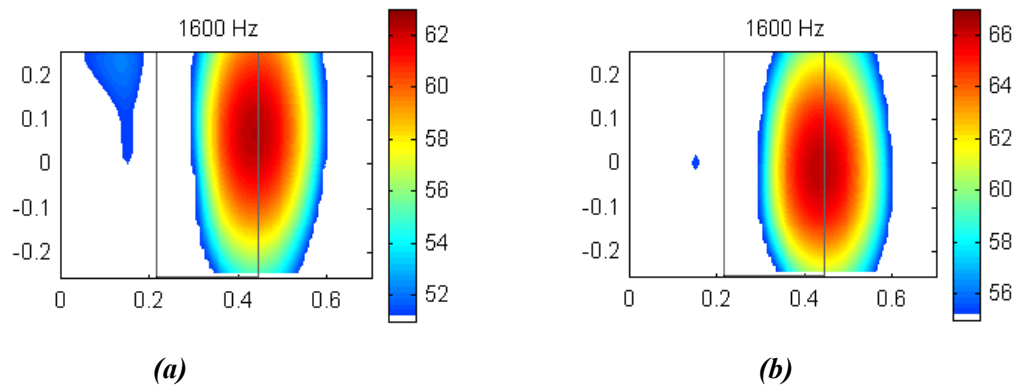
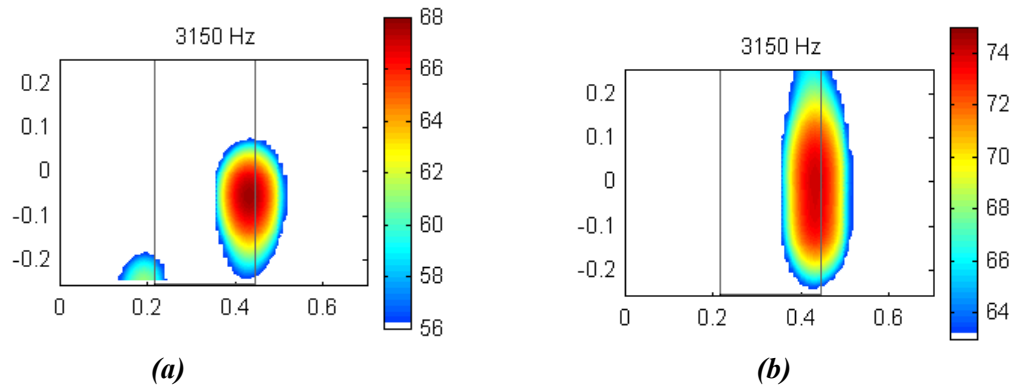


Figure 29. Acoustic source plot for tripped (a) and untripped (b) S822 airfoil at 32.0 m/s and  $\alpha = 18^\circ$  (array on suction side). The tripped case shows an atypical (i.e., asymmetric) source distribution.



**Figure 30. Acoustic source plot for tripped (a) and untripped (b) S834 airfoil at 47.9 m/s and  $\alpha = 18^\circ$  (array on suction side). The tripped case shows an atypical (i.e., asymmetric) source distribution.**

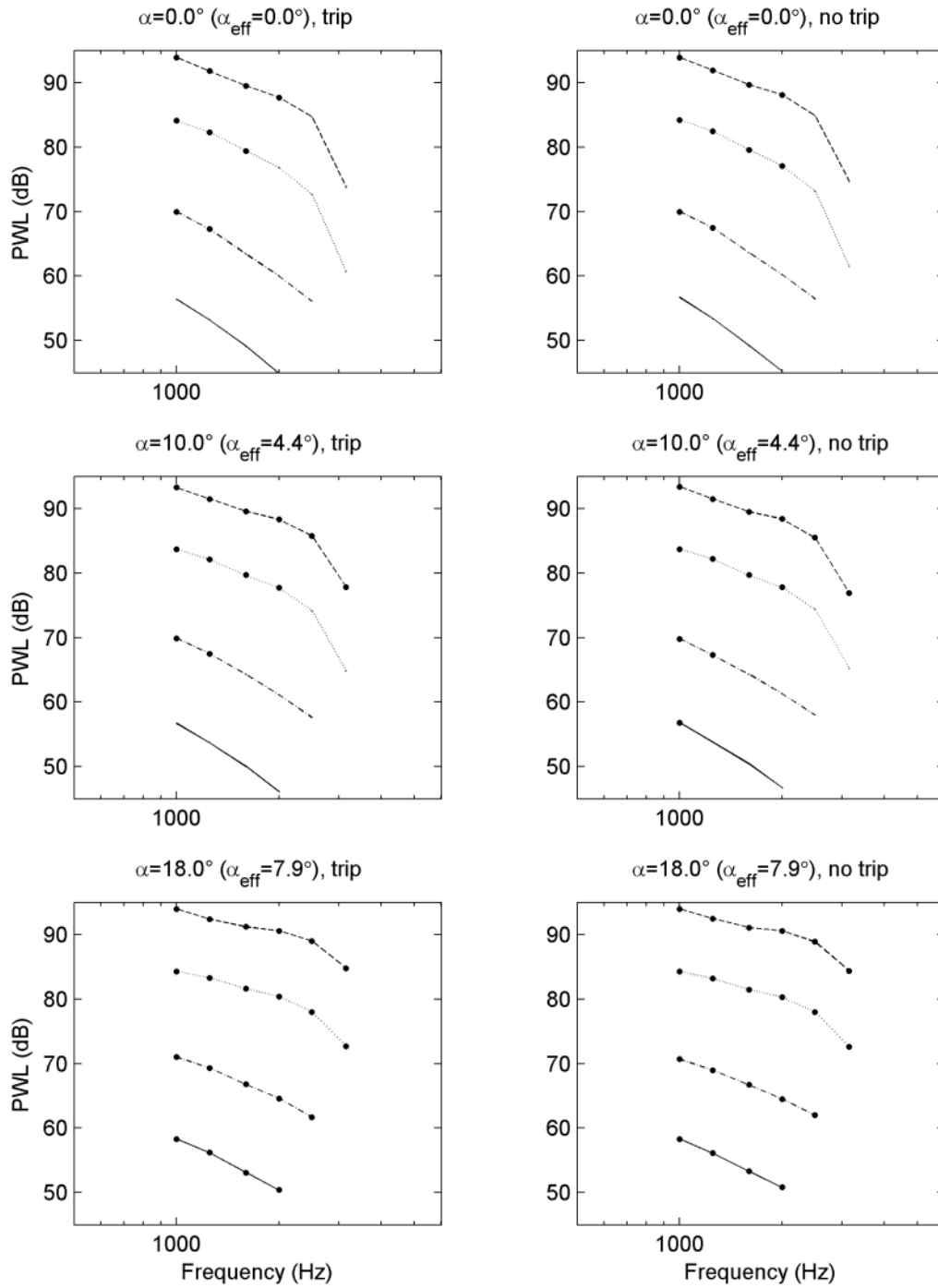


Figure 31. Leading-edge noise spectra for S822 airfoil (array on suction side)  $\underline{\quad}$  = 22.4 m/s;  $\underline{\quad}$  = 32.0 m/s;  $\dots$  = 47.9 m/s;  $\underline{\quad}$  = 63.9 m/s

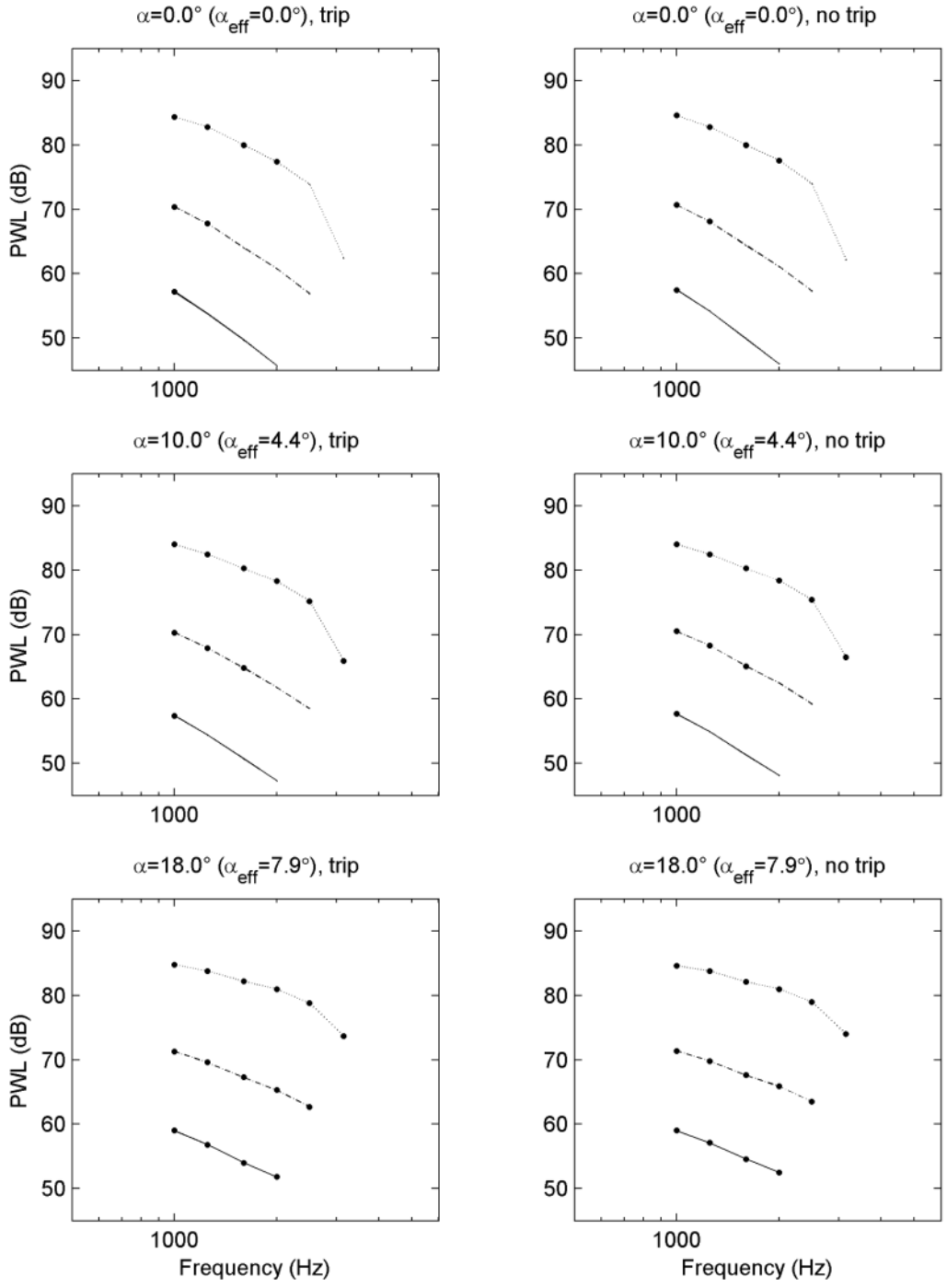


Figure 32. Leading-edge noise spectra for S834 airfoil (array on suction side)  $\underline{\quad}$  = 22.4 m/s;  $\underline{\quad}$  = 32.0 m/s;  $\dots$  = 47.9 m/s

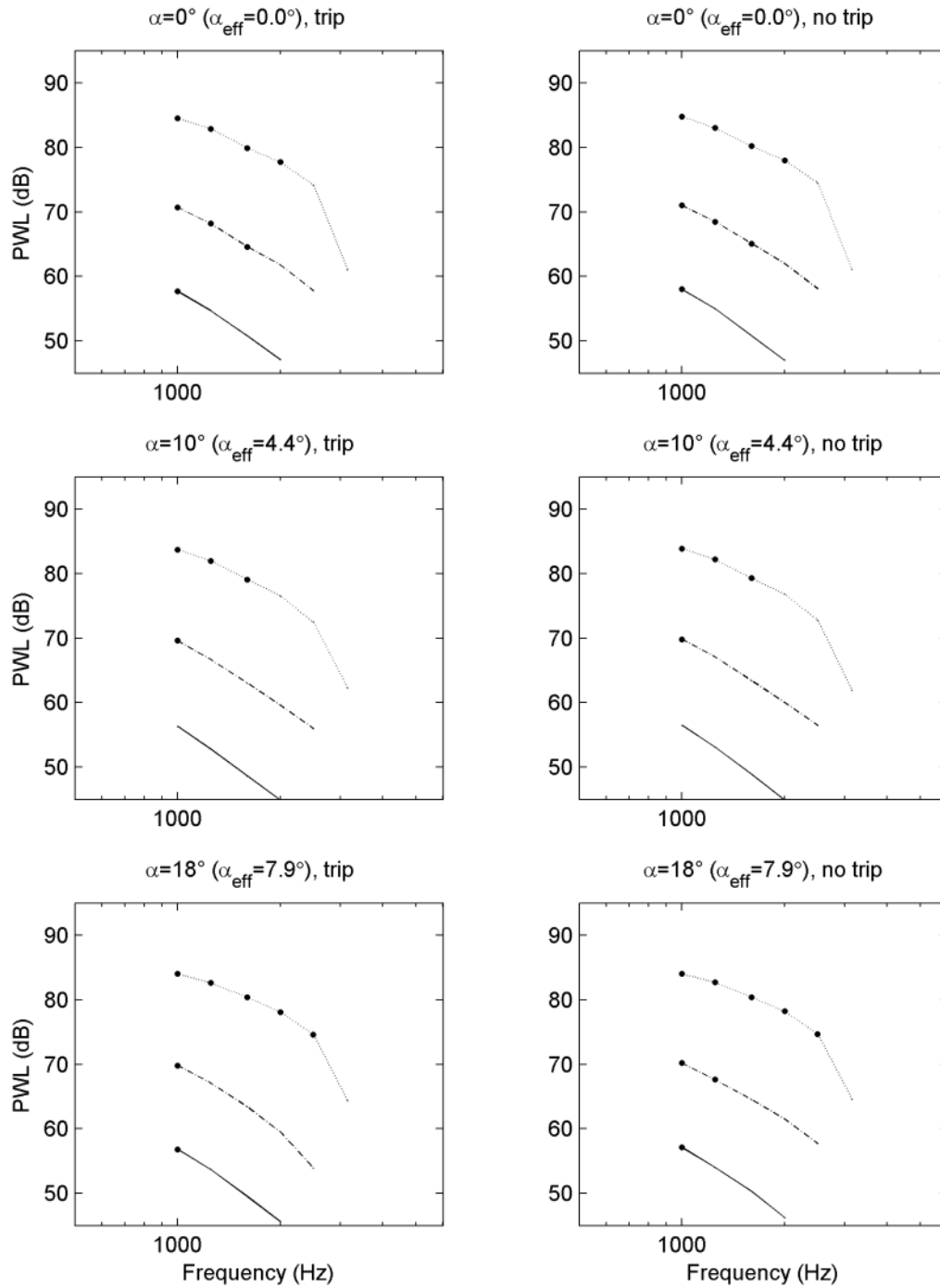


Figure 33. Leading-edge noise spectra for FX 63-137 airfoil (array on suction side)  $\text{---}$  = 22.4 m/s;  $\text{- -}$  = 32.0 m/s;  $\text{...}$  = 47.9 m/s

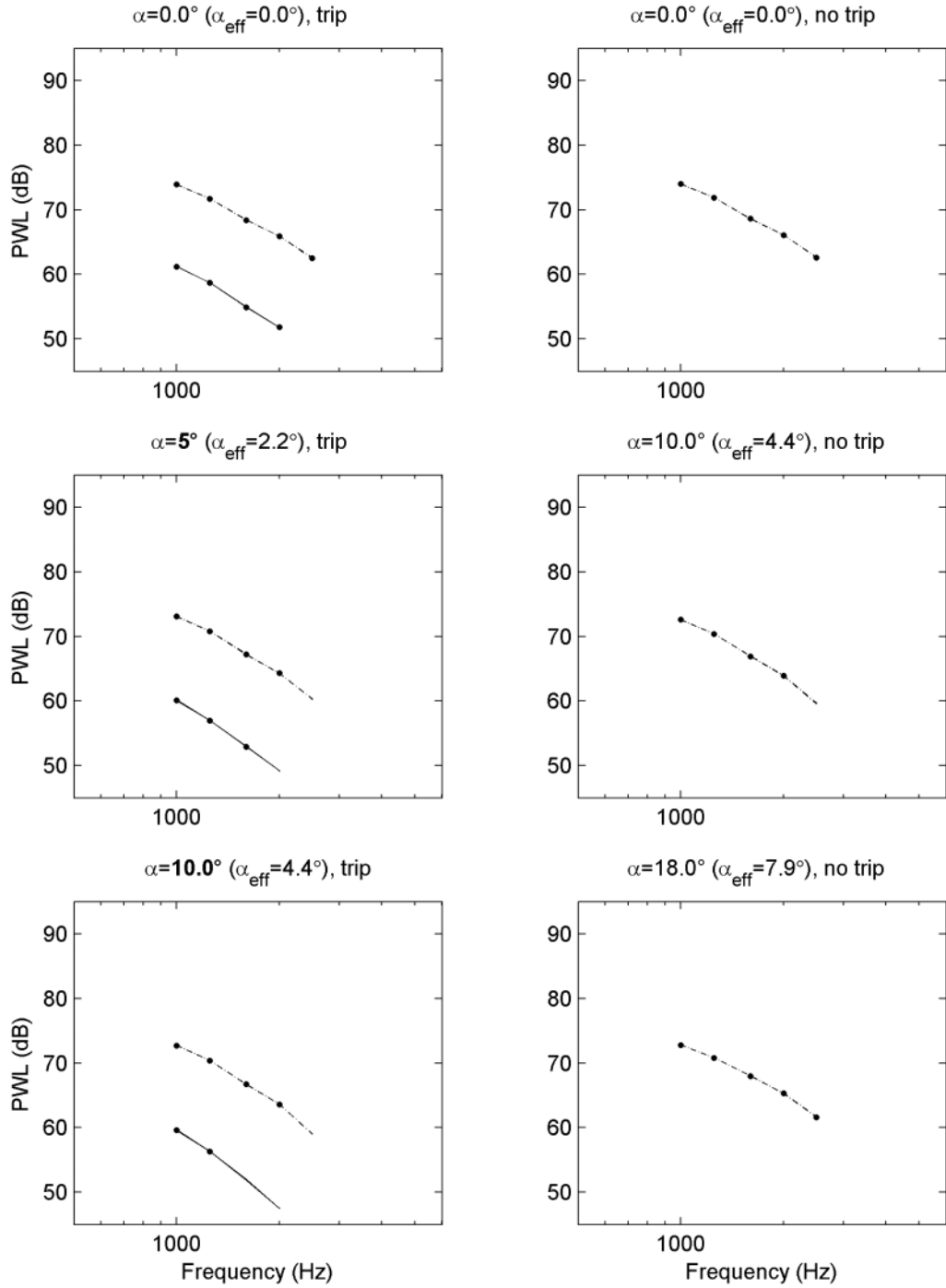


Figure 34. Leading-edge noise spectra for SG 6043 airfoil (array on suction side)  $\underline{\quad}$  = 22.4 m/s;  $\underline{\quad}$  = 32.0 m/s

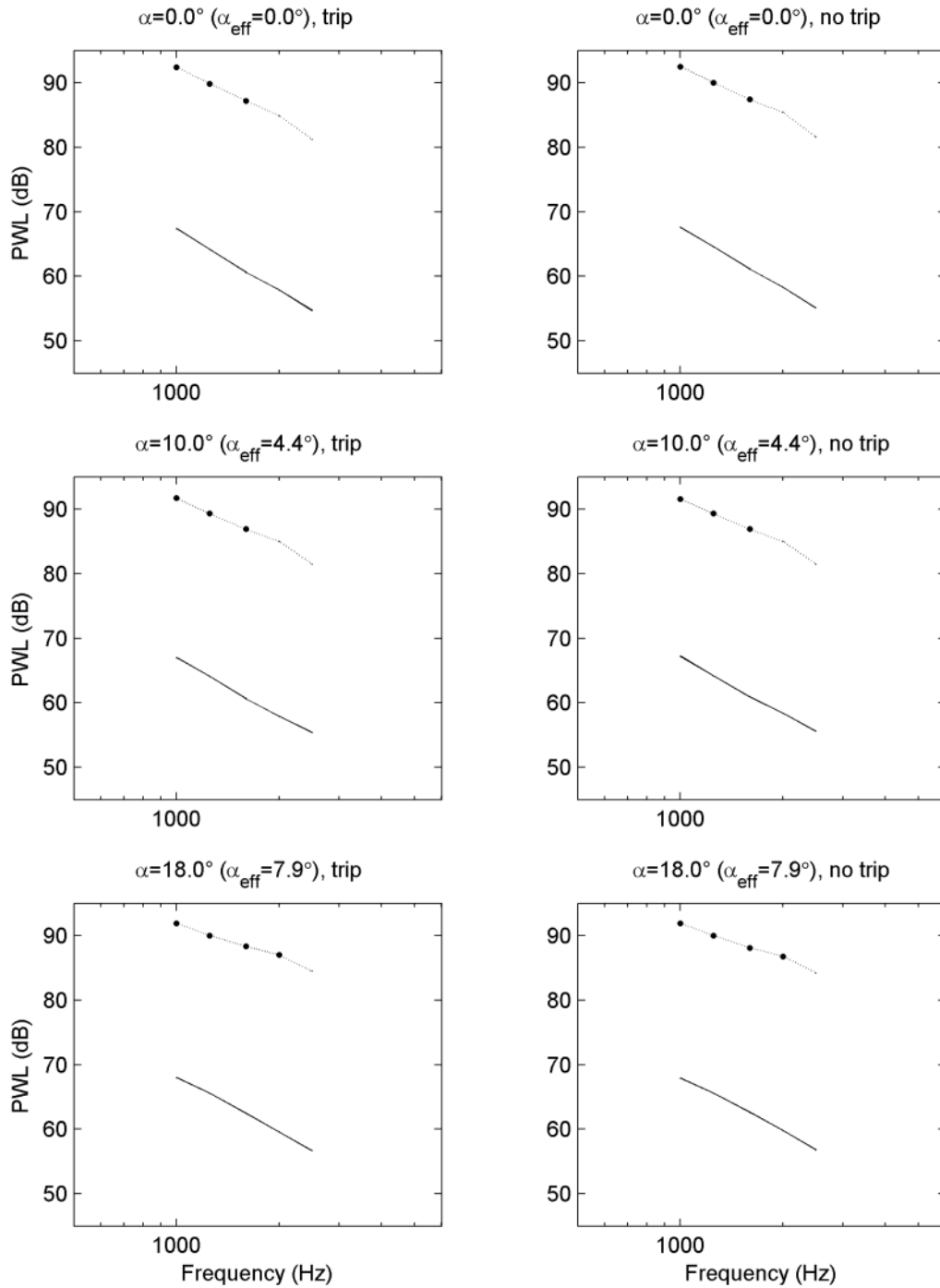


Figure 35. Leading-edge noise spectra for SH 3055 airfoil (array on suction side),      = 32.0 m/s; ... = 64.0 m/s

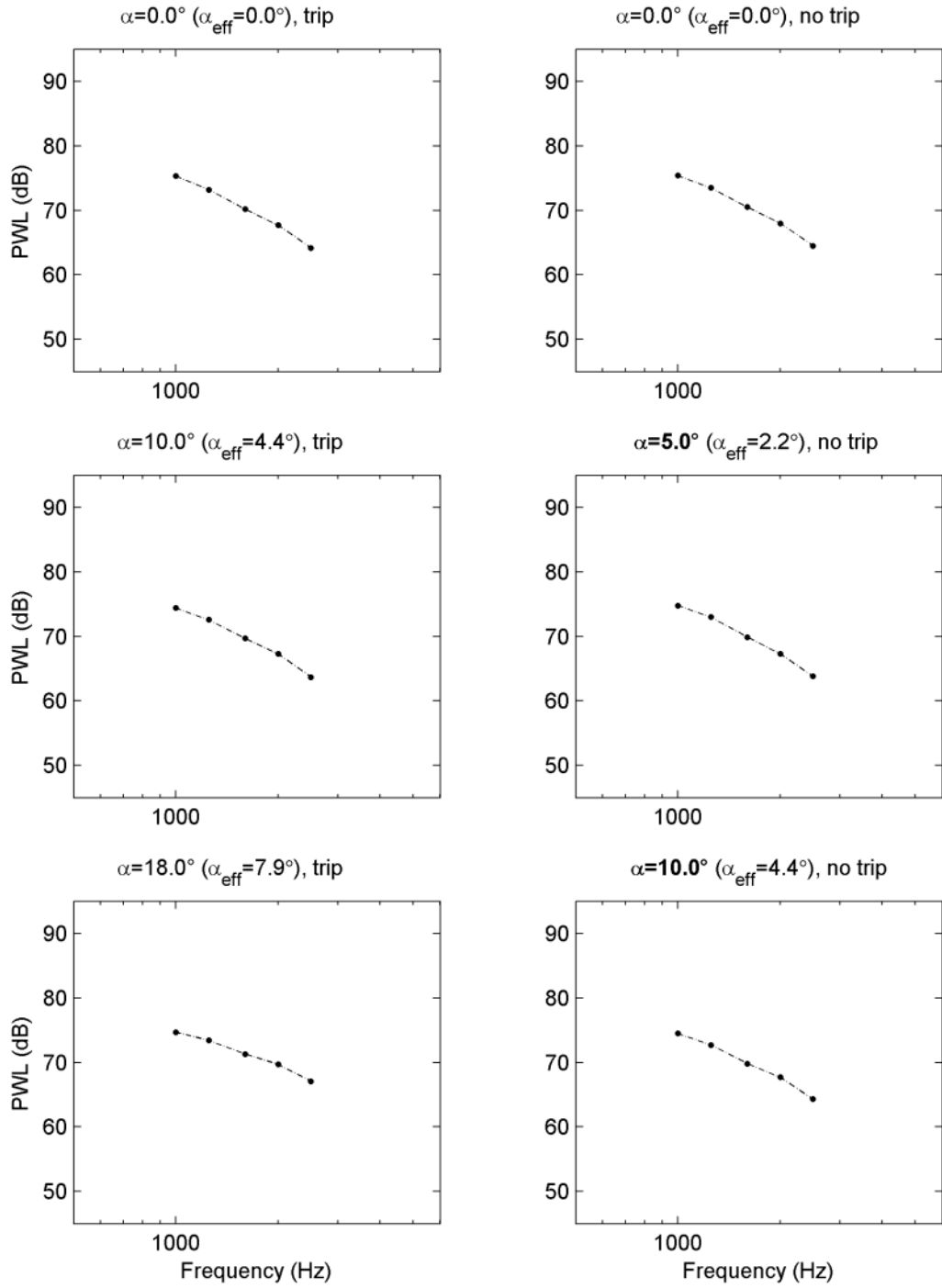


Figure 36. Leading-edge noise spectra for SD 2030 airfoil at 32 m/s (array on suction side)

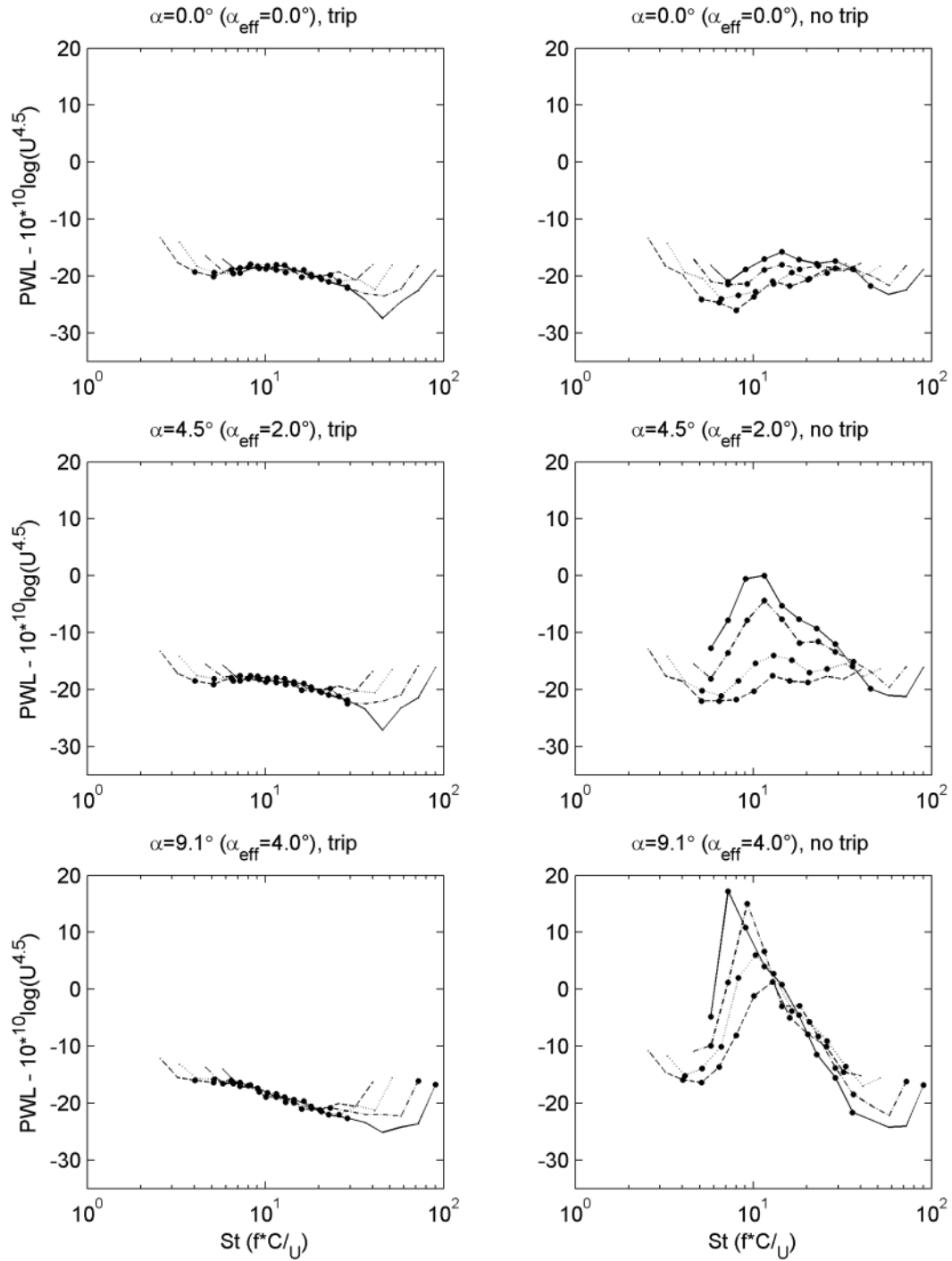


Figure 37 (part 1 of 2). Normalized trailing-edge noise spectra for NACA 0012 airfoil (array on suction side)  $—$  = 31.7 m/s;  $- -$  = 39.6 m/s;  $\dots$  = 55.5 m/s;  $- \cdot -$  = 71.3 m/s

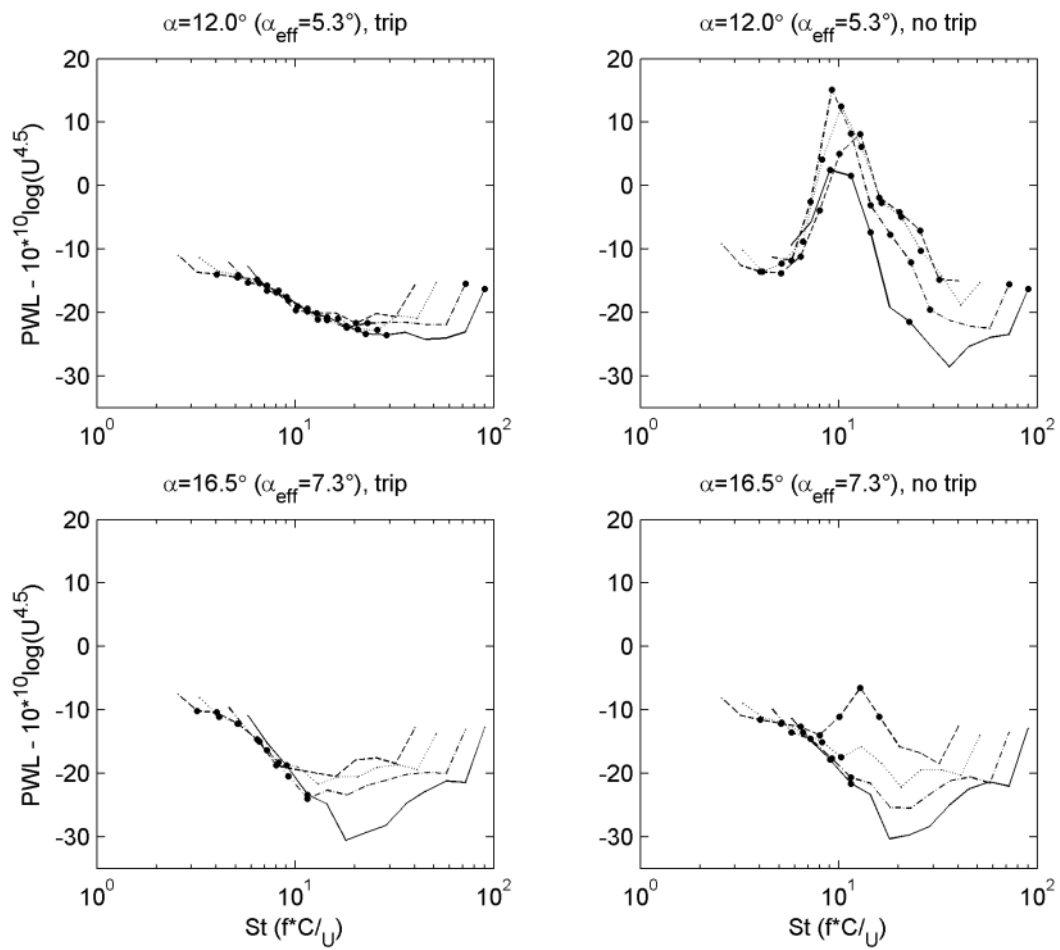


Figure 37 (part 2 of 2). Normalized trailing-edge noise spectra for NACA 0012 airfoil (array on suction side),  $\_ \_ = 31.7$  m/s;  $\_ \_ = 39.6$  m/s;  $\dots = 55.5$  m/s;  $\_ \_ = 71.3$  m/s

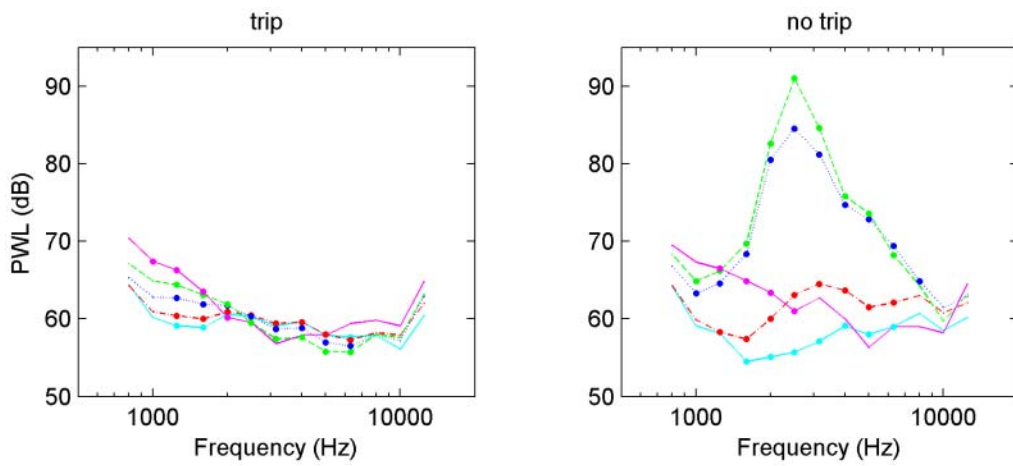


Figure 38. Trailing-edge noise spectra for NACA 0012 airfoil (array on suction side) at 55 m/s,  $\alpha = 0^\circ$ ;  $\alpha = 4.5^\circ$ ;  $\alpha = 9.1^\circ$ ;  $\alpha = 12^\circ$ ;  $\alpha = 16.5^\circ$

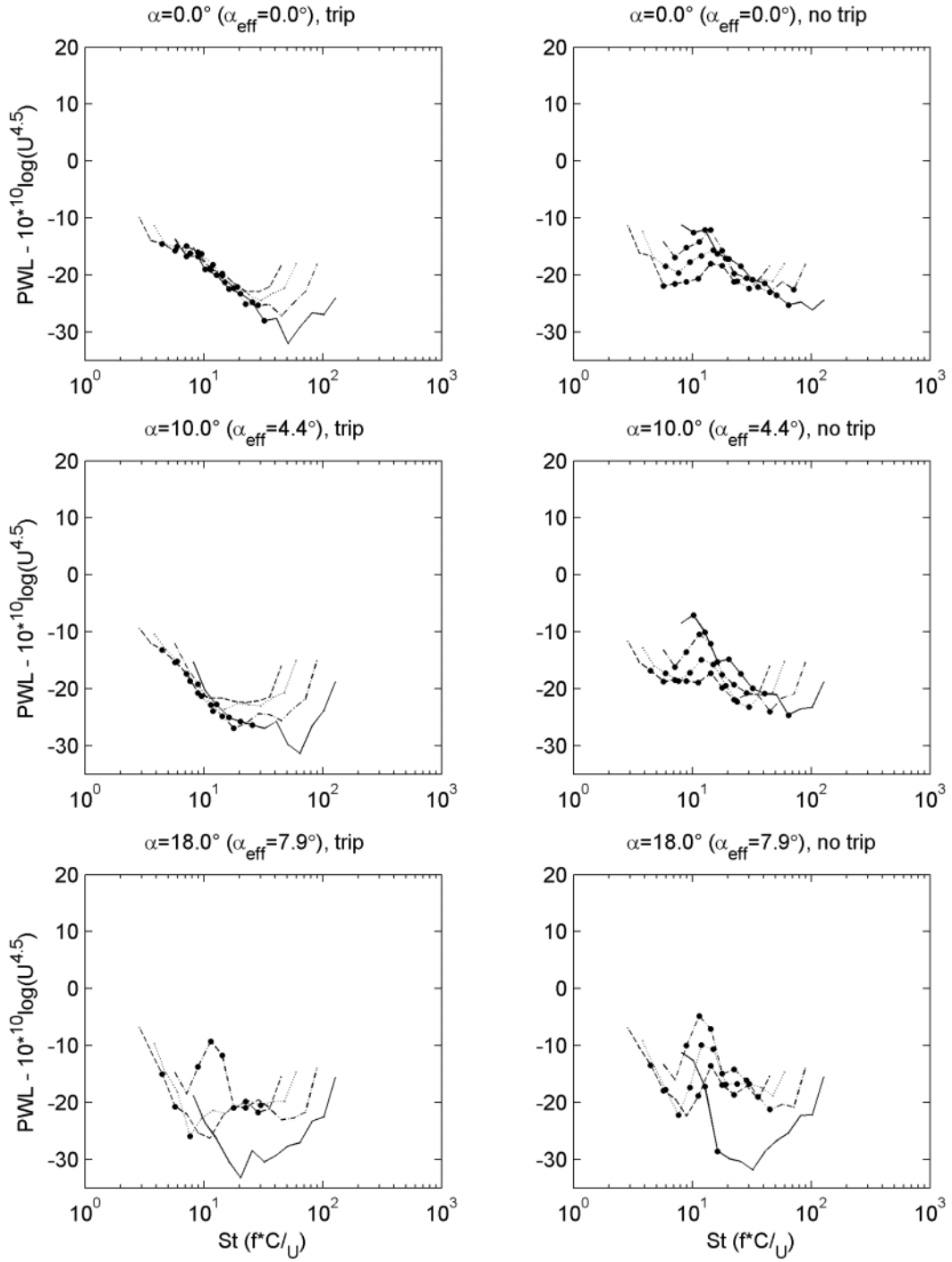


Figure 39. Normalized trailing-edge noise spectra for S822 airfoil (array on suction side),  $\text{—}$  = 22.4 m/s;  $\text{- -}$  = 32.0 m/s;  $\text{...}$  = 47.9 m/s;  $\text{- \cdot -}$  = 63.9 m/s

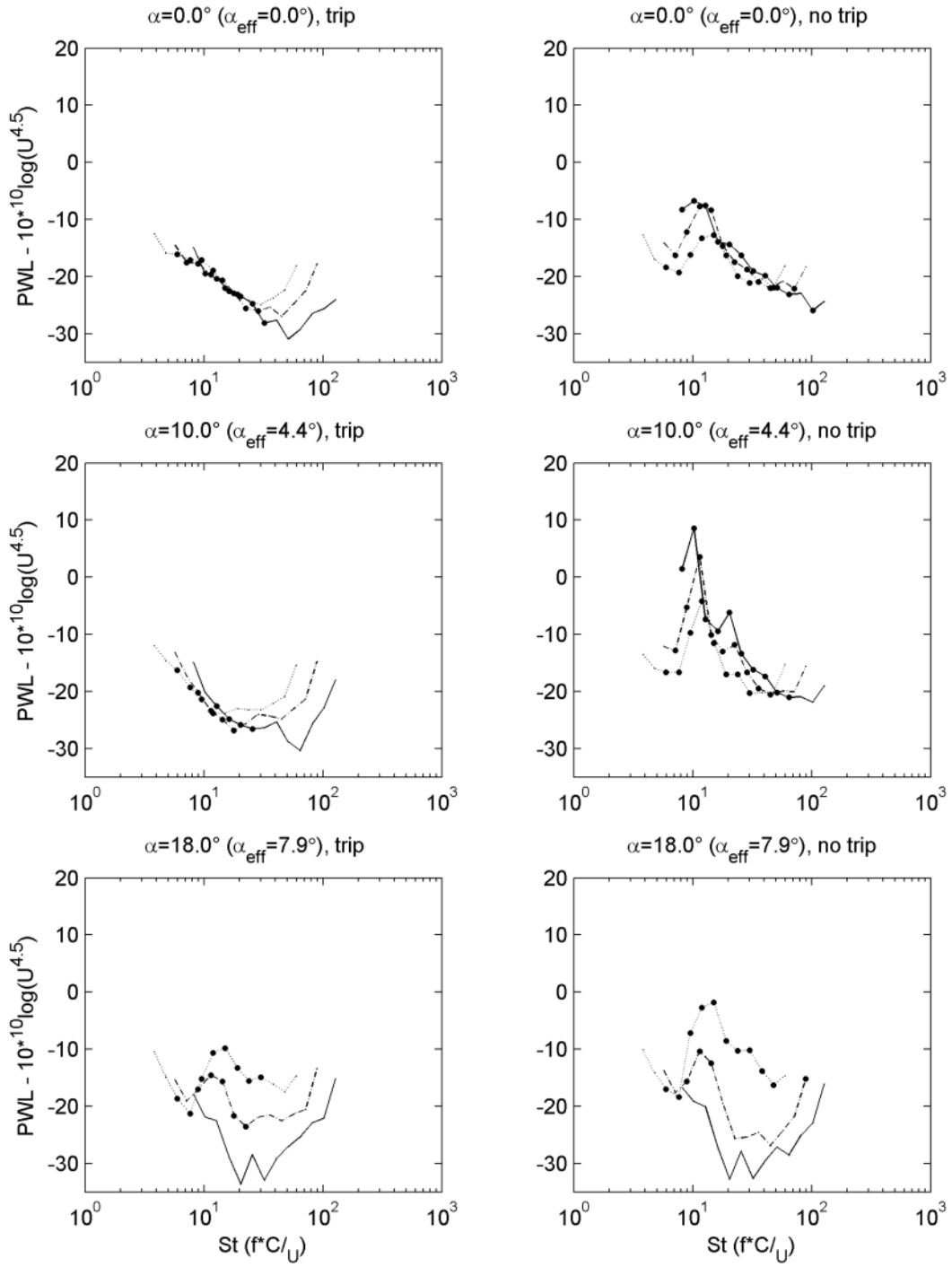


Figure 40. Normalized trailing-edge noise spectra for S834 airfoil (array on suction side),  $\underline{\quad}$  = 22.4 m/s;  $\underline{\quad}$  = 32.0 m/s;  $\dots$  = 47.9 m/s

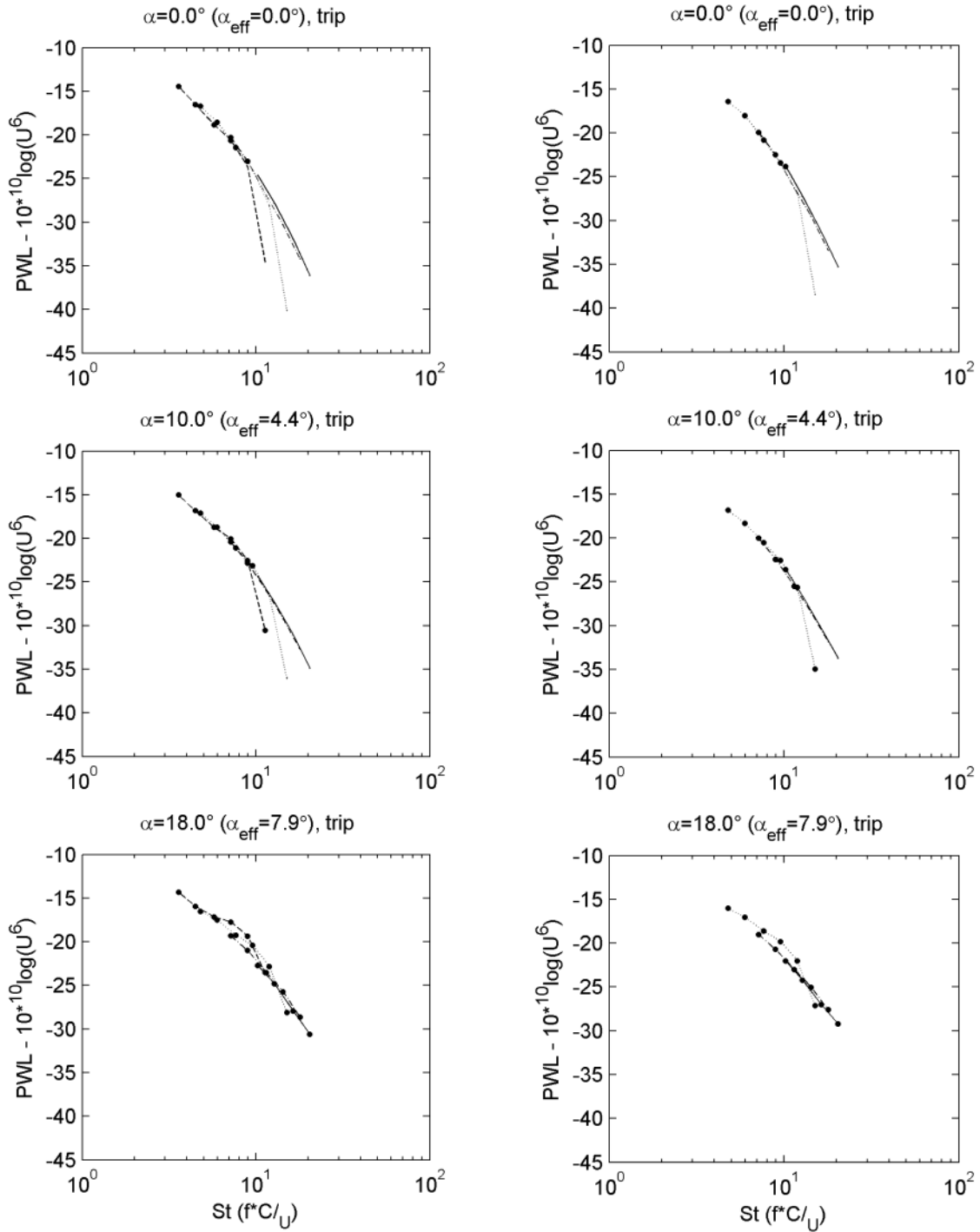
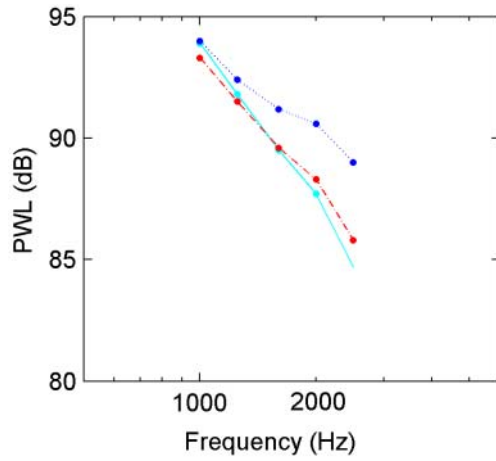
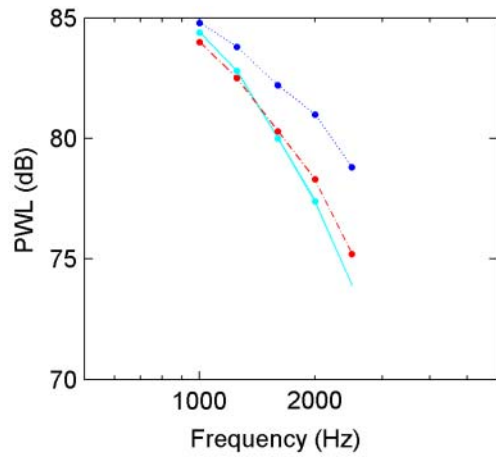


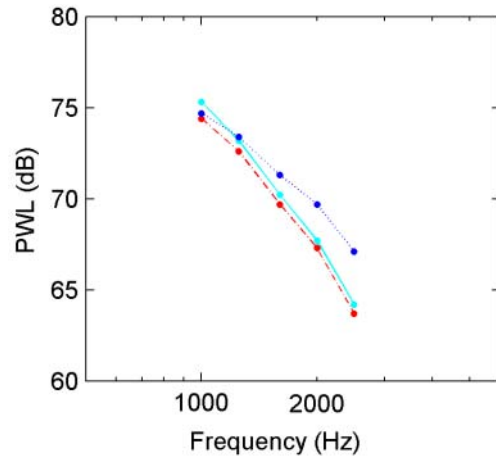
Figure 41. Normalized inflow turbulence noise spectra for tripped S822 (left column) and S834 (right column) airfoil (array on suction side),  $\underline{\quad}$  = 22.4 m/s;  $\underline{\quad}$  = 32.0 m/s;  $\dots$  = 47.9 m/s;  $\underline{\quad}$  = 63.9 m/s



(a)



(b)



(c)

Figure 42. Inflow turbulence noise spectra for tripped S822 (a), S834 (b), and SD 2030 (c) airfoils at 64, 48, and 32 m/s respectively (array on suction side), —  $\alpha = 0^\circ$ ; - -  $\alpha = 10^\circ$ ; ...  $\alpha = 18^\circ$

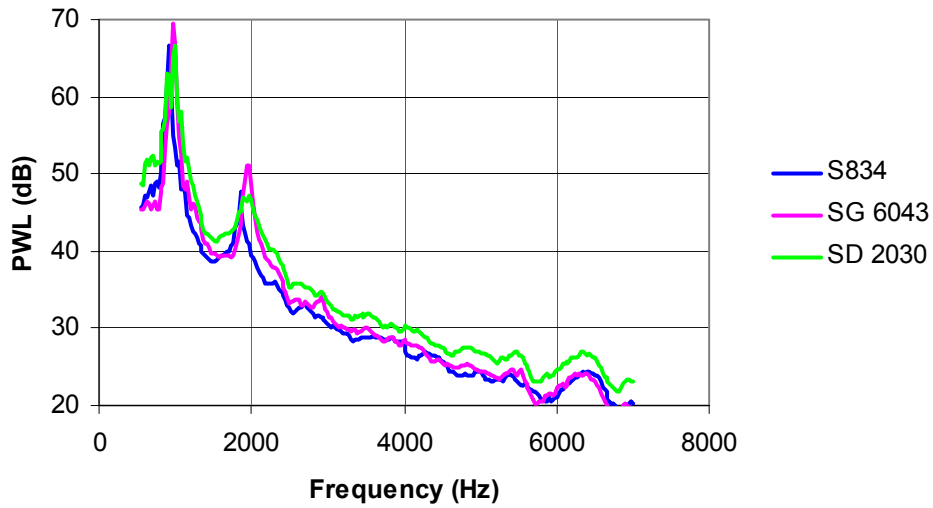


Figure 43. Narrowband trailing-edge noise spectra for three untripped airfoils that showed intense tones ( $U = 22.4$  m/s;  $\alpha = 10^\circ$  for S834,  $\alpha = 0^\circ$  for SG 6043 and SD 2030)

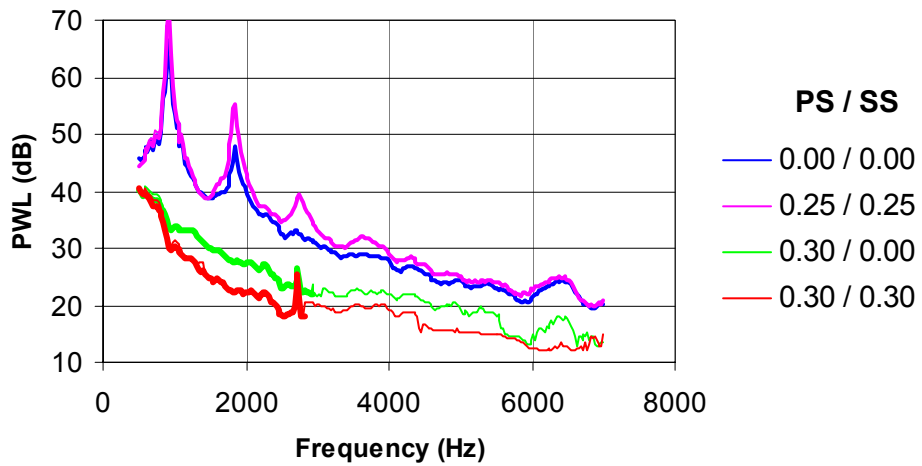


Figure 44. Narrowband trailing-edge noise spectra for S834 airfoil at 22.4 m/s and  $\alpha = 10^\circ$ , as a function of trip thickness on pressure side (PS) and suction side (SS). A thin line indicates that these spectral values are an upper limit for the trailing-edge noise level.

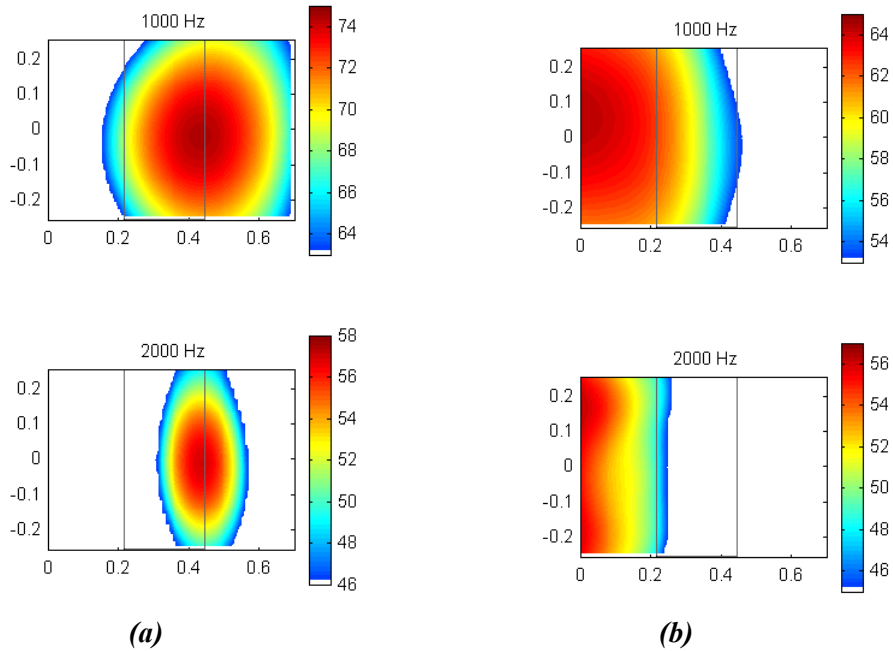


Figure 45. Acoustic source plots for untripped S834 airfoil at 22.4 m/s and  $\alpha = 10^\circ$ , without (a) and with (b) turbulence grid (array on suction side). Note the difference in color scales.

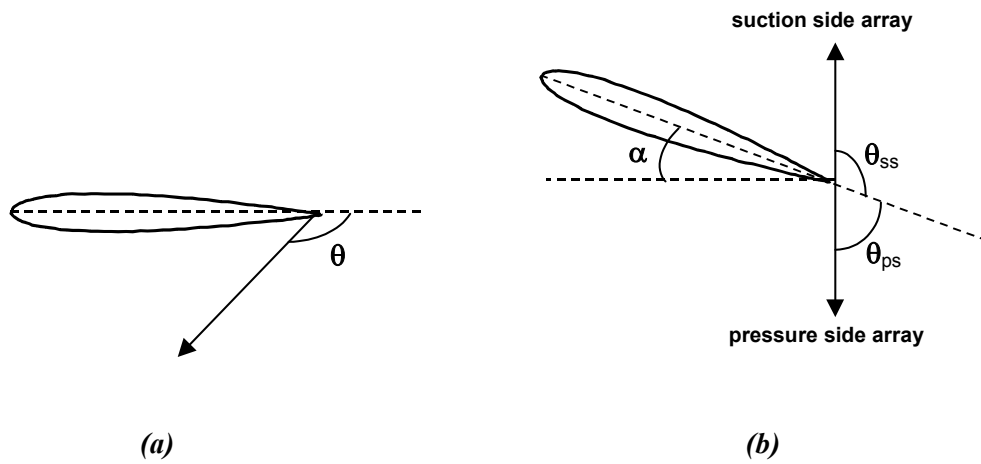


Figure 46. (a) Definition of emission angle  $\theta$  (b) Illustration of difference in measured direction for pressure and suction side array, as a function of angle of attack

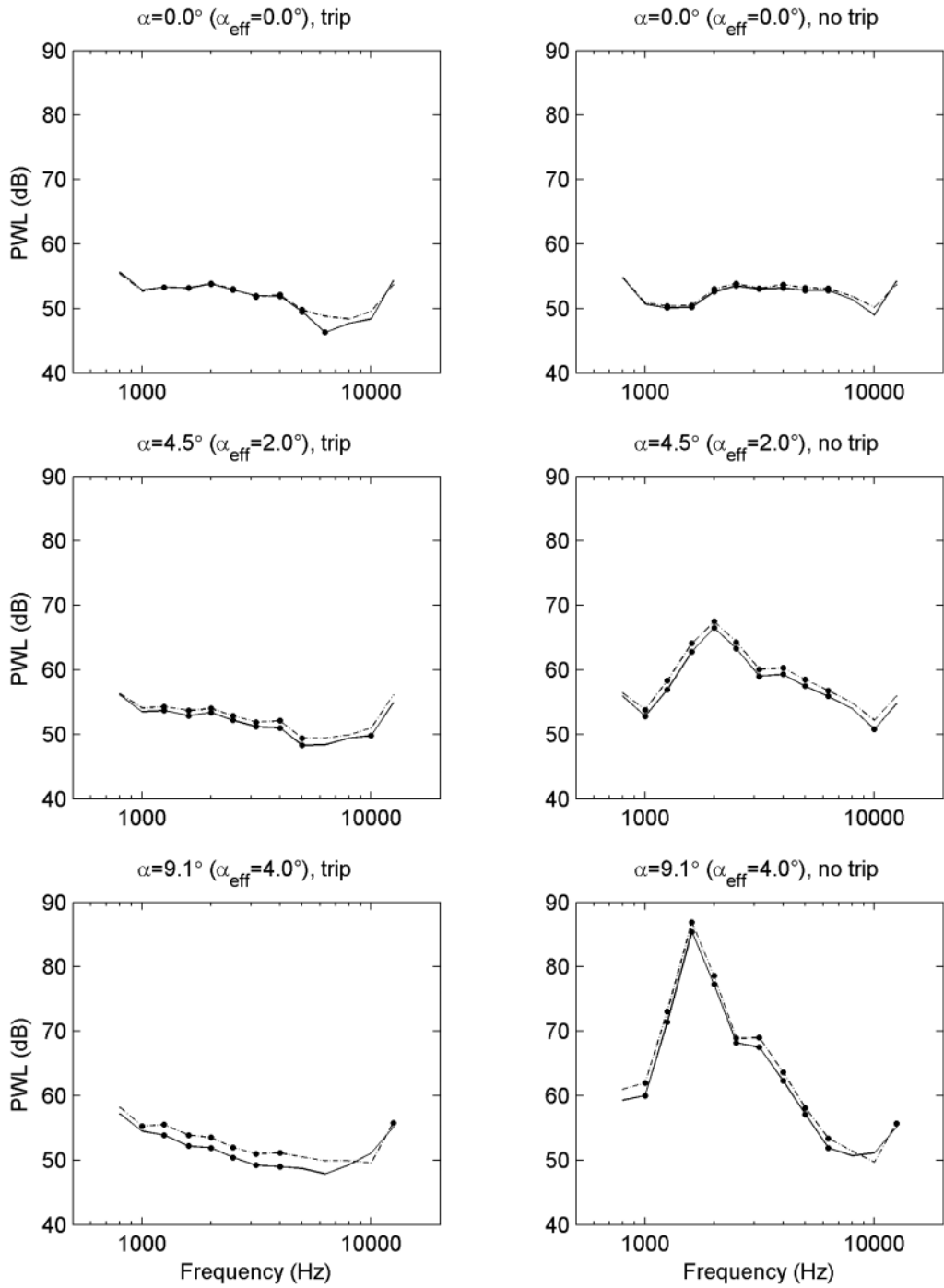


Figure 47 (part 1 of 2). Trailing-edge noise spectra for NACA 0012 airfoil at 39.6 m/s, \_\_\_ = array on pressure side; \_.\_ = array on suction side

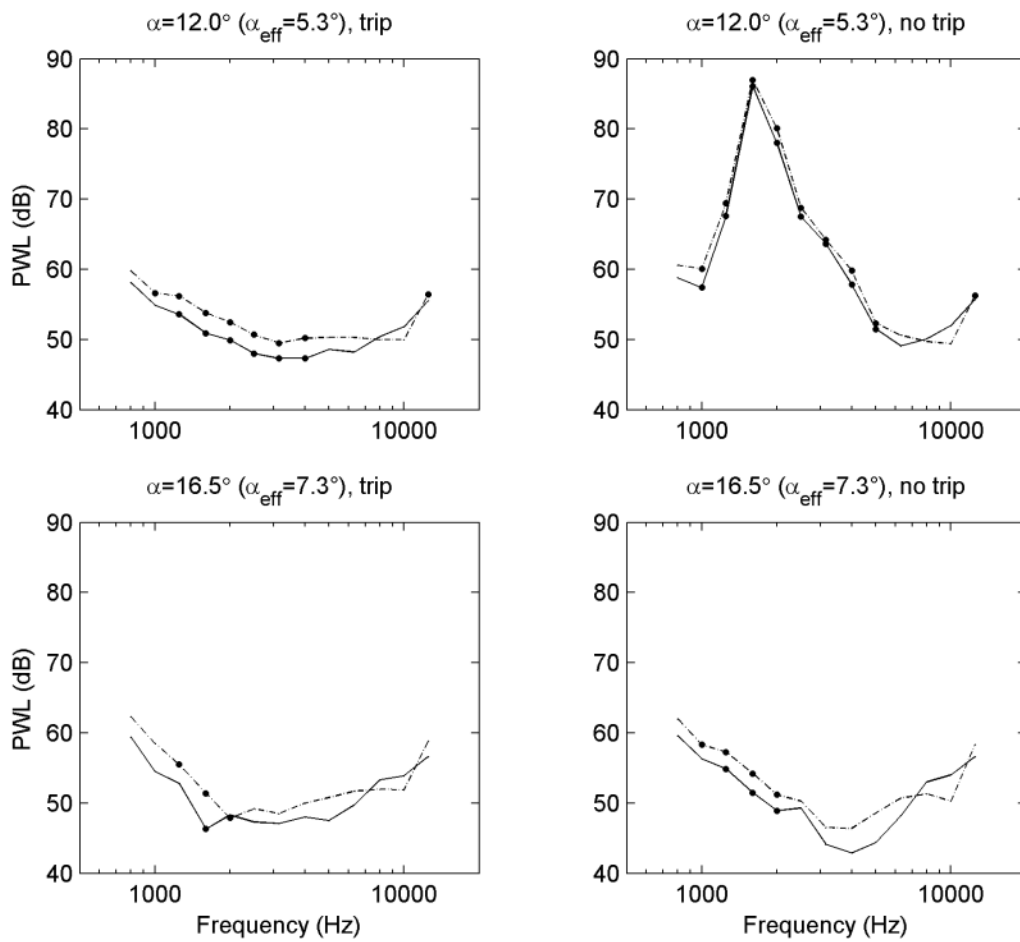


Figure 47. (Part 2 of 2). Trailing-edge noise spectra for NACA 0012 airfoil at 39.6 m/s,  $\text{---}$  = array on pressure side;  $\text{- - -}$  = array on suction side

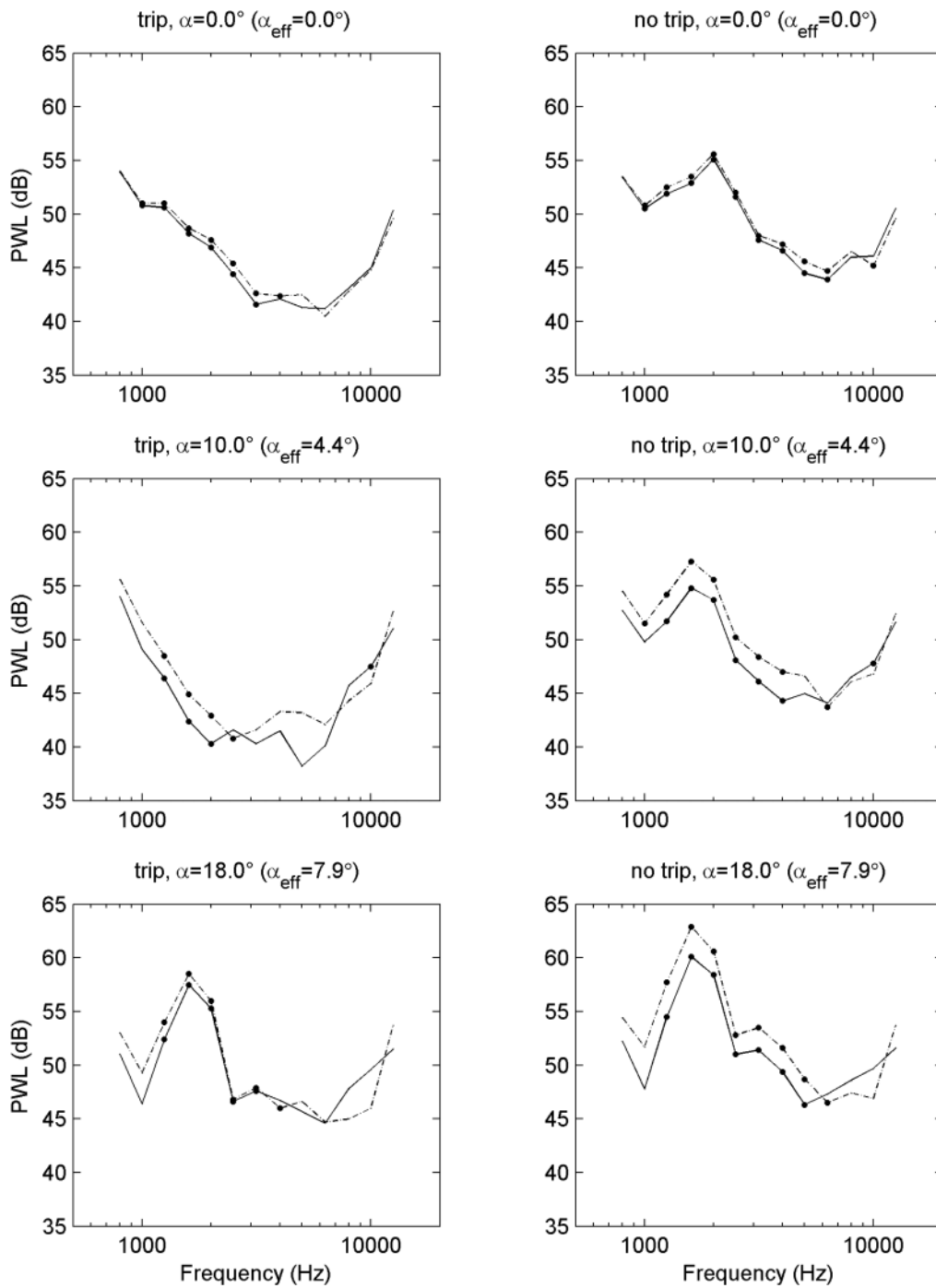


Figure 48. Trailing-edge noise spectra for S822 airfoil at 32 m/s, \_\_\_ = array on pressure side; \_.\_ = array on suction side

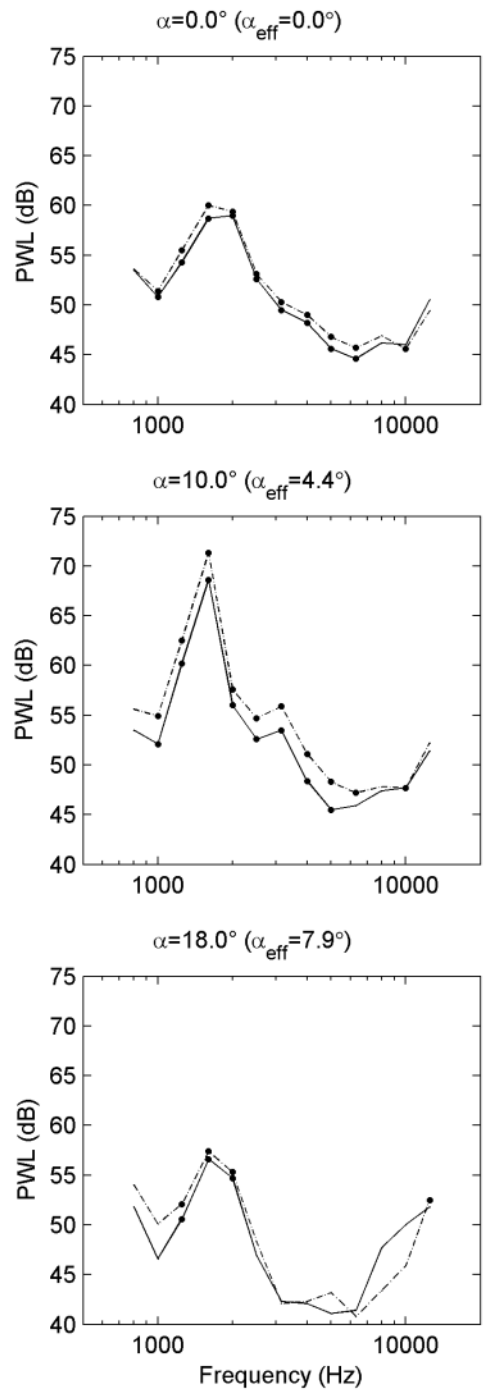


Figure 49. Trailing-edge noise spectra for untripped S834 airfoil at 32 m/s, \_\_\_ = array on pressure side; \_ \_ = array on suction side

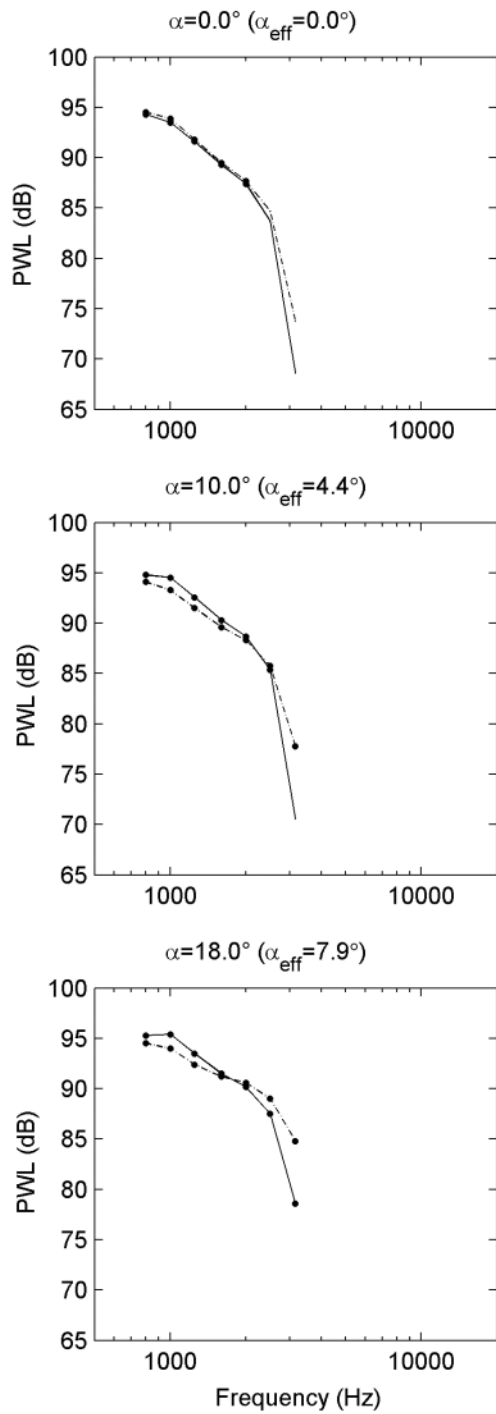


Figure 50. Inflow turbulence noise spectra for tripped S822 airfoil at 64 m/s, \_\_\_ = array on pressure side; \_.\_ = array on suction side

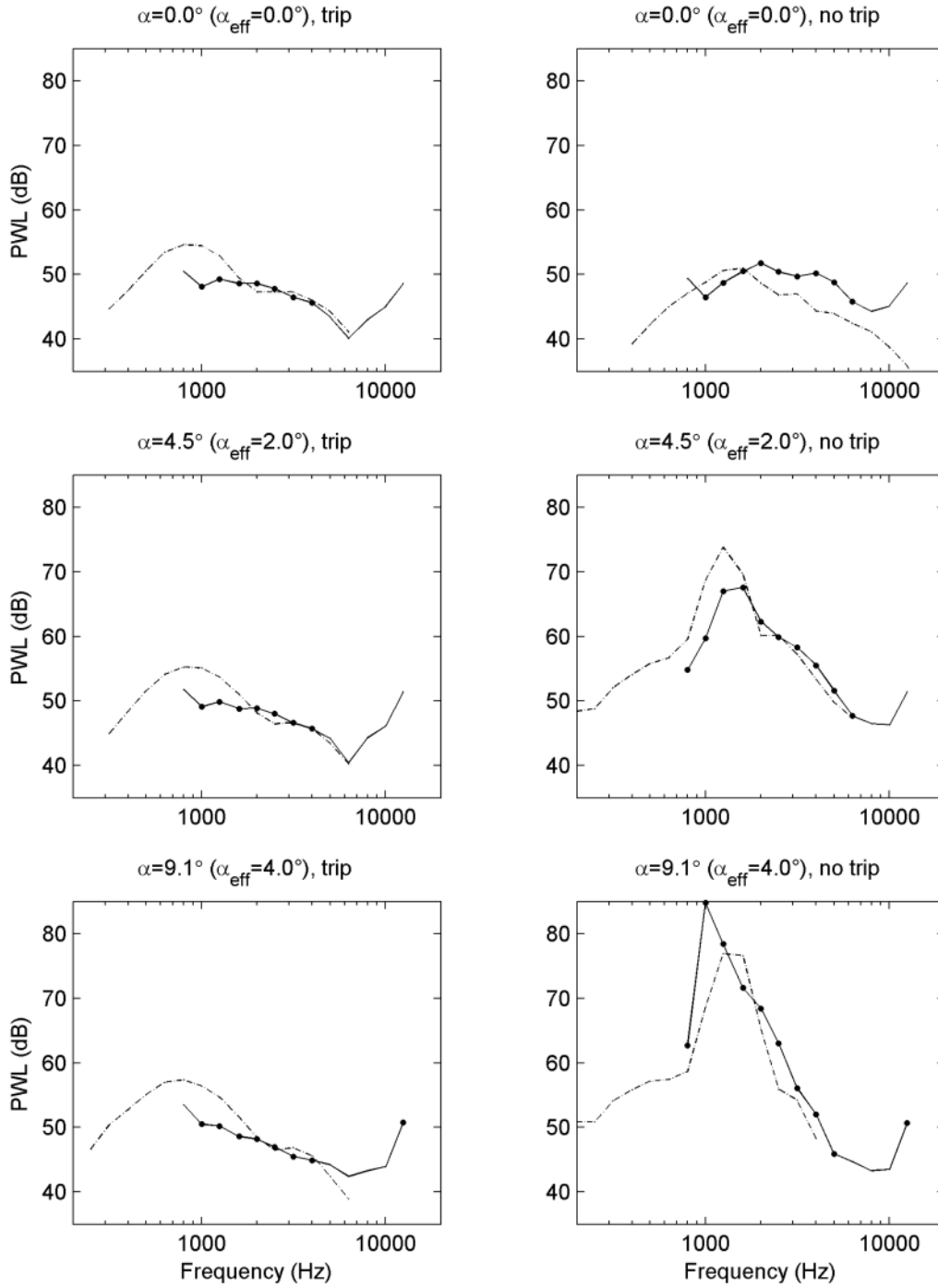


Figure 51 (part 1 of 2). Trailing-edge noise spectra for NACA 0012 airfoil at 31.7 m/s \_\_\_ = NLR data (array on suction side); \_ \_ = NASA data [2]

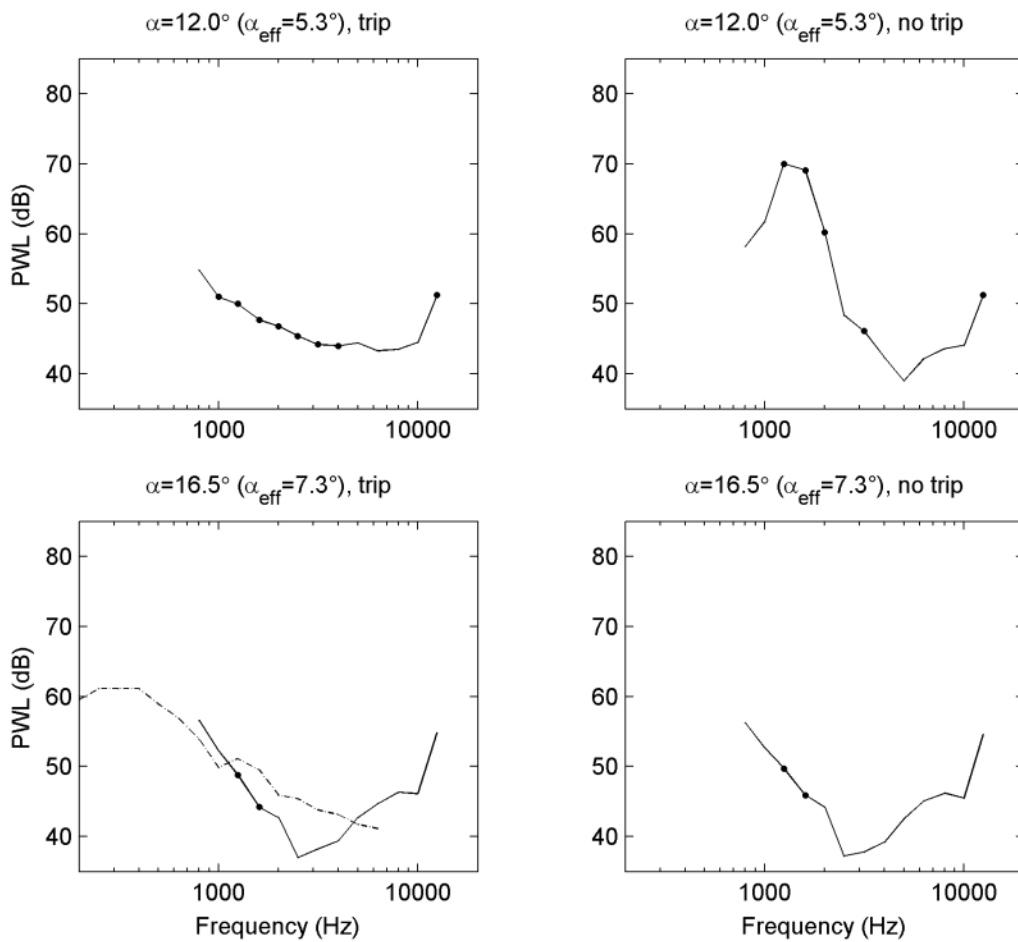


Figure 51 (part 2 of 2). Trailing-edge noise spectra for NACA 0012 airfoil at 31.7 m/s, \_\_\_ = NLR data (array on suction side); -.- = NASA data [2]

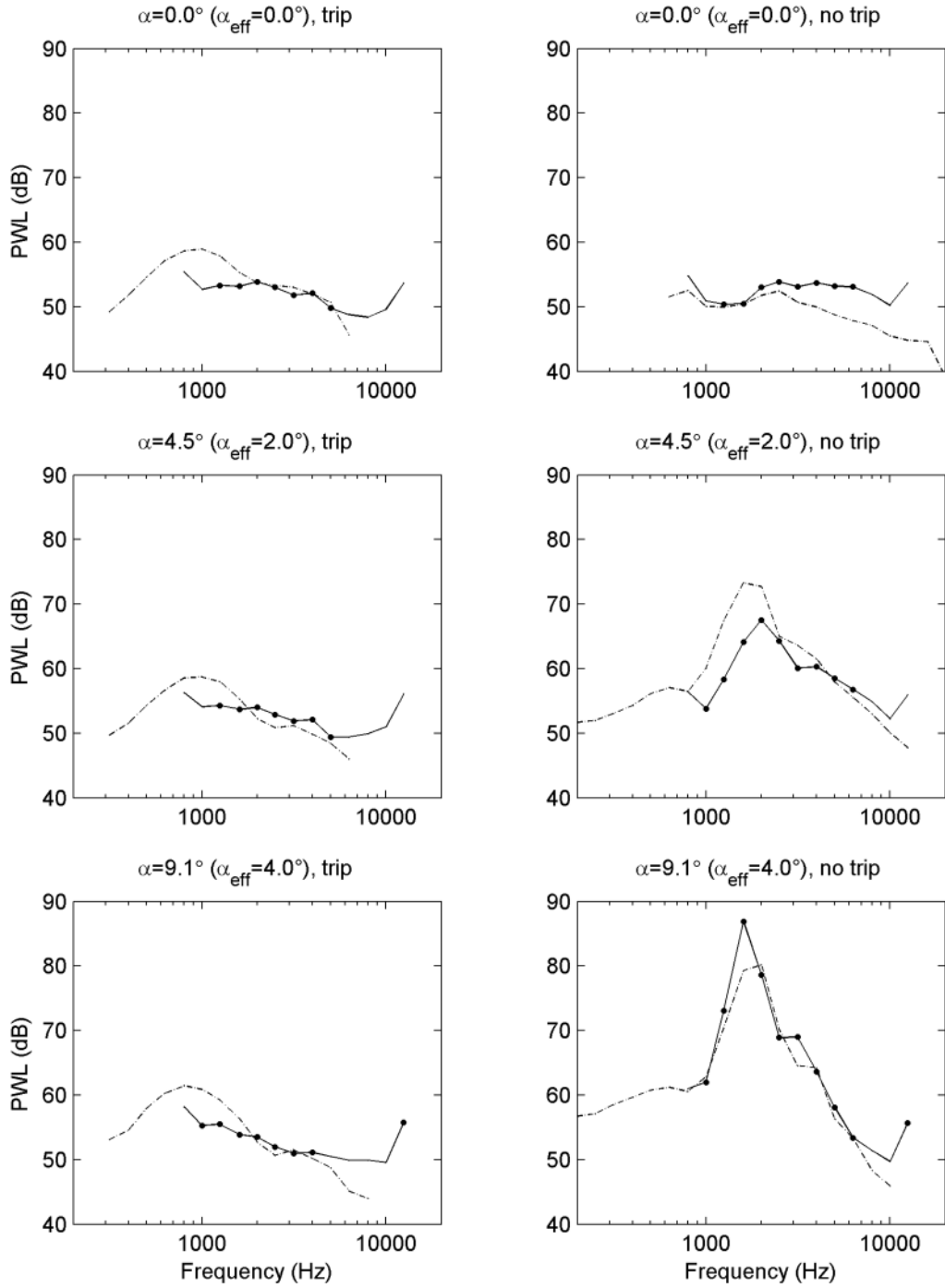


Figure 52 (part 1 of 2). Trailing-edge noise spectra for NACA 0012 airfoil at 39.6 m/s, \_\_\_ = NLR data (array on suction side); \_ \_ = NASA data [2]

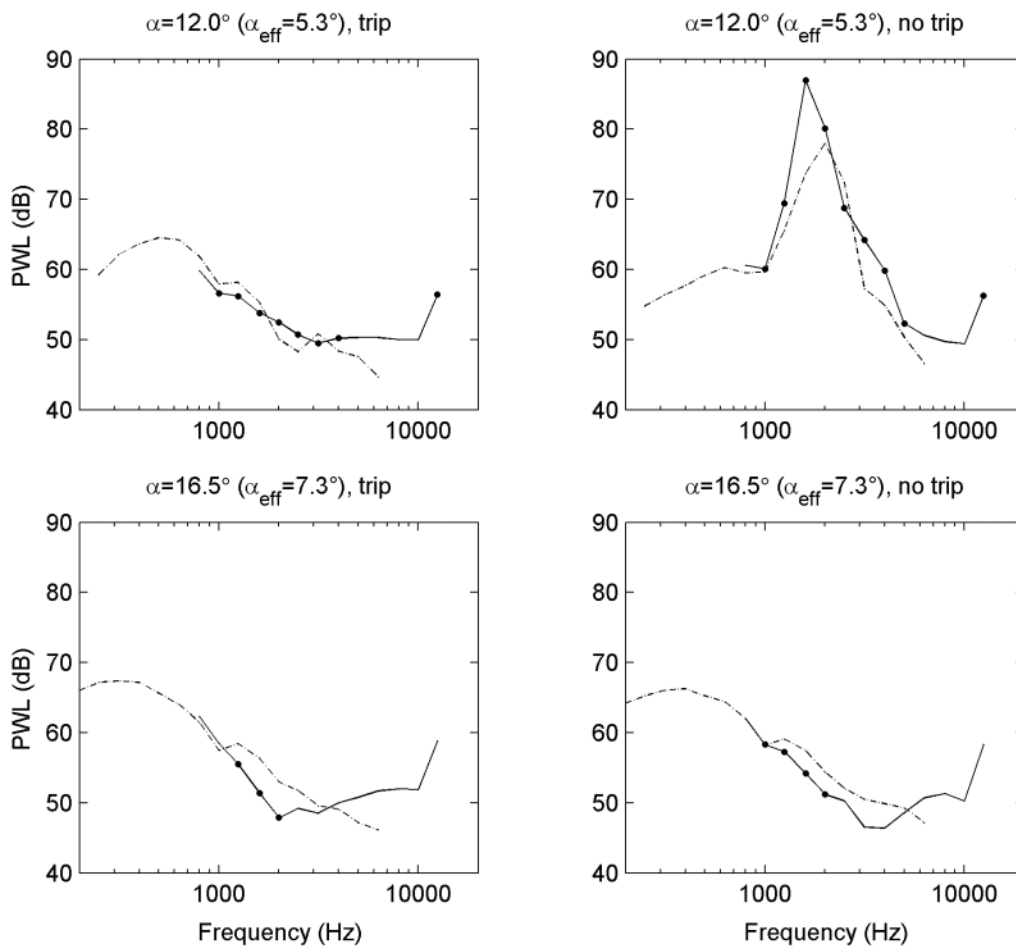


Figure 52 (part 2 of 2). Trailing-edge noise spectra for NACA 0012 airfoil at 39.6 m/s, \_\_\_ = NLR data (array on suction side); \_.\_ = NASA data [2]

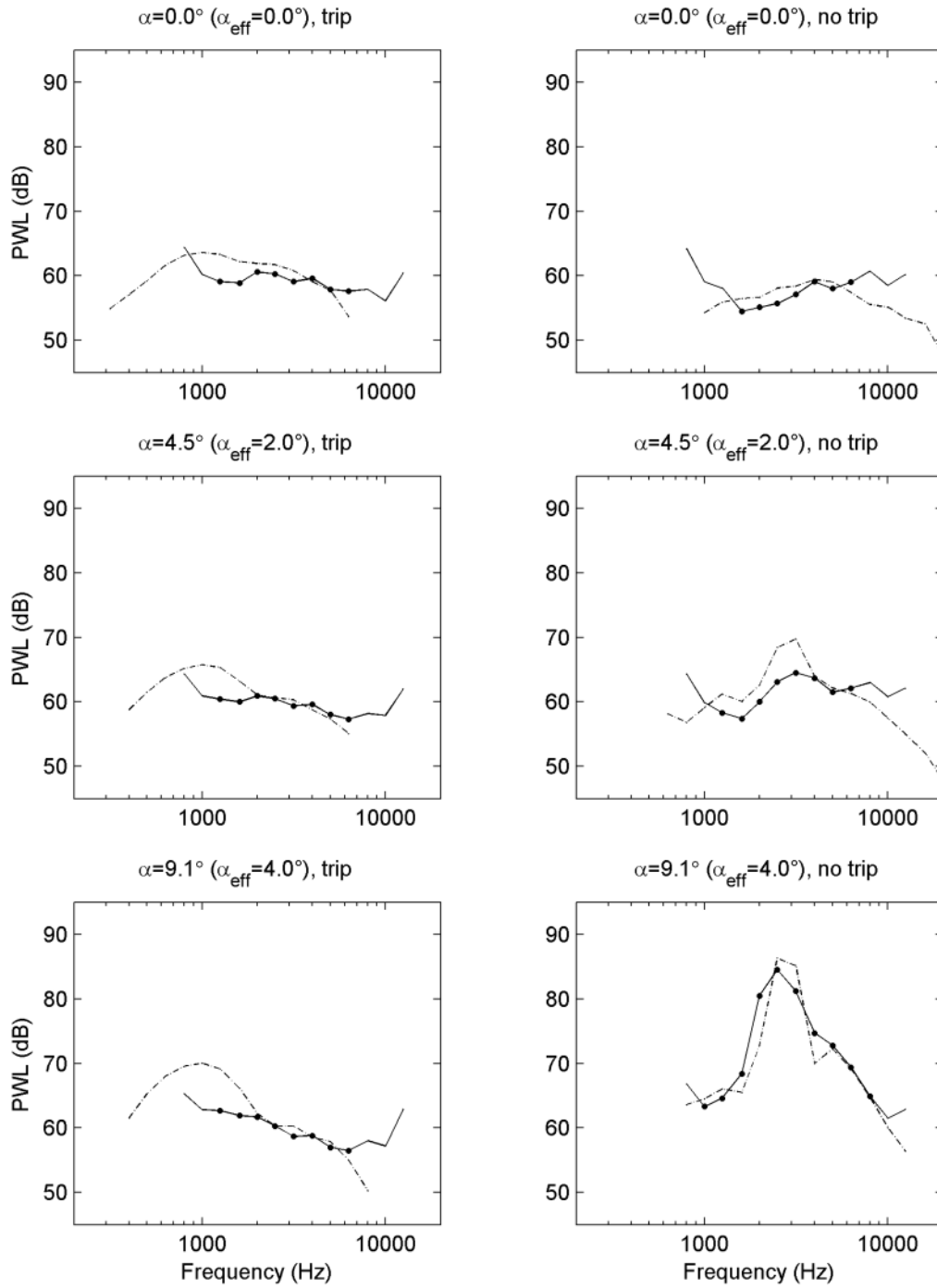


Figure 53 (part 1 of 2). Trailing-edge noise spectra for NACA 0012 airfoil at 55.5 m/s, \_\_\_ = NLR data (array on suction side); \_ \_ = NASA data [2]

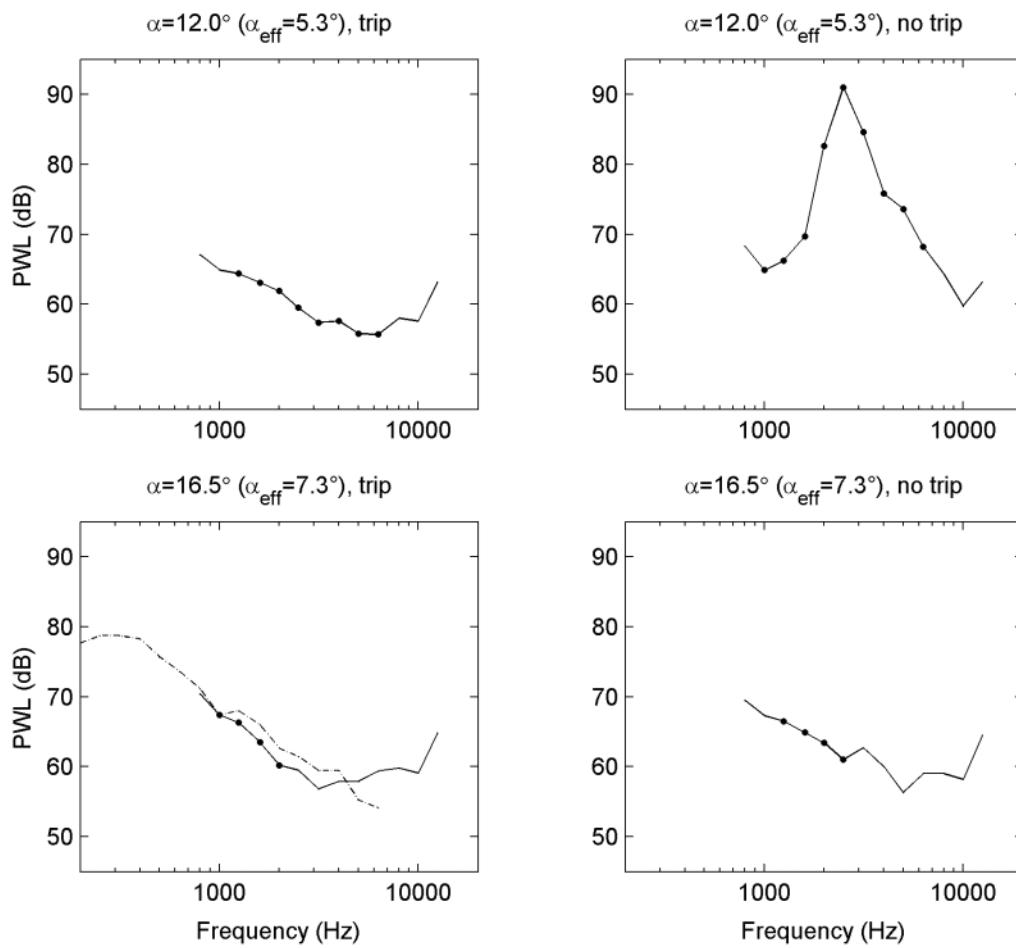


Figure 53 (part 2 of 2). Trailing-edge noise spectra for NACA 0012 airfoil at 55.5 m/s, \_\_ = NLR data (array on suction side); \_ \_ = NASA data [2]

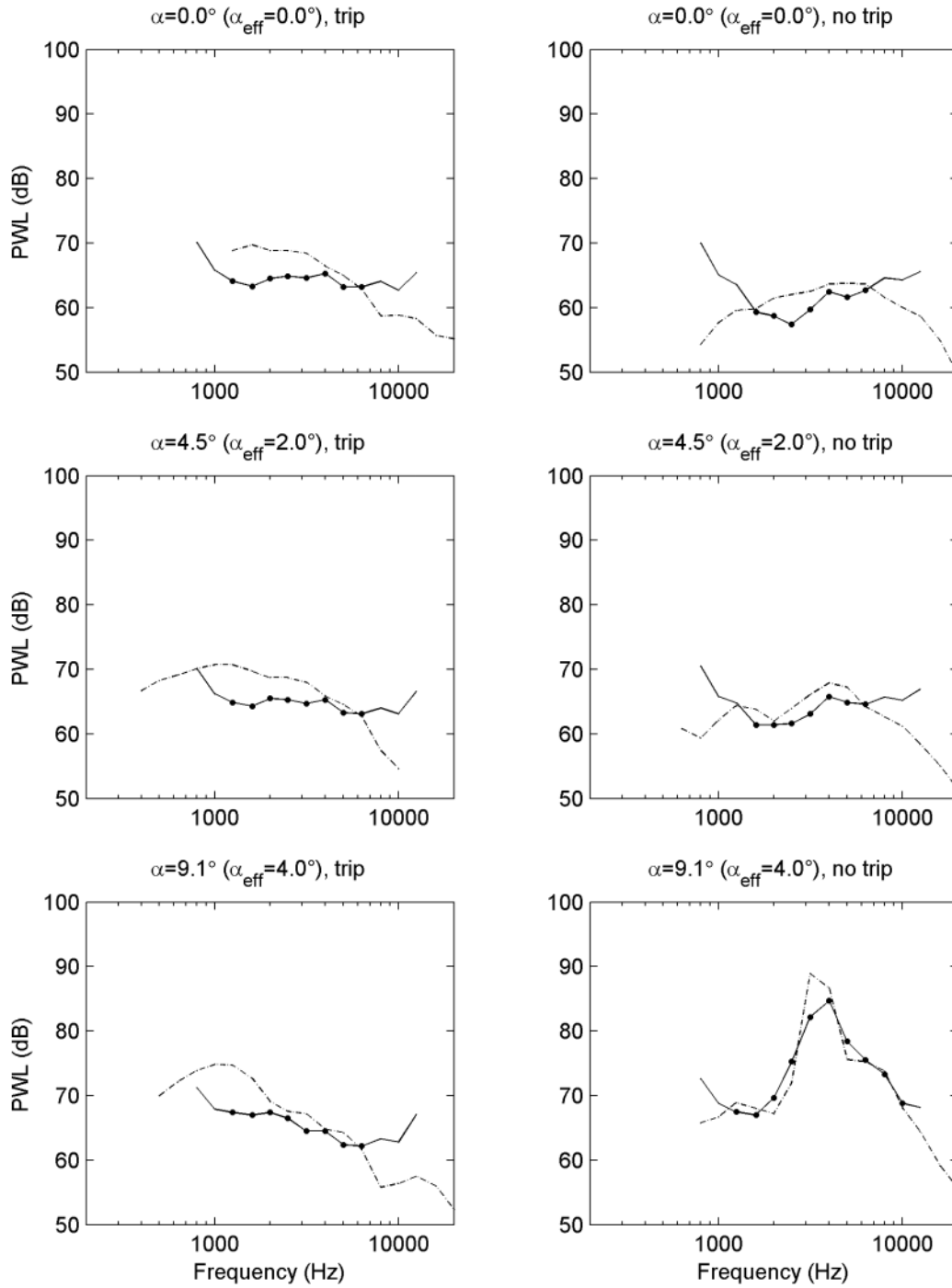


Figure 54 (part 1 of 2). Trailing-edge noise spectra for NACA 0012 airfoil at 71.3 m/s, \_\_\_ = NLR data (array on suction side); \_ \_ = NASA data [2]

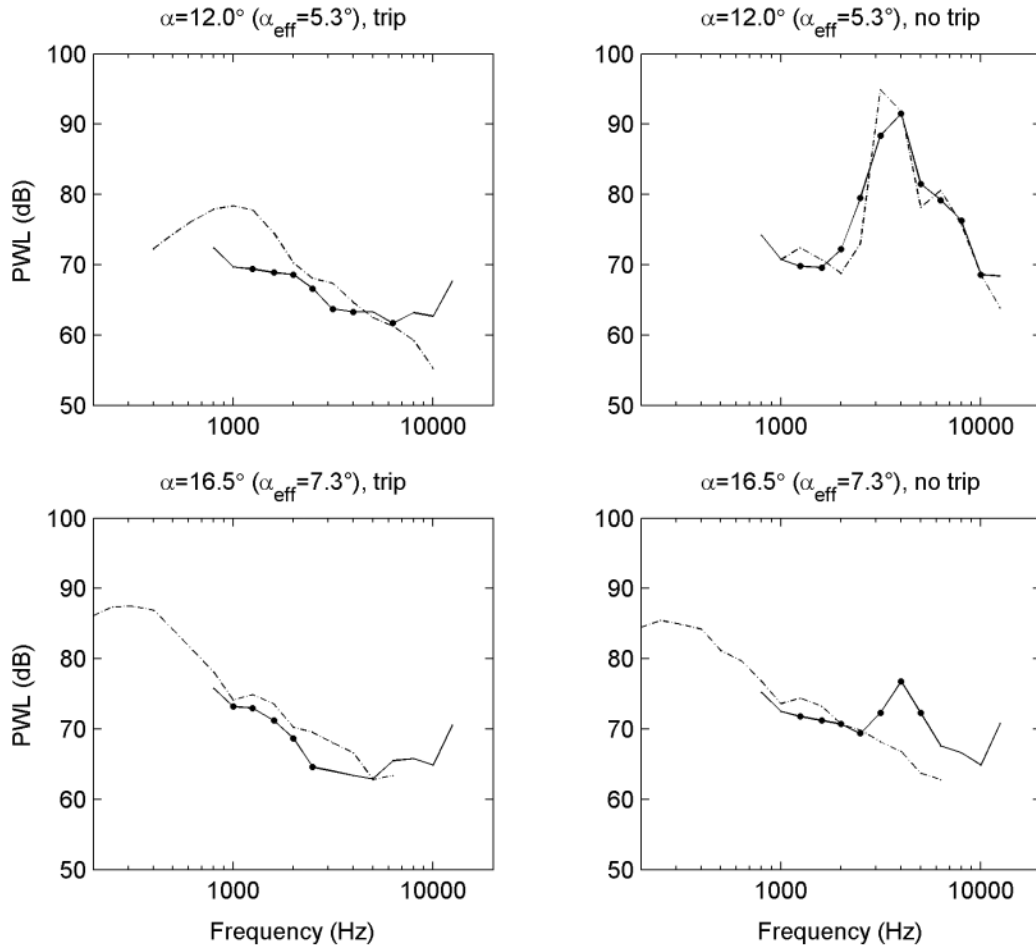


Figure 54 (part 2 of 2). Trailing-edge noise spectra for NACA 0012 airfoil at 71.3 m/s, \_\_\_ = NLR data (array on suction side); \_ \_ = NASA data [2]

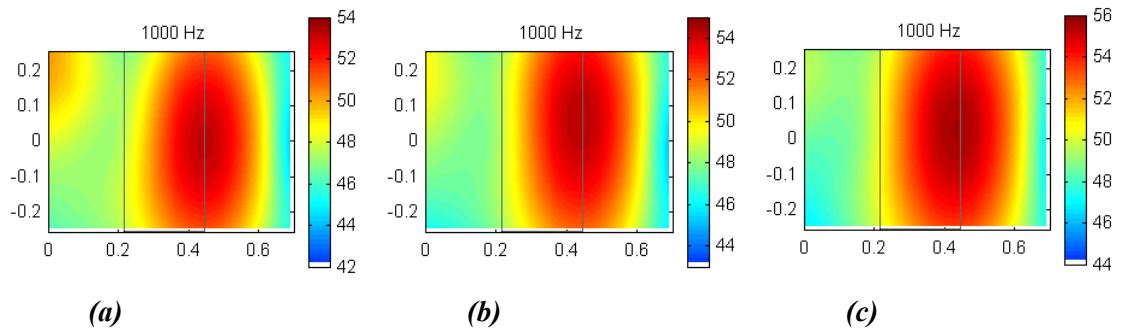


Figure 55. Acoustic source plots for tripped NACA 0012 airfoil at 31.7 m/s and  $\alpha = 0^\circ$  (a),  $\alpha = 4.5^\circ$  (b), and  $\alpha = 9.1^\circ$  (c). The array was located on the suction side and the turbulence grid was not installed.

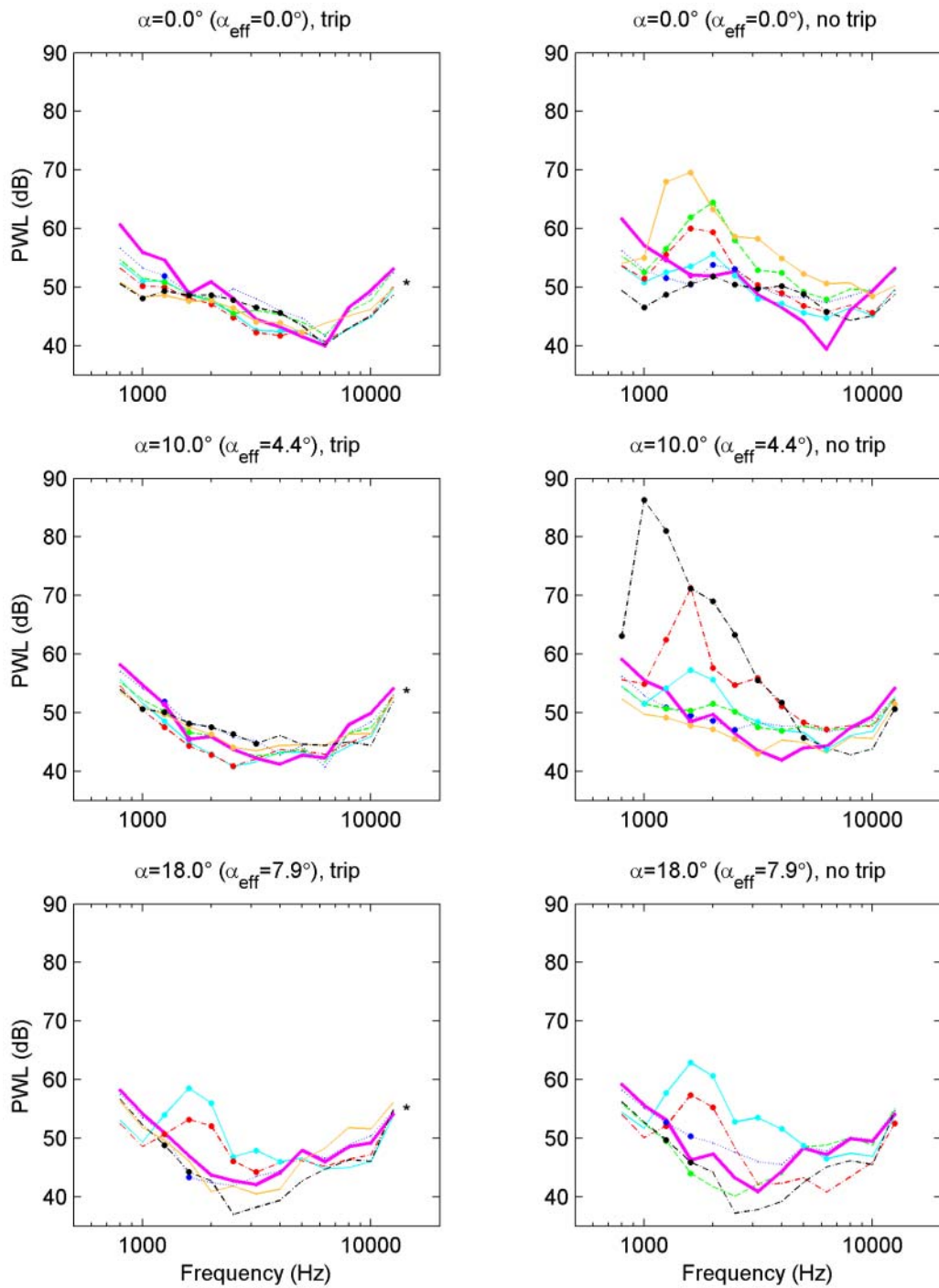


Figure 56. Comparison of trailing-edge noise levels for different airfoils at 32 m/s (array on suction side),  $\alpha = 0^\circ$  ( $\alpha_{eff} = 0.0^\circ$ );  $\alpha = 9.5^\circ$  ( $\alpha_{eff} = 4.4^\circ$ );  $\alpha = 18.0^\circ$  ( $\alpha_{eff} = 7.9^\circ$ );  $\alpha = 27.0^\circ$  ( $\alpha_{eff} = 12.4^\circ$ ).  $\alpha = 0^\circ$  ( $\alpha_{eff} = 0.0^\circ$ ), trip;  $\alpha = 0^\circ$  ( $\alpha_{eff} = 0.0^\circ$ ), no trip;  $\alpha = 10.0^\circ$  ( $\alpha_{eff} = 4.4^\circ$ ), trip;  $\alpha = 10.0^\circ$  ( $\alpha_{eff} = 4.4^\circ$ ), no trip;  $\alpha = 18.0^\circ$  ( $\alpha_{eff} = 7.9^\circ$ ), trip;  $\alpha = 18.0^\circ$  ( $\alpha_{eff} = 7.9^\circ$ ), no trip.  $\alpha = 0^\circ$  ( $\alpha_{eff} = 0.0^\circ$ ), trip;  $\alpha = 0^\circ$  ( $\alpha_{eff} = 0.0^\circ$ ), no trip;  $\alpha = 10.0^\circ$  ( $\alpha_{eff} = 4.4^\circ$ ), trip;  $\alpha = 10.0^\circ$  ( $\alpha_{eff} = 4.4^\circ$ ), no trip;  $\alpha = 18.0^\circ$  ( $\alpha_{eff} = 7.9^\circ$ ), trip;  $\alpha = 18.0^\circ$  ( $\alpha_{eff} = 7.9^\circ$ ), no trip.  $\alpha = 0^\circ$  ( $\alpha_{eff} = 0.0^\circ$ ), trip;  $\alpha = 0^\circ$  ( $\alpha_{eff} = 0.0^\circ$ ), no trip;  $\alpha = 10.0^\circ$  ( $\alpha_{eff} = 4.4^\circ$ ), trip;  $\alpha = 10.0^\circ$  ( $\alpha_{eff} = 4.4^\circ$ ), no trip;  $\alpha = 18.0^\circ$  ( $\alpha_{eff} = 7.9^\circ$ ), trip;  $\alpha = 18.0^\circ$  ( $\alpha_{eff} = 7.9^\circ$ ), no trip.

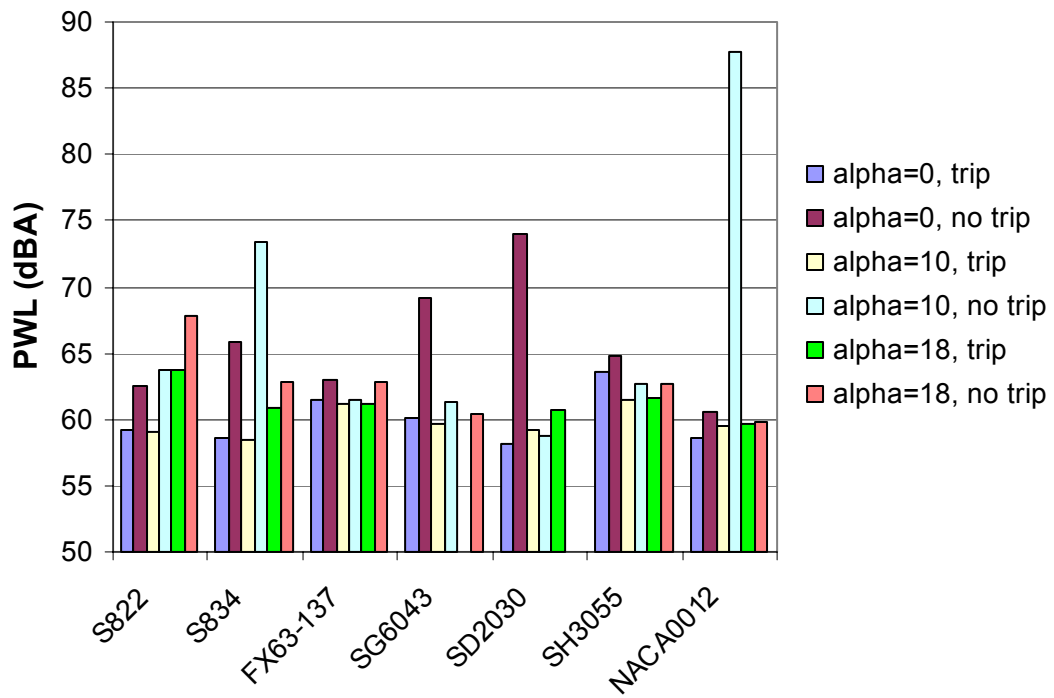


Figure 57. A-weighted overall trailing-edge noise levels for different airfoils at 32 m/s (based on the spectra shown in Figure 56)

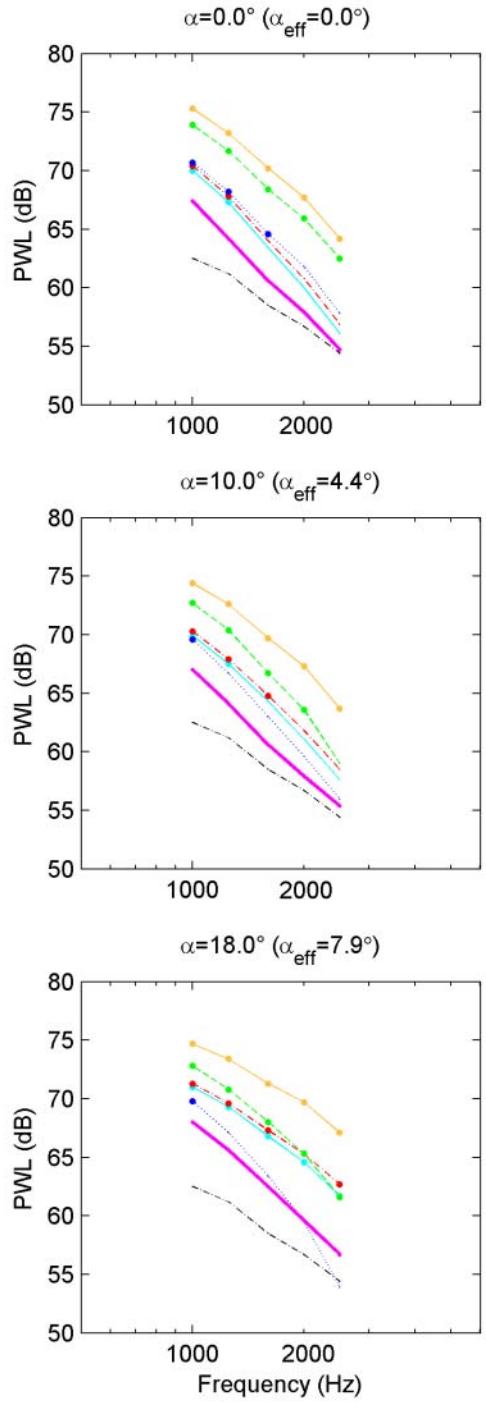


Figure 58. Comparison of inflow turbulence noise levels for different tripped airfoils at 32 m/s (array on suction side), — = S822; - - = S834; ...  = FX 63-137; - - SG 6043 (*no trip at  $\alpha = 18^\circ$* ); — SH 3055; — = SD 2030; - - = background noise (empty tunnel with grid)

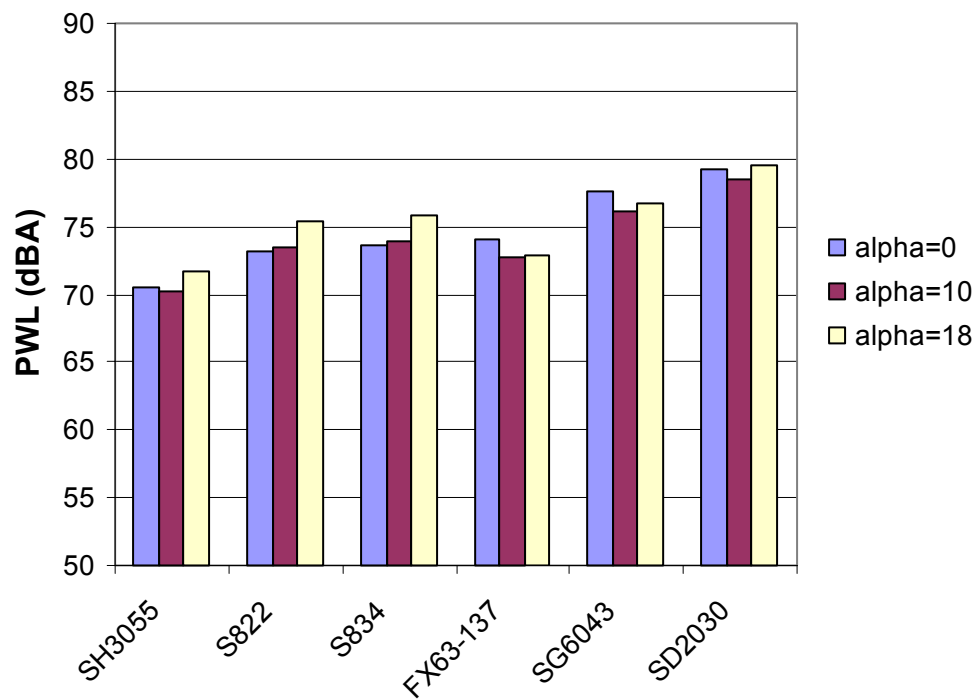


Figure 59. A-weighted overall inflow turbulence noise levels for different airfoils at 32 m/s (based on the spectra shown in Figure 58)

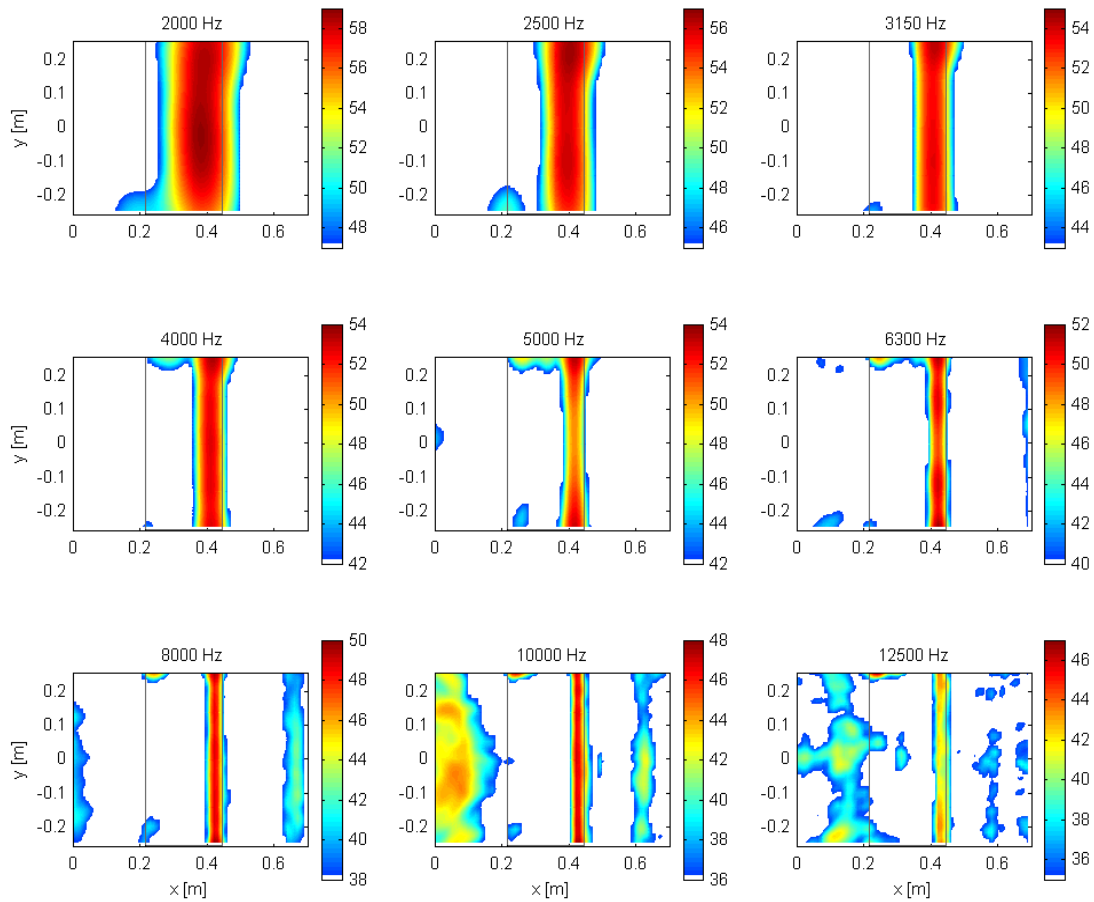


Figure 60. Acoustic source plots for tripped S822 airfoil with B4 MEMS, at 32 m/s and  $\alpha = 18^\circ$ , without turbulence grid (array on pressure side)

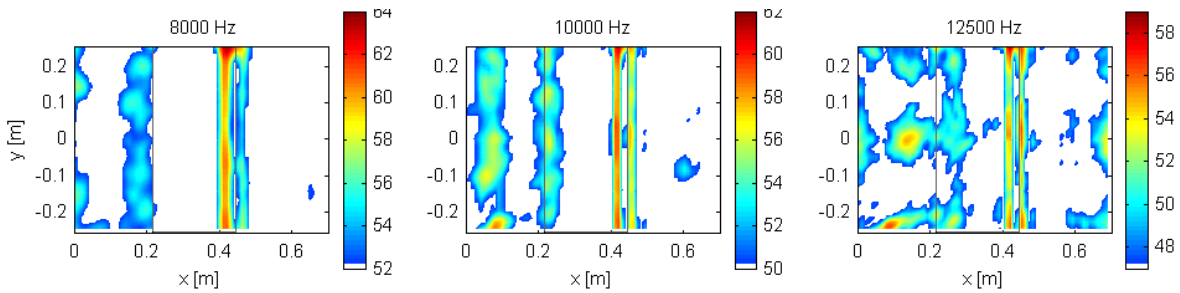


Figure 61. Acoustic source plots for tripped S822 airfoil with B2 MEMS, at 64 m/s and  $\alpha = 0^\circ$ , without turbulence grid (array on pressure side)

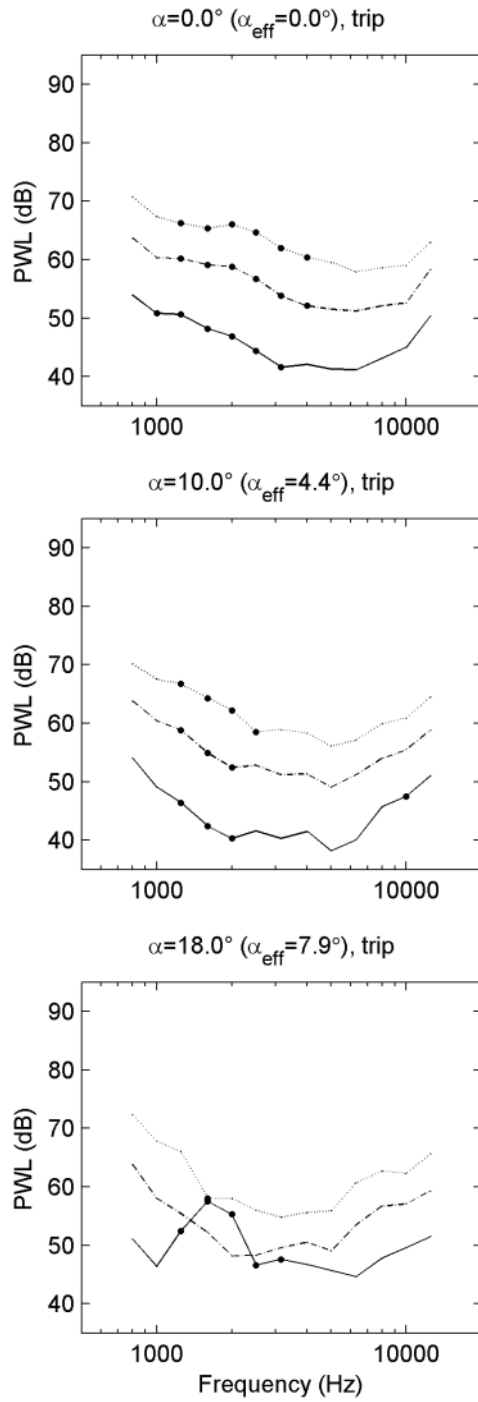


Figure 62. Trailing-edge noise spectra for tripped S822 airfoil as a reference for the MEMS measurements (array on pressure side),  $\text{--}$  = 32.0 m/s;  $\text{- -}$  = 47.9 m/s;  $\dots$  = 63.9 m/s

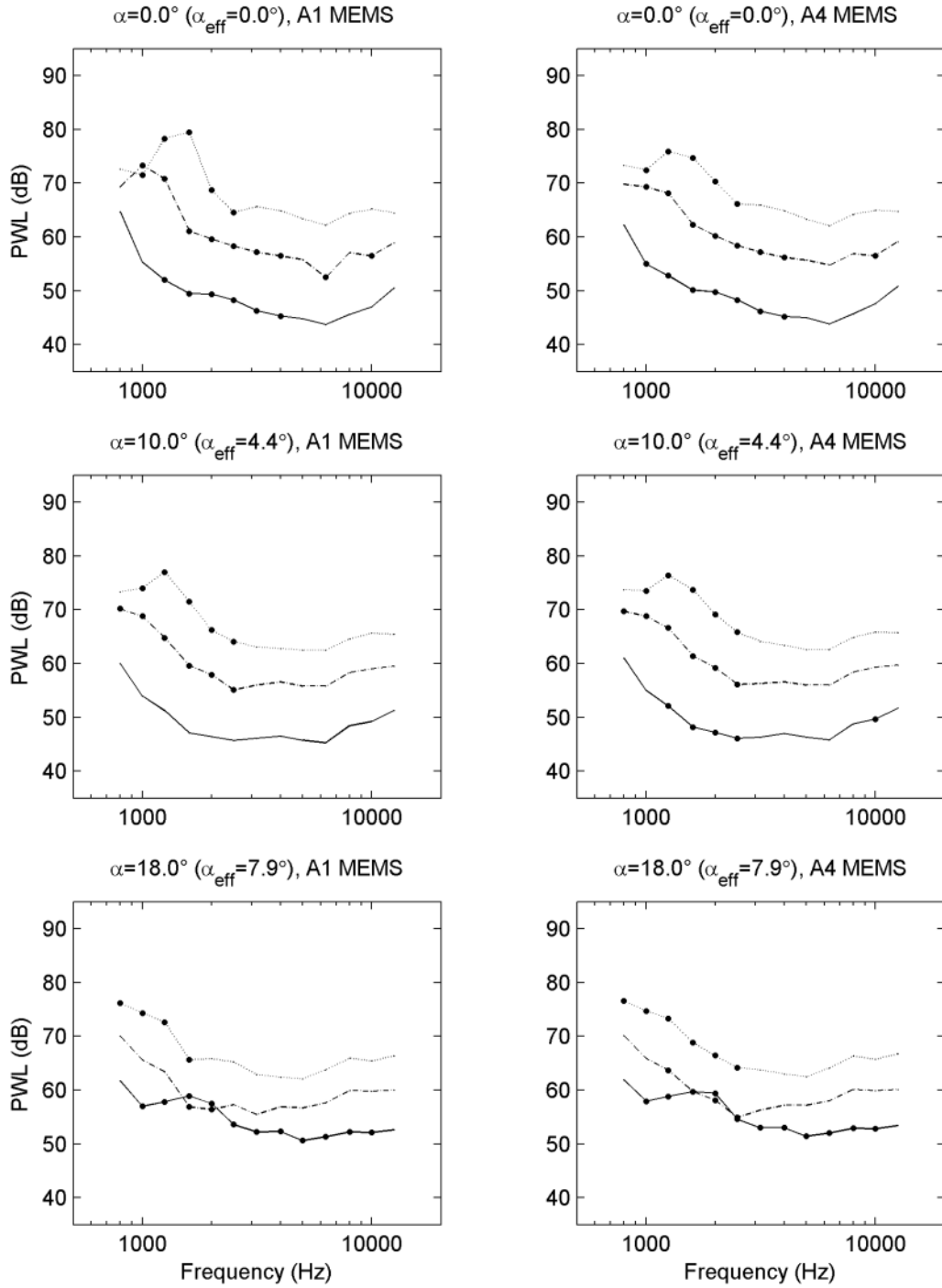


Figure 63. Trailing-edge noise spectra for tripped S822 airfoil with A1/A4 MEMS (array on pressure side),  $\underline{\quad}$  = 32.0 m/s;  $\underline{\quad}$  = 47.9 m/s;  $\dots$  = 63.9 m/s

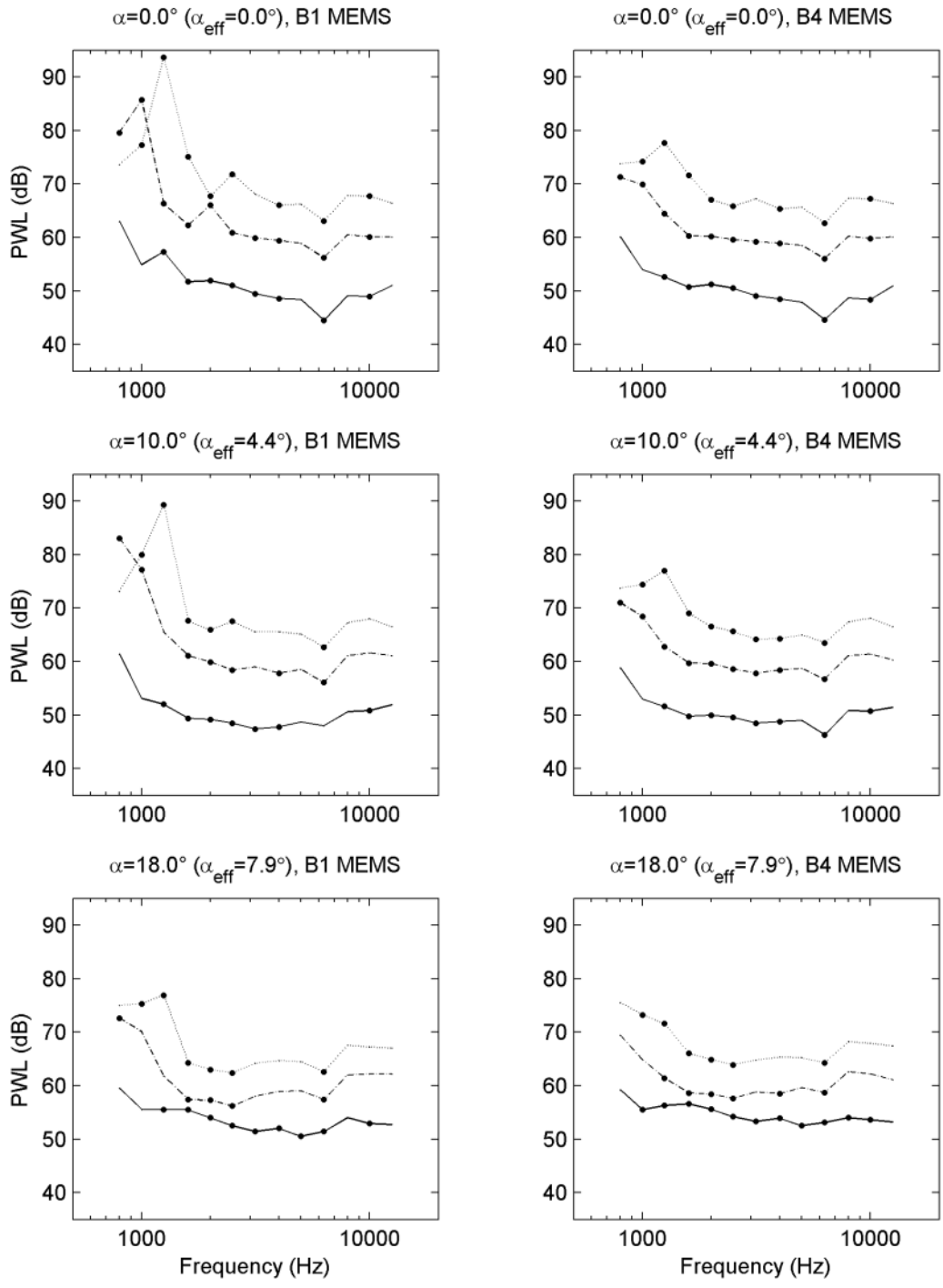
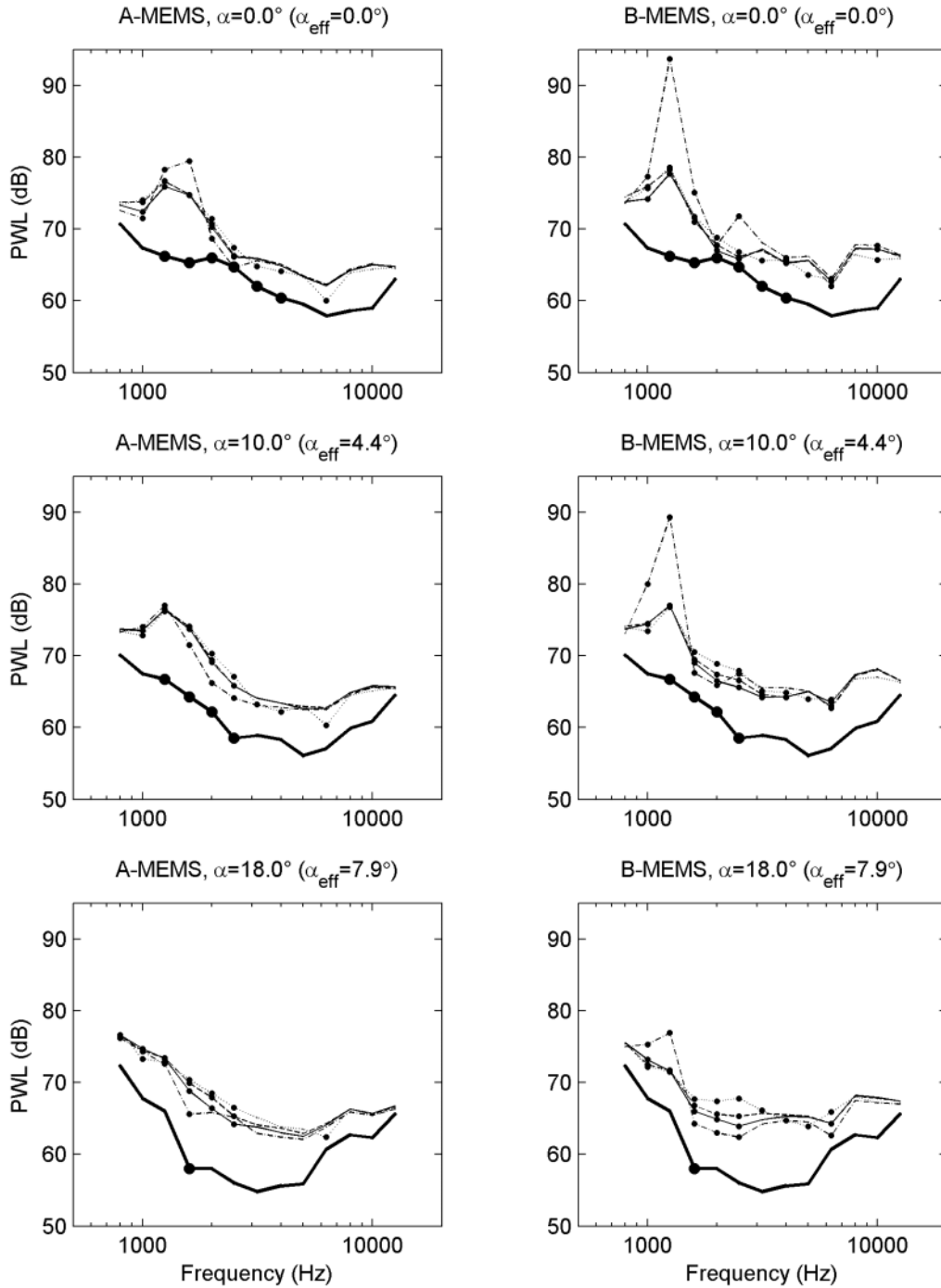


Figure 64. Trailing-edge noise spectra for tripped S822 airfoil with B1/B4 MEMS (array on pressure side),  $\underline{\quad}$  = 32.0 m/s;  $\underline{\quad}$  = 47.9 m/s;  $\dots$  = 63.9 m/s



**Figure 65. Trailing-edge noise spectra for tripped S822 airfoil with and without MEMS ( $U = 64$  m/s, array on pressure side),  $\text{—}$  = S822;  $\text{- -}$  = A1/B1;  $\dots$  = A2/B2;  $\text{- . -}$  = A3/B3;  $\text{— —}$  = A4/B4**

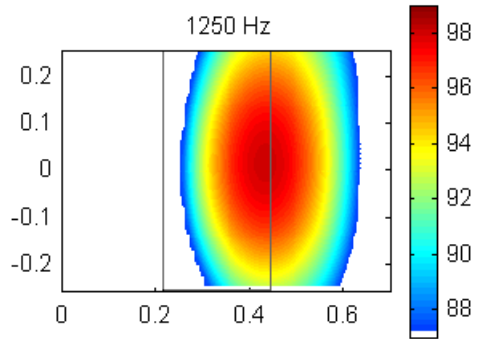


Figure 66. Acoustic source plot for tripped S822 airfoil with B1 MEMS, at 64 m/s and  $\alpha = 0^\circ$ , without turbulence grid (array on pressure side), indicating source position of MEMS tone

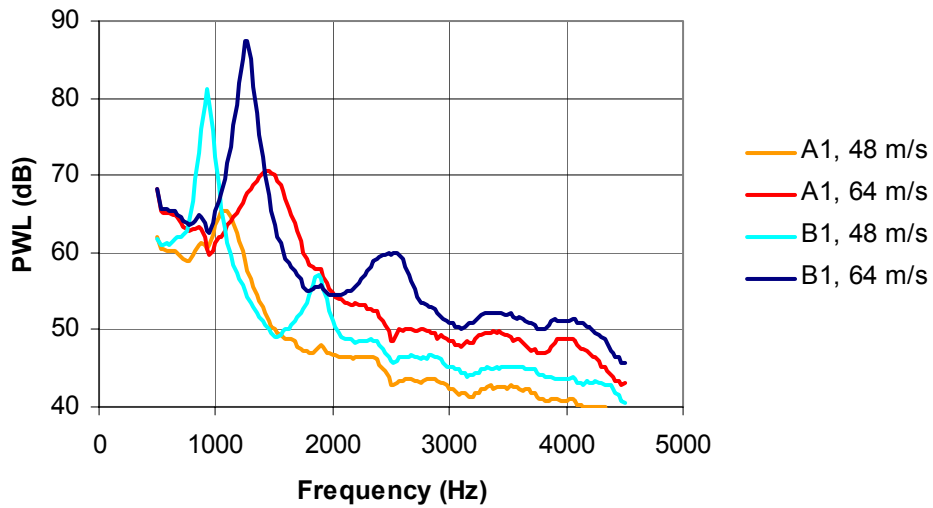


Figure 67. Narrowband trailing-edge noise spectra for tripped S822 airfoil with A1 and B1 MEMS at  $\alpha = 0^\circ$  (array on pressure side)

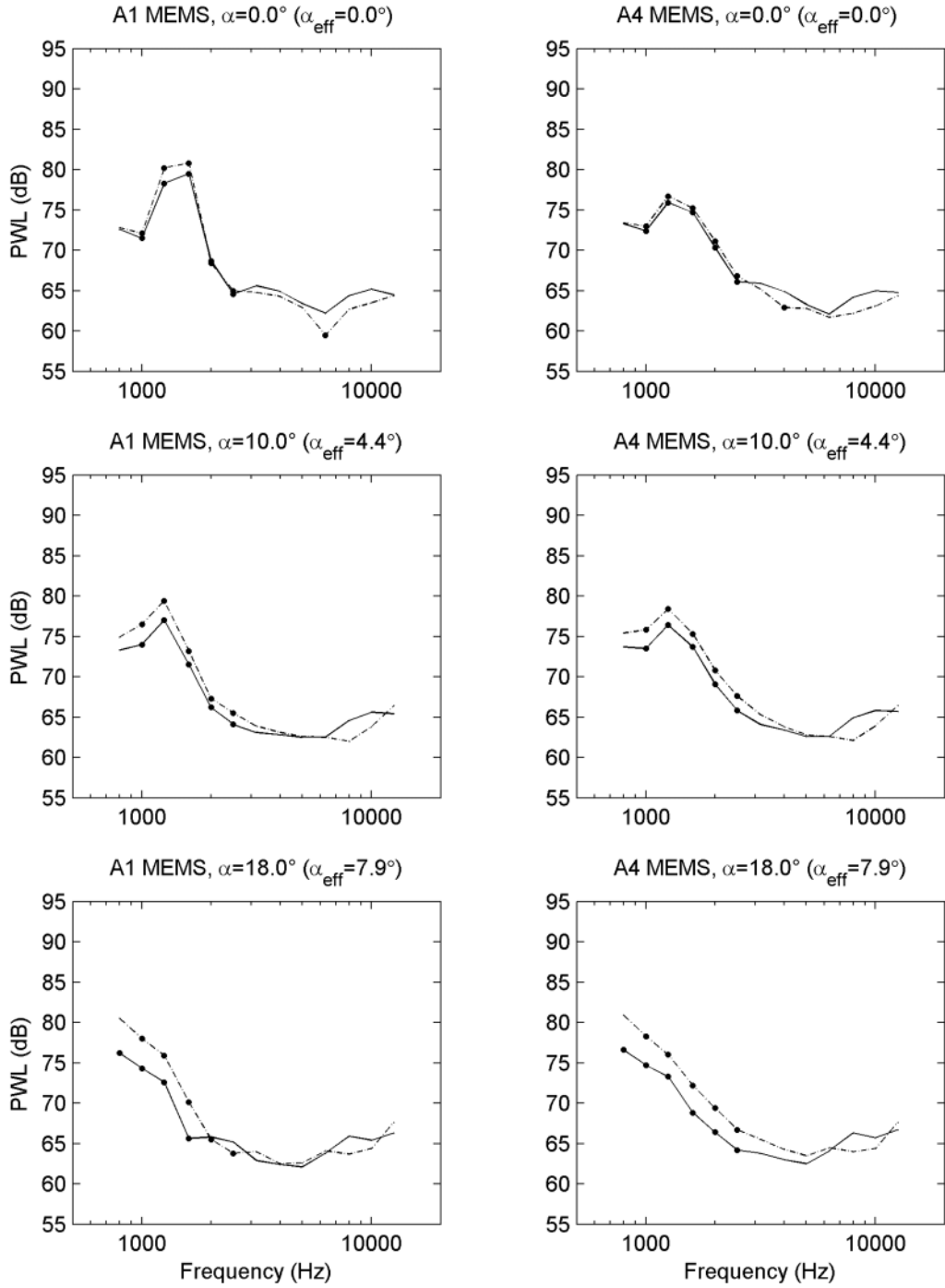


Figure 68. Trailing-edge noise spectra for tripped S822 airfoil with A1/A4 MEMS at 64 m/s, \_\_ = array on pressure side; \_ \_ = array on suction side

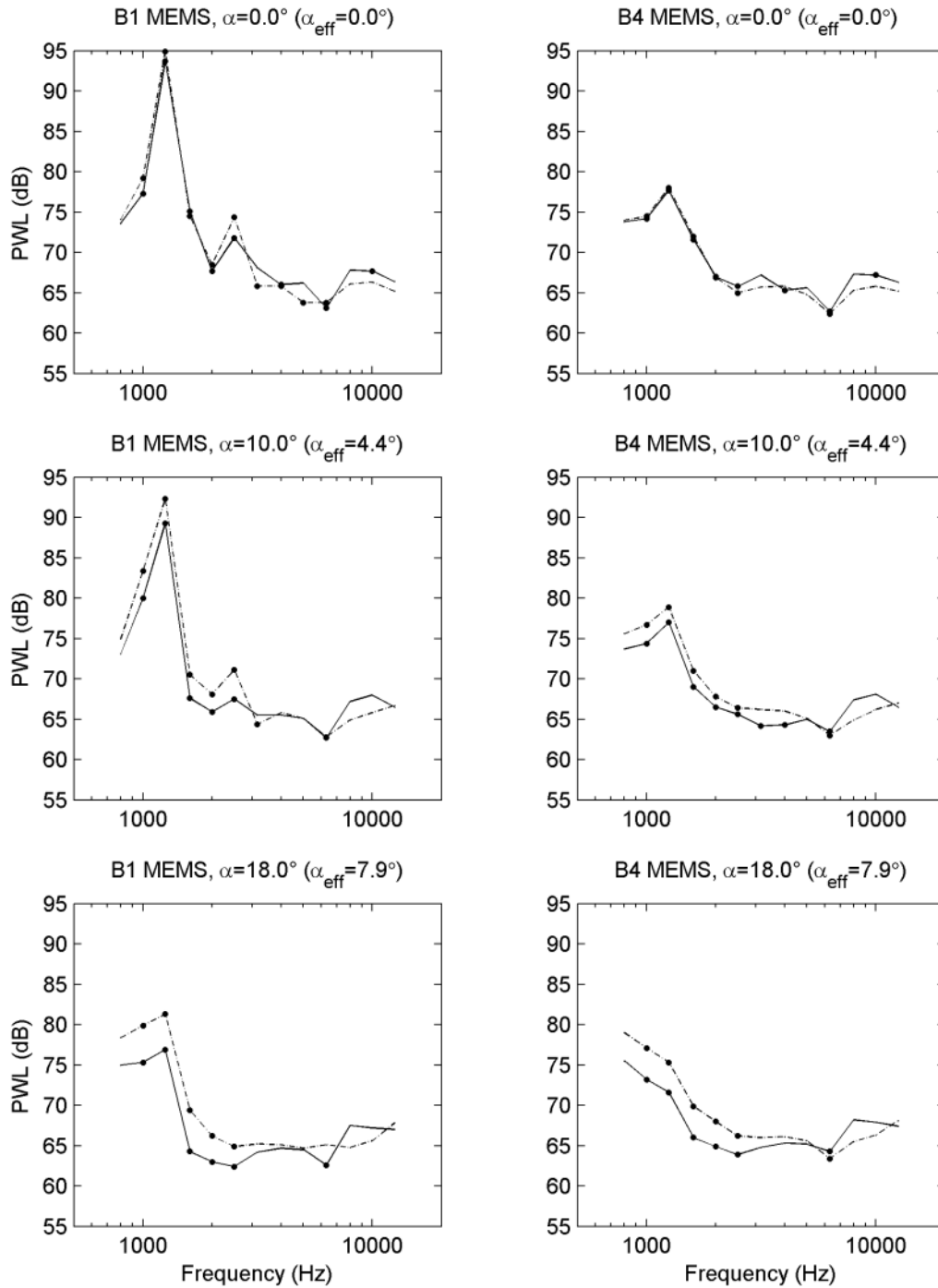


Figure 69. Trailing-edge noise spectra for tripped S822 airfoil with B1/B4 MEMS at 64 m/s, \_\_ = array on pressure side; \_ \_ = array on suction side

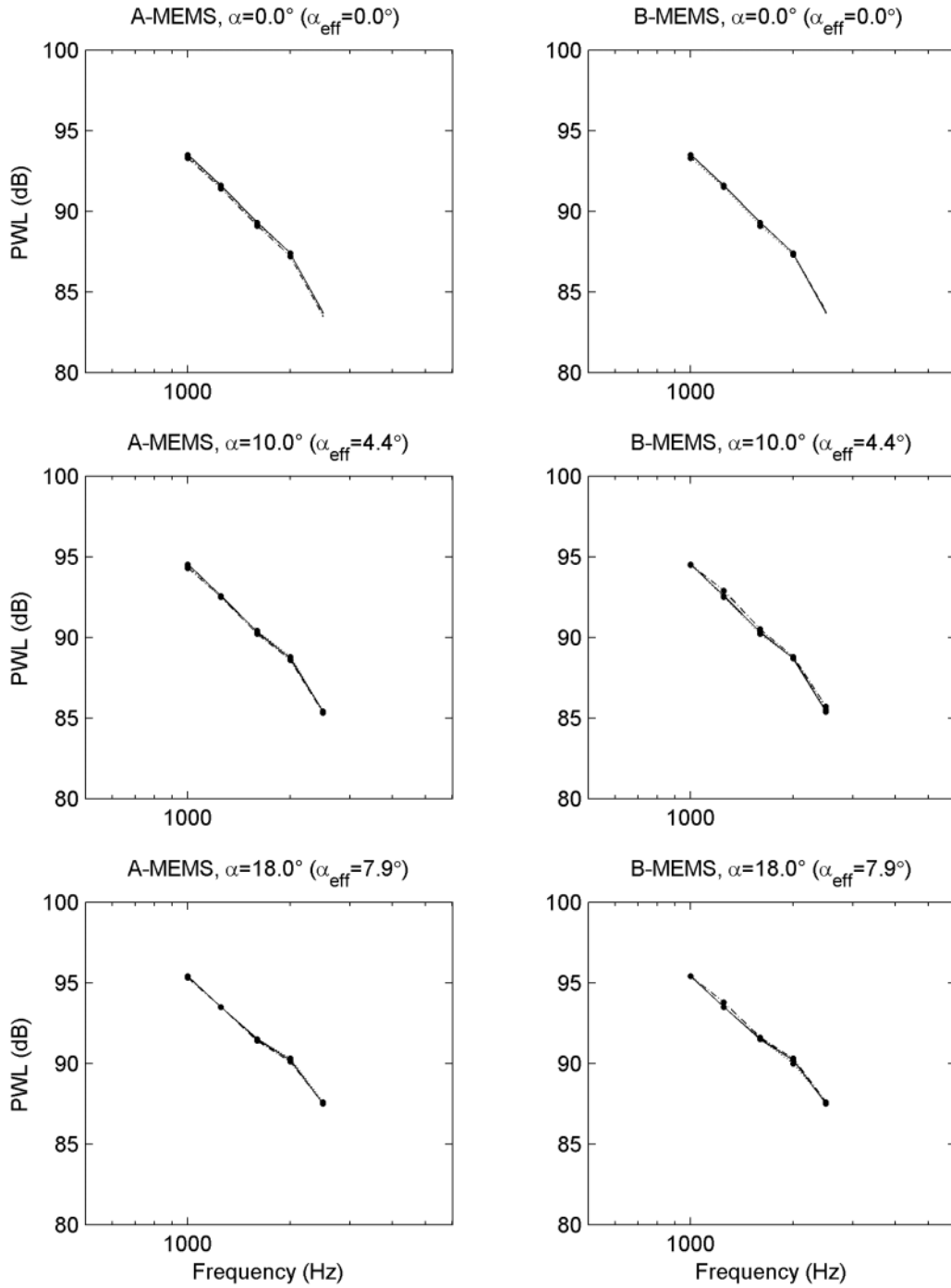


Figure 70. Inflow turbulence noise spectra for S822 airfoil with and without MEMS ( $U = 64$  m/s, array on pressure side),  $\_ \_$  = S822;  $\_ \_ \_$  = A1/B1;  $\_ \_ \_ \_$  = A4/B4

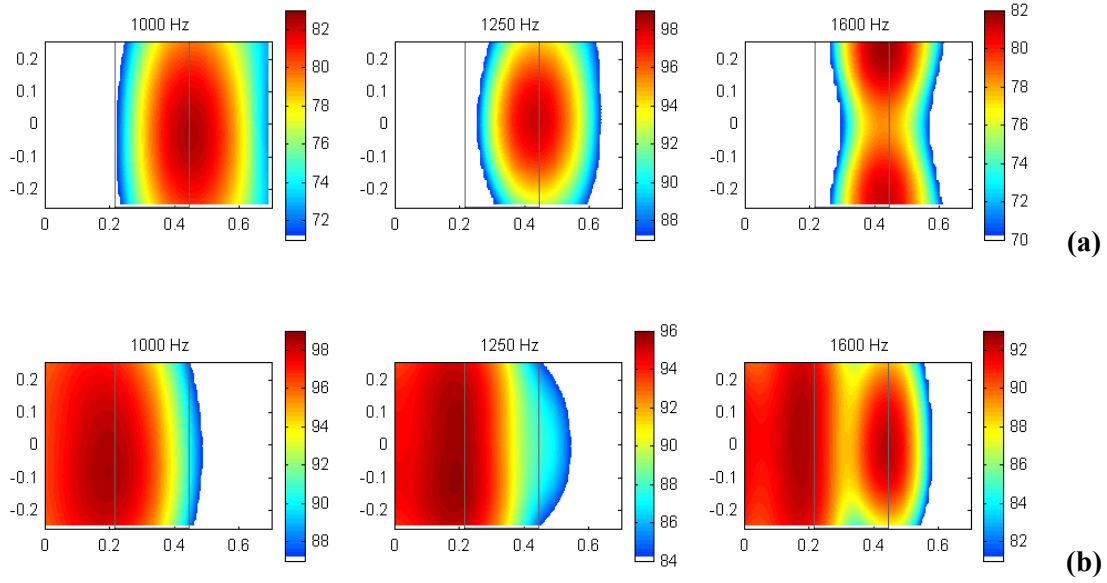


Figure 71. Acoustic source plots for tripped S822 airfoil with B1 MEMS at 64 m/s and  $\alpha = 0^\circ$ , without (a) and with (b) turbulence grid (array on pressure side, note that the color scales are different)

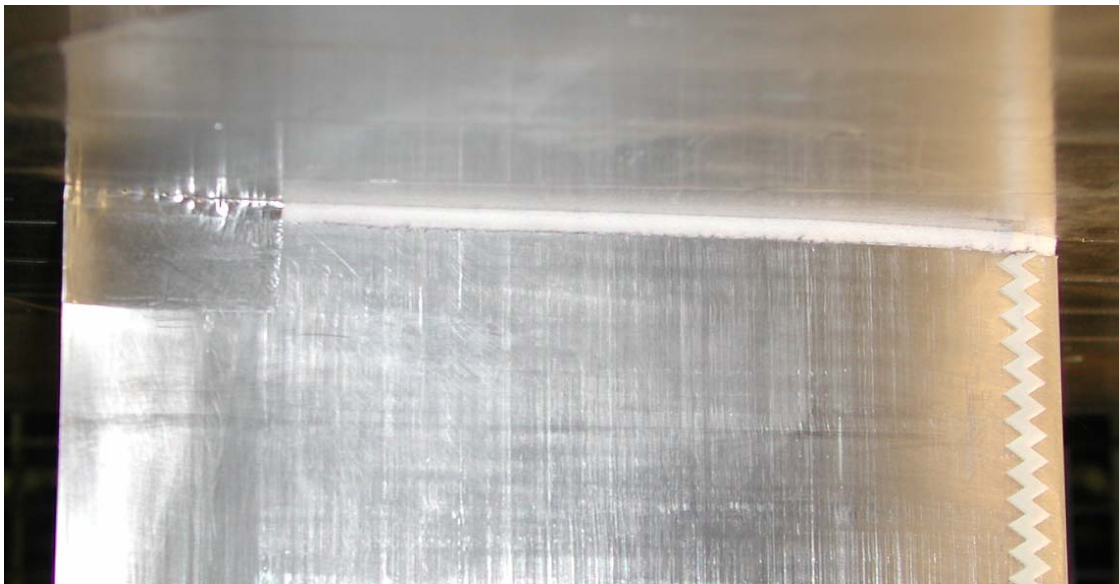


Figure 72. Model-endplate gap treatment consisting of foam and tape at the trailing edge

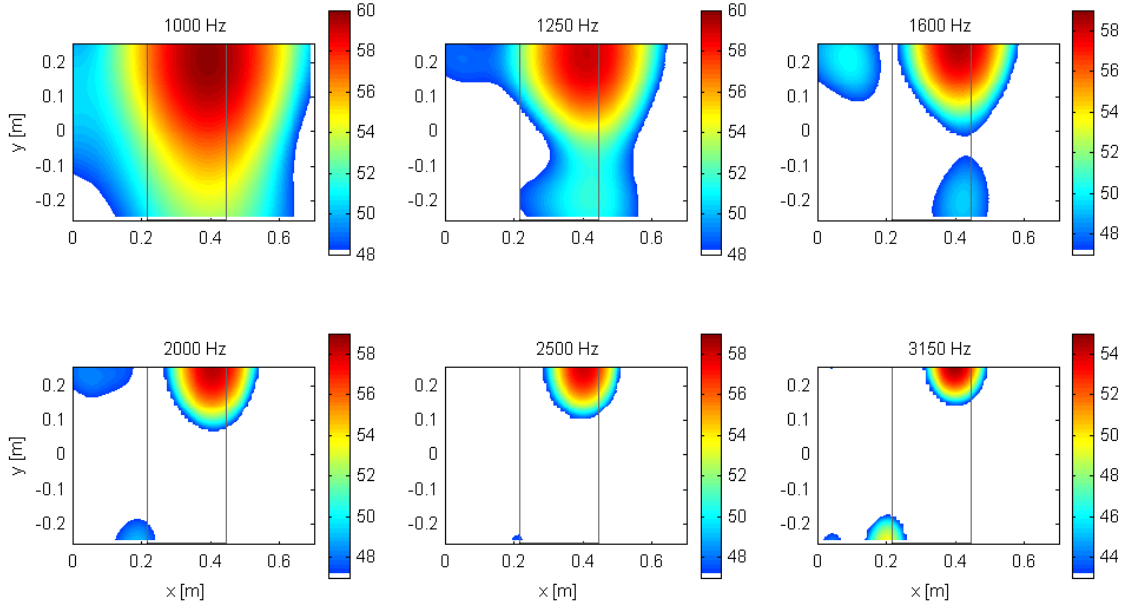


Figure 73. Acoustic source plots for tripped FX 63-137 airfoil at 32 m/s and  $\alpha = 14^\circ$  (array on suction side), without porous treatment on model edges (compare to Figure 74, note the different color scales)

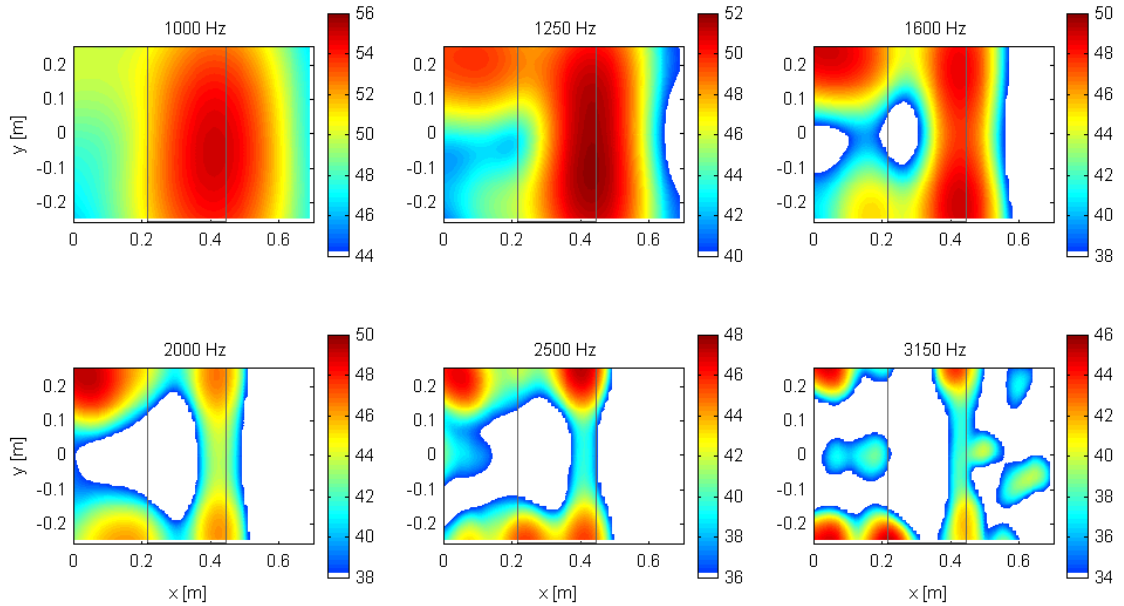


Figure 74. Acoustic source plots for tripped FX 63-137 airfoil at 32 m/s and  $\alpha = 14^\circ$  (array on suction side), with porous treatment on model edges (compare to Figure 73, note the different color scales)

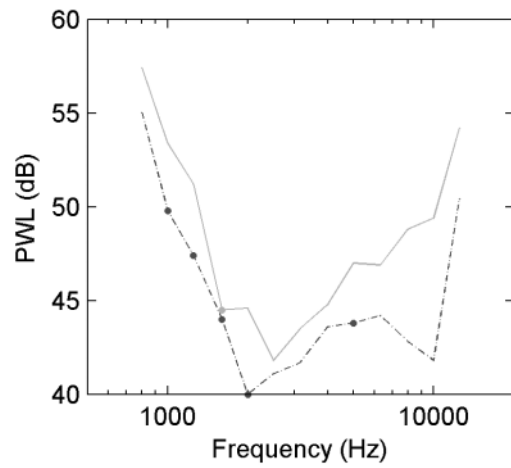


Figure 75. Trailing-edge noise spectra for tripped FX 63-137 airfoil at 32 m/s and  $\alpha = 14^\circ$  (array on suction side), illustrating the effectiveness of porous edge treatment in reducing extraneous “corner sources”, \_\_\_ = untreated; \_.\_ = treated

## Appendix 1. Test Matrix

### Column headers:

Run:	run number
Polar:	polar number
DPN:	data point number
$\alpha$ :	geometrical model angle of attack (degrees)
$\alpha_{\text{eff}}$ :	effective model angle of attack (degrees)
M:	tunnel Mach number
V:	tunnel speed (m/s)
Ttot:	tunnel temperature (K)
C:	speed of sound (m/s)
Airfoil:	airfoil ID
Trip SS:	trip thickness on suction side
Trip PS:	trip thickness on pressure side
Grid:	presence of turbulence grid in nozzle
Array:	position of array ( <u>s</u> uction <u>s</u> ide or <u>p</u> ressure <u>s</u> ide of the model)
Info:	additional remarks

Run	Polar	DPN	$\alpha$	$\alpha_{eff}$	M	V	Ttot	C	Airfoil	Trip SS	Trip PS	Grid	Array	Info
31	1	751	0.00	0.00	0.093	31.7	286	340.4	NACA0012	0.25	0.25	no grid	SS	
31	1	752	3.58	1.58	0.093	31.7	286	340.6	NACA0012	0.25	0.25	no grid	SS	
31	1	753	3.58	1.58	0.093	31.7	286	340.9	NACA0012	0.25	0.25	no grid	SS	
31	1	754	7.18	3.17	0.093	31.7	285	340.8	NACA0012	0.25	0.25	no grid	SS	
31	1	755	9.49	4.19	0.094	31.7	285	337.2	NACA0012	0.25	0.25	no grid	SS	
31	1	756	13.11	5.79	0.094	31.8	285	337.9	NACA0012	0.25	0.25	no grid	SS	
31	2	757	0.00	0.00	0.117	39.6	287	338.5	NACA0012	0.25	0.25	no grid	SS	
31	2	758	3.58	1.58	0.117	39.6	287	338.5	NACA0012	0.25	0.25	no grid	SS	
31	2	759	7.18	3.17	0.117	39.6	287	338.5	NACA0012	0.25	0.25	no grid	SS	
31	2	760	9.51	4.20	0.117	39.7	287	338.9	NACA0012	0.25	0.25	no grid	SS	
31	2	761	13.10	5.78	0.117	39.7	287	339.4	NACA0012	0.25	0.25	no grid	SS	
32	1	764	-0.01	0.00	0.163	55.6	291	340.9	NACA0012	0.25	0.25	no grid	SS	
32	1	765	3.58	1.58	0.163	55.6	291	341.1	NACA0012	0.25	0.25	no grid	SS	
32	1	766	7.18	3.17	0.163	55.6	291	341.3	NACA0012	0.25	0.25	no grid	SS	
32	1	767	9.49	4.19	0.163	55.7	291	341.4	NACA0012	0.25	0.25	no grid	SS	
32	1	768	13.10	5.78	0.163	55.7	291	341.9	NACA0012	0.25	0.25	no grid	SS	
32	2	769	0.00	0.00	0.207	71.4	297	345.0	NACA0012	0.25	0.25	no grid	SS	
32	2	770	3.57	1.58	0.207	71.6	298	345.7	NACA0012	0.25	0.25	no grid	SS	
32	2	771	7.19	3.17	0.207	71.6	299	346.0	NACA0012	0.25	0.25	no grid	SS	
32	2	772	9.51	4.20	0.207	71.7	299	346.4	NACA0012	0.25	0.25	no grid	SS	
32	2	773	13.10	5.78	0.208	71.8	299	345.2	NACA0012	0.25	0.25	no grid	SS	
33	1	776	13.10	5.78	0.094	32.0	287	340.6	NACA0012	0.25	0.25	no grid	SS	+plasticine
34	1	779	-0.01	0.00	0.094	31.7	285	337.6	NACA0012	0	0	no grid	SS	
34	1	780	3.58	1.58	0.094	31.7	284	337.6	NACA0012	0	0	no grid	SS	
34	1	781	7.18	3.17	0.094	31.7	284	337.2	NACA0012	0	0	no grid	SS	
34	1	782	9.50	4.19	0.094	31.7	284	337.4	NACA0012	0	0	no grid	SS	
34	1	783	13.11	5.79	0.094	31.8	284	337.9	NACA0012	0	0	no grid	SS	
34	2	784	0.00	0.00	0.117	39.6	286	338.4	NACA0012	0	0	no grid	SS	
34	2	785	3.58	1.58	0.117	39.6	286	338.4	NACA0012	0	0	no grid	SS	
34	2	786	7.18	3.17	0.117	39.6	286	338.5	NACA0012	0	0	no grid	SS	
34	2	787	9.50	4.19	0.117	39.6	286	338.7	NACA0012	0	0	no grid	SS	
34	2	788	13.11	5.79	0.117	39.7	286	339.1	NACA0012	0	0	no grid	SS	
34	3	789	0.00	0.00	0.163	55.6	290	340.8	NACA0012	0	0	no grid	SS	
34	3	790	3.58	1.58	0.163	55.6	290	341.2	NACA0012	0	0	no grid	SS	
34	3	791	7.18	3.17	0.163	55.6	291	341.3	NACA0012	0	0	no grid	SS	
34	3	792	9.50	4.19	0.163	55.7	291	341.7	NACA0012	0	0	no grid	SS	
34	3	793	13.11	5.79	0.163	55.8	291	342.1	NACA0012	0	0	no grid	SS	
34	4	794	0.00	0.00	0.207	71.4	297	344.7	NACA0012	0	0	no grid	SS	
34	4	795	3.58	1.58	0.207	71.5	298	345.6	NACA0012	0	0	no grid	SS	
34	4	796	7.18	3.17	0.207	71.6	298	346.0	NACA0012	0	0	no grid	SS	
34	4	797	9.51	4.20	0.208	71.7	299	344.9	NACA0012	0	0	no grid	SS	
34	4	798	13.10	5.78	0.208	71.8	299	345.1	NACA0012	0	0	no grid	SS	
37	1	834	-0.01	0.00	0.038	12.8	284	336.8	S822	0.25	0.25	no grid	SS	
37	1	835	10.00	4.42	0.038	12.8	284	336.6	S822	0.25	0.25	no grid	SS	
37	1	836	18.01	7.95	0.038	12.8	284	337.9	S822	0.25	0.25	no grid	SS	
37	2	837	0.00	0.00	0.066	22.4	284	339.4	S822	0.25	0.25	no grid	SS	
37	2	838	10.01	4.42	0.066	22.4	284	339.4	S822	0.25	0.25	no grid	SS	
37	2	839	18.00	7.95	0.066	22.5	284	340.3	S822	0.25	0.25	no grid	SS	
37	3	840	0.00	0.00	0.094	32.0	285	340.4	S822	0.25	0.25	no grid	SS	
37	3	841	10.00	4.42	0.094	32.0	286	340.7	S822	0.25	0.25	no grid	SS	
37	3	842	18.01	7.95	0.095	32.1	286	338.3	S822	0.25	0.25	no grid	SS	
37	4	843	0.00	0.00	0.141	48.0	289	340.4	S822	0.25	0.25	no grid	SS	
37	4	844	9.99	4.41	0.141	48.1	290	340.8	S822	0.25	0.25	no grid	SS	

Run	Polar	DPN	$\alpha$	$\alpha_{eff}$	M	V	Ttot	C	Airfoil	Trip SS	Trip PS	Grid	Array	Info
37	4	845	18.01	7.95	0.141	48.2	290	341.9	S822	0.25	0.25	no grid	SS	
37	5	846	0.00	0.00	0.186	63.9	295	343.4	S822	0.25	0.25	no grid	SS	
37	5	847	10.00	4.42	0.186	64.0	296	343.9	S822	0.25	0.25	no grid	SS	
37	5	848	18.00	7.95	0.186	64.2	297	345.3	S822	0.25	0.25	no grid	SS	
38	1	851	0.00	0.00	0.038	12.7	286	335.0	S822	0.25	0.25	grid	SS	
38	1	852	10.01	4.42	0.038	12.7	285	334.7	S822	0.25	0.25	grid	SS	
38	1	853	18.01	7.95	0.038	12.8	285	336.6	S822	0.25	0.25	grid	SS	
38	2	854	-0.01	0.00	0.066	22.4	285	339.4	S822	0.25	0.25	grid	SS	
38	2	855	10.00	4.42	0.066	22.4	285	339.4	S822	0.25	0.25	grid	SS	
38	2	856	18.00	7.95	0.066	22.5	285	340.2	S822	0.25	0.25	grid	SS	
38	3	857	0.00	0.00	0.094	32.0	287	340.6	S822	0.25	0.25	grid	SS	
38	3	858	10.01	4.42	0.094	32.0	286	340.1	S822	0.25	0.25	grid	SS	
38	3	859	18.01	7.95	0.094	32.0	286	340.7	S822	0.25	0.25	grid	SS	
38	4	860	0.00	0.00	0.14	47.9	289	342.1	S822	0.25	0.25	grid	SS	
38	4	861	10.00	4.42	0.14	47.9	290	342.1	S822	0.25	0.25	grid	SS	
38	4	862	18.00	7.95	0.141	48.0	290	340.2	S822	0.25	0.25	grid	SS	
38	5	863	0.00	0.00	0.186	63.9	296	343.7	S822	0.25	0.25	grid	SS	
38	5	864	9.99	4.41	0.186	63.9	296	343.8	S822	0.25	0.25	grid	SS	
38	5	865	18.00	7.95	0.186	64.1	296	344.4	S822	0.25	0.25	grid	SS	
41	1	900	-0.01	0.00	0.038	12.8	285	337.6	S822	0	0	grid	SS	
41	1	901	10.00	4.42	0.038	12.8	285	337.4	S822	0	0	grid	SS	
41	1	902	18.00	7.95	0.038	12.8	284	337.4	S822	0	0	grid	SS	
41	2	903	0.00	0.00	0.066	22.4	285	339.8	S822	0	0	grid	SS	
41	2	904	10.00	4.42	0.066	22.4	285	339.5	S822	0	0	grid	SS	
41	2	905	18.01	7.95	0.066	22.5	285	340.2	S822	0	0	grid	SS	
41	3	906	0.01	0.00	0.094	32.0	286	340.1	S822	0	0	grid	SS	
41	3	907	9.99	4.41	0.094	32.0	286	340.2	S822	0	0	grid	SS	
41	3	908	18.00	7.95	0.094	32.0	286	340.6	S822	0	0	grid	SS	
41	4	909	-0.01	0.00	0.141	48.0	289	340.1	S822	0	0	grid	SS	
41	4	910	10.01	4.42	0.141	48.0	290	340.4	S822	0	0	grid	SS	
41	4	911	18.00	7.95	0.141	48.1	290	341.2	S822	0	0	grid	SS	
41	5	912	0.00	0.00	0.186	64.1	296	344.7	S822	0	0	grid	SS	
41	5	913	10.00	4.42	0.186	64.2	296	344.9	S822	0	0	grid	SS	
41	5	914	17.99	7.94	0.187	64.3	297	344.0	S822	0	0	grid	SS	
42	1	917	0.00	0.00	0.038	12.8	286	337.1	S822	0	0	no grid	SS	
42	1	918	10.01	4.42	0.038	12.8	285	337.9	S822	0	0	no grid	SS	
42	1	919	18.01	7.95	0.038	12.8	285	337.9	S822	0	0	no grid	SS	
42	2	920	0.00	0.00	0.066	22.4	285	338.8	S822	0	0	no grid	SS	
42	2	921	9.99	4.41	0.066	22.4	286	338.8	S822	0	0	no grid	SS	
42	2	922	17.99	7.94	0.066	22.4	285	339.7	S822	0	0	no grid	SS	
42	3	923	0.00	0.00	0.094	32.0	287	340.4	S822	0	0	no grid	SS	
42	3	924	10.00	4.42	0.094	32.0	287	340.6	S822	0	0	no grid	SS	
42	3	925	18.01	7.95	0.095	32.2	287	338.4	S822	0	0	no grid	SS	
42	4	926	0.00	0.00	0.14	47.9	290	342.1	S822	0	0	no grid	SS	
42	4	927	10.01	4.42	0.14	48.0	291	342.5	S822	0	0	no grid	SS	
42	4	928	18.00	7.95	0.141	48.1	291	341.3	S822	0	0	no grid	SS	
42	5	929	0.00	0.00	0.185	63.9	297	345.6	S822	0	0	no grid	SS	
42	5	930	9.99	4.41	0.186	64.0	297	344.2	S822	0	0	no grid	SS	
42	5	931	18.01	7.95	0.186	64.2	298	345.2	S822	0	0	no grid	SS	

Run	Polar	DPN	$\alpha$	$\alpha_{eff}$	M	V	Ttot	C	Airfoil	Trip SS	Trip PS	Grid	Array	Info
45	1	966	-0.01	0.00	0.038	12.9	285	339.5	S834	0.25	0.25	no grid	SS	
45	1	967	10.01	4.42	0.038	12.9	285	338.2	S834	0.25	0.25	no grid	SS	
45	1	968	18.00	7.95	0.038	12.9	285	339.5	S834	0.25	0.25	no grid	SS	
45	2	969	0.01	0.00	0.066	22.3	285	338.5	S834	0.25	0.25	no grid	SS	
45	2	970	9.99	4.41	0.066	22.4	285	338.9	S834	0.25	0.25	no grid	SS	
45	2	971	18.00	7.95	0.066	22.5	285	340.3	S834	0.25	0.25	no grid	SS	
45	3	972	0.00	0.00	0.094	32.0	286	340.1	S834	0.25	0.25	no grid	SS	
45	3	973	10.00	4.42	0.094	32.0	286	340.5	S834	0.25	0.25	no grid	SS	
45	3	974	17.99	7.94	0.094	32.1	286	341.2	S834	0.25	0.25	no grid	SS	
45	4	975	0.00	0.00	0.14	47.9	290	342.1	S834	0.25	0.25	no grid	SS	
45	4	976	10.00	4.42	0.14	48.0	290	342.6	S834	0.25	0.25	no grid	SS	
45	4	977	18.01	7.95	0.141	48.1	291	341.3	S834	0.25	0.25	no grid	SS	
46	1	980	0.01	0.00	0.038	12.8	285	336.8	S834	0.25	0.25	grid	SS	
46	1	981	10.00	4.42	0.038	12.8	285	337.4	S834	0.25	0.25	grid	SS	
46	1	982	18.00	7.95	0.038	12.9	285	338.4	S834	0.25	0.25	grid	SS	
46	2	983	-0.01	0.00	0.066	22.5	285	340.3	S834	0.25	0.25	grid	SS	
46	2	984	10.00	4.42	0.066	22.4	285	340.0	S834	0.25	0.25	grid	SS	
46	2	985	18.00	7.95	0.066	22.5	285	340.3	S834	0.25	0.25	grid	SS	
46	3	986	0.00	0.00	0.094	32.0	286	340.2	S834	0.25	0.25	grid	SS	
46	3	987	10.00	4.42	0.094	32.0	286	340.3	S834	0.25	0.25	grid	SS	
46	3	988	18.00	7.95	0.094	32.0	286	340.7	S834	0.25	0.25	grid	SS	
46	4	989	0.00	0.00	0.141	48.0	289	340.4	S834	0.25	0.25	grid	SS	
46	4	990	9.99	4.41	0.141	48.0	290	340.6	S834	0.25	0.25	grid	SS	
46	4	991	18.01	7.95	0.141	48.1	290	341.2	S834	0.25	0.25	grid	SS	
49	1	1026	0.00	0.00	0.038	12.8	285	336.8	S834	0	0	grid	SS	
49	1	1027	9.99	4.41	0.038	12.8	285	335.5	S834	0	0	grid	SS	
49	1	1028	18.00	7.95	0.038	12.8	285	336.6	S834	0	0	grid	SS	
49	2	1029	0.00	0.00	0.066	22.4	285	339.2	S834	0	0	grid	SS	
49	2	1030	10.00	4.42	0.066	22.4	285	339.2	S834	0	0	grid	SS	
49	2	1031	18.01	7.95	0.066	22.5	285	340.5	S834	0	0	grid	SS	
49	4	1032	0.00	0.00	0.094	32.0	286	340.7	S834	0	0	grid	SS	
49	4	1033	10.01	4.42	0.094	32.0	286	340.9	S834	0	0	grid	SS	
49	4	1034	18.01	7.95	0.095	32.1	286	337.6	S834	0	0	grid	SS	
49	5	1035	0.00	0.00	0.141	47.9	289	339.6	S834	0	0	grid	SS	
49	5	1036	10.01	4.42	0.141	47.9	289	339.9	S834	0	0	grid	SS	
49	5	1037	18.00	7.95	0.141	48.0	290	340.4	S834	0	0	grid	SS	
50	1	1040	0.00	0.00	0.038	12.8	286	337.4	S834	0	0	no grid	SS	
50	1	1041	9.99	4.41	0.038	12.8	285	337.1	S834	0	0	no grid	SS	
50	1	1043	18.01	7.95	0.038	12.8	285	337.1	S834	0	0	no grid	SS	
50	2	1044	0.01	0.00	0.066	22.4	285	339.4	S834	0	0	no grid	SS	
50	2	1045	10.00	4.42	0.066	22.4	285	339.8	S834	0	0	no grid	SS	
50	2	1046	18.01	7.95	0.066	22.5	285	340.8	S834	0	0	no grid	SS	
50	3	1047	0.00	0.00	0.094	32.0	286	340.6	S834	0	0	no grid	SS	
50	3	1048	10.00	4.42	0.094	32.1	286	341.0	S834	0	0	no grid	SS	
50	3	1049	18.00	7.95	0.095	32.1	287	338.2	S834	0	0	no grid	SS	
50	4	1050	0.00	0.00	0.14	47.9	290	342.2	S834	0	0	no grid	SS	
50	4	1051	10.00	4.42	0.14	48.0	291	342.5	S834	0	0	no grid	SS	
50	4	1052	18.01	7.95	0.141	48.1	291	341.1	S834	0	0	no grid	SS	
53	1	1091	0.00	0.00	0.038	12.8	284	337.6	S822+B1	0.25	0.25	no grid	SS	
53	1	1092	10.01	4.42	0.038	12.8	284	337.4	S822+B1	0.25	0.25	no grid	SS	

Run	Polar	DPN	$\alpha$	$\alpha_{eff}$	M	V	Ttot	C	Airfoil	Trip SS	Trip PS	Grid	Array	Info
53	1	1093	18.00	7.95	0.038	12.8	284	337.4	S822+B1	0.25	0.25	no grid	SS	
53	2	1094	0.00	0.00	0.066	22.4	284	340.0	S822+B1	0.25	0.25	no grid	SS	
53	2	1095	10.00	4.42	0.066	22.5	284	340.5	S822+B1	0.25	0.25	no grid	SS	
53	2	1096	17.99	7.94	0.067	22.5	284	336.3	S822+B1	0.25	0.25	no grid	SS	
53	3	1097	0.01	0.00	0.094	32.0	285	340.4	S822+B1	0.25	0.25	no grid	SS	
53	3	1098	10.01	4.42	0.095	32.0	285	337.3	S822+B1	0.25	0.25	no grid	SS	
53	3	1099	18.01	7.95	0.095	32.1	285	338.2	S822+B1	0.25	0.25	no grid	SS	
53	4	1100	0.01	0.00	0.141	47.9	289	339.7	S822+B1	0.25	0.25	no grid	SS	
53	4	1101	10.01	4.42	0.141	48.0	289	340.1	S822+B1	0.25	0.25	no grid	SS	
53	4	1102	17.99	7.94	0.141	48.1	289	341.3	S822+B1	0.25	0.25	no grid	SS	
53	5	1103	0.00	0.00	0.186	63.9	295	343.5	S822+B1	0.25	0.25	no grid	SS	
53	5	1104	10.02	4.42	0.186	64.0	296	343.9	S822+B1	0.25	0.25	no grid	SS	
53	5	1105	18.01	7.95	0.186	64.2	296	345.2	S822+B1	0.25	0.25	no grid	SS	
55	1	1124	0.00	0.00	0.038	12.8	284	336.3	FX63-137	0.25	0.25	no grid	SS	
55	1	1125	9.99	4.41	0.038	12.8	284	336.3	FX63-137	0.25	0.25	no grid	SS	
55	1	1126	18.01	7.95	0.038	12.8	284	337.6	FX63-137	0.25	0.25	no grid	SS	
55	2	1127	0.00	0.00	0.066	22.4	284	339.4	FX63-137	0.25	0.25	no grid	SS	
55	2	1128	10.01	4.42	0.066	22.4	284	339.4	FX63-137	0.25	0.25	no grid	SS	
55	2	1129	18.00	7.95	0.066	22.5	284	340.6	FX63-137	0.25	0.25	no grid	SS	
55	3	1130	0.01	0.00	0.094	32.0	285	340.3	FX63-137	0.25	0.25	no grid	SS	
55	3	1131	10.01	4.42	0.094	32.0	286	340.5	FX63-137	0.25	0.25	no grid	SS	
55	3	1132	18.01	7.95	0.095	32.1	286	337.6	FX63-137	0.25	0.25	no grid	SS	
55	4	1133	0.00	0.00	0.141	47.9	289	340.0	FX63-137	0.25	0.25	no grid	SS	
55	4	1134	10.00	4.42	0.141	48.0	289	340.4	FX63-137	0.25	0.25	no grid	SS	
55	4	1135	18.01	7.95	0.141	48.2	290	341.7	FX63-137	0.25	0.25	no grid	SS	
56	1	1138	-0.01	0.00	0.038	12.8	285	337.4	FX63-137	0.25	0.25	grid	SS	
56	1	1139	10.00	4.42	0.038	12.8	284	337.1	FX63-137	0.25	0.25	grid	SS	
56	1	1140	17.99	7.94	0.038	12.8	284	337.1	FX63-137	0.25	0.25	grid	SS	
56	2	1141	0.00	0.00	0.066	22.4	284	339.8	FX63-137	0.25	0.25	grid	SS	
56	2	1142	10.00	4.42	0.066	22.4	284	339.8	FX63-137	0.25	0.25	grid	SS	
56	2	1143	18.00	7.95	0.066	22.5	284	340.2	FX63-137	0.25	0.25	grid	SS	
56	3	1144	0.00	0.00	0.094	32.0	285	340.5	FX63-137	0.25	0.25	grid	SS	
56	3	1145	10.00	4.42	0.094	32.0	285	340.5	FX63-137	0.25	0.25	grid	SS	
56	3	1146	18.00	7.95	0.095	32.1	285	337.4	FX63-137	0.25	0.25	grid	SS	
56	4	1147	0.01	0.00	0.141	47.9	288	339.9	FX63-137	0.25	0.25	grid	SS	
56	4	1148	10.01	4.42	0.141	48.0	289	340.1	FX63-137	0.25	0.25	grid	SS	
56	4	1149	17.99	7.94	0.141	48.0	289	340.7	FX63-137	0.25	0.25	grid	SS	
59	1	1184	0.00	0.00	0.038	12.8	284	336.8	FX63-137	0	0	grid	SS	
59	1	1185	10.00	4.42	0.038	12.8	284	337.6	FX63-137	0	0	grid	SS	
59	1	1186	18.00	7.95	0.038	12.8	284	337.6	FX63-137	0	0	grid	SS	
59	2	1187	-0.01	0.00	0.066	22.4	284	339.7	FX63-137	0	0	grid	SS	
59	2	1188	10.00	4.42	0.066	22.4	284	339.8	FX63-137	0	0	grid	SS	
59	2	1189	18.01	7.95	0.066	22.5	284	340.2	FX63-137	0	0	grid	SS	
59	3	1190	0.00	0.00	0.095	32.0	285	337.3	FX63-137	0	0	grid	SS	
59	3	1191	10.00	4.42	0.095	32.1	285	337.5	FX63-137	0	0	grid	SS	
59	3	1192	18.00	7.95	0.095	32.1	285	337.7	FX63-137	0	0	grid	SS	
59	4	1193	0.01	0.00	0.141	48.0	288	340.1	FX63-137	0	0	grid	SS	
59	4	1194	10.00	4.42	0.141	48.0	288	340.6	FX63-137	0	0	grid	SS	
59	4	1195	17.99	7.94	0.141	48.1	289	341.2	FX63-137	0	0	grid	SS	

Run	Polar	DPN	$\alpha$	$\alpha_{eff}$	M	V	Ttot	C	Airfoil	Trip SS	Trip PS	Grid	Array	Info
60	1	1198	0.00	0.00	0.038	12.8	284	337.6	FX63-137	0	0	no grid	SS	
60	1	1199	10.01	4.42	0.038	12.8	284	337.6	FX63-137	0	0	no grid	SS	
60	1	1200	18.01	7.95	0.038	12.8	284	337.6	FX63-137	0	0	no grid	SS	
60	2	1201	0.00	0.00	0.066	22.4	284	338.8	FX63-137	0	0	no grid	SS	
60	2	1202	9.99	4.41	0.066	22.4	284	339.2	FX63-137	0	0	no grid	SS	
60	2	1203	18.01	7.95	0.066	22.5	284	340.2	FX63-137	0	0	no grid	SS	
60	3	1204	-0.01	0.00	0.094	32.0	286	340.6	FX63-137	0	0	no grid	SS	
60	3	1205	10.00	4.42	0.095	32.0	286	337.3	FX63-137	0	0	no grid	SS	
60	3	1206	18.00	7.95	0.095	32.1	286	338.3	FX63-137	0	0	no grid	SS	
60	4	1207	0.00	0.00	0.141	47.9	289	339.9	FX63-137	0	0	no grid	SS	
60	4	1208	10.00	4.42	0.141	48.0	289	340.3	FX63-137	0	0	no grid	SS	
60	4	1209	18.00	7.95	0.141	48.2	290	341.6	FX63-137	0	0	no grid	SS	
63	1	1244	0.00	0.00	0.094	32.0	285	340.2	S822+B4	0.25	0.25	no grid	SS	
63	1	1245	9.99	4.41	0.094	32.0	285	340.6	S822+B4	0.25	0.25	no grid	SS	
63	1	1246	18.01	7.95	0.095	32.1	285	338.1	S822+B4	0.25	0.25	no grid	SS	
63	2	1247	0.00	0.00	0.141	48.0	288	340.1	S822+B4	0.25	0.25	no grid	SS	
63	2	1248	10.01	4.42	0.141	48.1	289	340.8	S822+B4	0.25	0.25	no grid	SS	
63	2	1249	18.00	7.95	0.142	48.2	289	339.6	S822+B4	0.25	0.25	no grid	SS	
63	3	1250	0.01	0.00	0.187	64.1	294	342.6	S822+B4	0.25	0.25	no grid	SS	
63	3	1251	10.00	4.42	0.187	64.3	295	343.7	S822+B4	0.25	0.25	no grid	SS	
63	3	1252	18.00	7.95	0.188	64.5	296	343.1	S822+B4	0.25	0.25	no grid	SS	
65	1	1271	0.00	0.00	0.067	22.8	283	339.9	SG6043	0.25	0.25	no grid	SS	
65	1	1272	4.99	2.20	0.067	22.8	283	340.3	SG6043	0.25	0.25	no grid	SS	
65	1	1273	10.00	4.42	0.067	22.8	283	340.1	SG6043	0.25	0.25	no grid	SS	
65	2	1274	-0.01	0.00	0.038	12.8	283	337.1	SG6043	0.25	0.25	no grid	SS	
65	2	1275	5.00	2.21	0.038	12.8	283	337.1	SG6043	0.25	0.25	no grid	SS	
65	2	1276	10.00	4.42	0.038	12.8	283	337.1	SG6043	0.25	0.25	no grid	SS	
65	3	1277	0.00	0.00	0.066	22.4	283	339.5	SG6043	0.25	0.25	no grid	SS	
65	3	1278	4.99	2.20	0.066	22.4	283	339.2	SG6043	0.25	0.25	no grid	SS	
65	3	1279	10.00	4.42	0.066	22.4	283	339.2	SG6043	0.25	0.25	no grid	SS	
65	4	1280	-0.01	0.00	0.095	32.0	284	337.2	SG6043	0.25	0.25	no grid	SS	
65	4	1281	4.99	2.20	0.095	32.0	284	336.9	SG6043	0.25	0.25	no grid	SS	
65	4	1282	10.00	4.42	0.095	32.0	284	336.9	SG6043	0.25	0.25	no grid	SS	
66	1	1285	-0.01	0.00	0.038	12.8	283	336.6	SG6043	0.25	0.25	grid	SS	
66	1	1286	5.00	2.21	0.038	12.8	283	335.8	SG6043	0.25	0.25	grid	SS	
66	1	1287	10.01	4.42	0.038	12.8	283	336.6	SG6043	0.25	0.25	grid	SS	
66	2	1288	0.01	0.00	0.066	22.4	283	339.7	SG6043	0.25	0.25	grid	SS	
66	2	1289	4.99	2.20	0.066	22.4	283	339.2	SG6043	0.25	0.25	grid	SS	
66	2	1290	10.01	4.42	0.066	22.4	283	339.5	SG6043	0.25	0.25	grid	SS	
66	3	1291	0.00	0.00	0.095	32.0	284	337.3	SG6043	0.25	0.25	grid	SS	
66	3	1292	5.00	2.21	0.095	32.0	284	337.3	SG6043	0.25	0.25	grid	SS	
66	3	1293	10.00	4.42	0.095	32.1	284	337.5	SG6043	0.25	0.25	grid	SS	
66	4	1294	-0.01	0.00	0.02	6.9	283	345.5	SG6043	0.25	0.25	grid	SS	
66	4	1295	4.99	2.20	0.02	6.9	283	345.5	SG6043	0.25	0.25	grid	SS	
66	4	1296	9.99	4.41	0.02	6.9	283	345.5	SG6043	0.25	0.25	grid	SS	
67	1	1299	0.00	0.00	0.021	7.0	283	332.4	SG6043	0.25	0.25	no grid	SS	
67	1	1300	5.00	2.21	0.021	7.0	283	332.4	SG6043	0.25	0.25	no grid	SS	
67	1	1301	9.99	4.41	0.021	7.0	283	332.4	SG6043	0.25	0.25	no grid	SS	
70	1	1337	0.00	0.00	0.095	32.0	284	336.6	SG6043	0	0	grid	SS	
70	1	1338	10.01	4.42	0.095	32.0	284	336.8	SG6043	0	0	grid	SS	

Run	Polar	DPN	$\alpha$	$\alpha_{eff}$	M	V	Ttot	C	Airfoil	Trip SS	Trip PS	Grid	Array	Info
70	1	1339	18.00	7.95	0.095	32.0	284	336.9	SG6043	0	0	grid	SS	
71	1	1342	0.00	0.00	0.021	7.1	283	337.1	SG6043	0	0	no grid	SS	
71	1	1343	10.00	4.42	0.021	7.0	283	332.9	SG6043	0	0	no grid	SS	
71	1	1344	18.00	7.95	0.021	7.0	283	332.9	SG6043	0	0	no grid	SS	
71	2	1345	0.00	0.00	0.038	12.8	283	337.4	SG6043	0	0	no grid	SS	
71	2	1346	10.00	4.42	0.038	12.8	283	337.4	SG6043	0	0	no grid	SS	
71	2	1347	17.99	7.94	0.038	12.9	283	338.7	SG6043	0	0	no grid	SS	
71	3	1348	0.01	0.00	0.066	22.4	283	339.5	SG6043	0	0	no grid	SS	
71	3	1349	10.00	4.42	0.066	22.4	283	339.7	SG6043	0	0	no grid	SS	
71	3	1350	18.01	7.95	0.067	22.5	283	335.4	SG6043	0	0	no grid	SS	
71	4	1351	0.00	0.00	0.095	32.0	284	337.1	SG6043	0	0	no grid	SS	
71	4	1352	10.00	4.42	0.095	32.0	284	336.8	SG6043	0	0	no grid	SS	
71	4	1353	18.01	7.95	0.095	32.1	285	337.8	SG6043	0	0	no grid	SS	
74	1	1389	0.00	0.00	0.095	32.1	284	337.7	S822+A1	0.25	0.25	no grid	SS	
74	1	1390	9.99	4.41	0.095	32.1	285	338.2	S822+A1	0.25	0.25	no grid	SS	
74	1	1391	18.00	7.95	0.095	32.2	285	339.3	S822+A1	0.25	0.25	no grid	SS	
74	2	1392	0.00	0.00	0.141	48.0	288	340.1	S822+A1	0.25	0.25	no grid	SS	
74	2	1393	10.00	4.42	0.141	48.1	288	340.8	S822+A1	0.25	0.25	no grid	SS	
74	2	1394	18.00	7.95	0.142	48.2	288	339.5	S822+A1	0.25	0.25	no grid	SS	
74	3	1395	0.00	0.00	0.186	64.0	294	343.8	S822+A1	0.25	0.25	no grid	SS	
74	3	1396	10.00	4.42	0.187	64.1	294	342.9	S822+A1	0.25	0.25	no grid	SS	
74	3	1397	17.99	7.94	0.187	64.4	295	344.2	S822+A1	0.25	0.25	no grid	SS	
76	1	1416	0.00	0.00	0.095	32.1	285	337.6	SH3055	0.25	0.25	no grid	SS	
76	1	1417	10.00	4.42	0.095	32.1	285	338.1	SH3055	0.25	0.25	no grid	SS	
76	1	1418	18.00	7.95	0.095	32.2	285	338.7	SH3055	0.25	0.25	no grid	SS	
76	2	1419	0.00	0.00	0.141	48.1	288	340.9	SH3055	0.25	0.25	no grid	SS	
76	2	1420	9.99	4.41	0.141	48.0	289	340.3	SH3055	0.25	0.25	no grid	SS	
76	2	1421	18.01	7.95	0.141	48.1	289	341.2	SH3055	0.25	0.25	no grid	SS	
76	3	1422	0.01	0.00	0.186	64.0	295	343.8	SH3055	0.25	0.25	no grid	SS	
76	3	1423	10.01	4.42	0.186	64.0	295	344.2	SH3055	0.25	0.25	no grid	SS	
76	3	1424	18.01	7.95	0.187	64.2	295	343.3	SH3055	0.25	0.25	no grid	SS	
77	1	1427	0.00	0.00	0.094	32.0	286	340.7	SH3055	0.25	0.25	grid	SS	
77	1	1428	9.99	4.41	0.094	32.0	286	340.5	SH3055	0.25	0.25	grid	SS	
77	1	1429	18.01	7.95	0.095	32.0	286	337.3	SH3055	0.25	0.25	grid	SS	
77	2	1430	0.01	0.00	0.186	64.0	294	343.9	SH3055	0.25	0.25	grid	SS	
77	2	1431	10.01	4.42	0.187	64.0	294	342.5	SH3055	0.25	0.25	grid	SS	
77	2	1432	18.01	7.95	0.187	64.2	295	343.2	SH3055	0.25	0.25	grid	SS	
82	1	1477	0.00	0.00	0.095	32.0	285	336.9	SH3055	0	0	grid	SS	
82	1	1478	9.99	4.41	0.095	32.0	285	337.1	SH3055	0	0	grid	SS	
82	1	1479	18.01	7.95	0.095	32.0	285	337.3	SH3055	0	0	grid	SS	
82	2	1480	0.00	0.00	0.187	64.0	293	342.1	SH3055	0	0	grid	SS	
82	2	1481	9.99	4.41	0.187	64.1	294	342.6	SH3055	0	0	grid	SS	
82	2	1482	17.99	7.94	0.187	64.2	294	343.2	SH3055	0	0	grid	SS	
83	1	1485	-0.01	0.00	0.095	32.1	283	337.4	SH3055	0	0	no grid	SS	
83	1	1486	-0.01	0.00	0.095	32.1	283	337.5	SH3055	0	0	no grid	SS	
83	1	1487	9.99	4.41	0.095	32.1	283	337.5	SH3055	0	0	no grid	SS	
83	1	1488	17.99	7.94	0.095	32.1	283	338.1	SH3055	0	0	no grid	SS	
83	2	1489	0.00	0.00	0.142	48.0	285	337.7	SH3055	0	0	no grid	SS	
83	2	1490	10.01	4.42	0.142	48.0	285	338.2	SH3055	0	0	no grid	SS	
83	2	1491	18.00	7.95	0.142	48.2	286	339.2	SH3055	0	0	no grid	SS	

Run	Polar	DPN	$\alpha$	$\alpha_{eff}$	M	V	Ttot	C	Airfoil	Trip SS	Trip PS	Grid	Array	Info
83	3	1492	0.00	0.00	0.187	64.0	291	342.0	SH3055	0	0	no grid	SS	
83	3	1493	10.01	4.42	0.188	64.0	291	340.6	SH3055	0	0	no grid	SS	
83	3	1494	18.01	7.95	0.188	64.2	292	341.4	SH3055	0	0	no grid	SS	
86	1	1529	0.00	0.00	0.095	32.0	284	336.9	S822+A4	0.25	0.25	no grid	SS	
86	1	1530	10.00	4.42	0.095	32.1	284	337.4	S822+A4	0.25	0.25	no grid	SS	
86	1	1531	18.01	7.95	0.095	32.2	284	338.4	S822+A4	0.25	0.25	no grid	SS	
86	2	1532	0.00	0.00	0.141	47.9	287	339.7	S822+A4	0.25	0.25	no grid	SS	
86	2	1533	10.00	4.42	0.141	48.0	287	340.1	S822+A4	0.25	0.25	no grid	SS	
86	2	1534	18.00	7.95	0.142	48.1	287	338.8	S822+A4	0.25	0.25	no grid	SS	
86	3	1535	0.00	0.00	0.187	63.9	293	341.9	S822+A4	0.25	0.25	no grid	SS	
86	3	1536	10.00	4.42	0.187	64.1	294	342.7	S822+A4	0.25	0.25	no grid	SS	
86	3	1537	18.00	7.95	0.188	64.3	294	342.1	S822+A4	0.25	0.25	no grid	SS	
88	1	1556	0.00	0.00	0.038	12.8	283	335.8	SD2030	0.25	0.25	no grid	SS	
88	1	1557	10.00	4.42	0.038	12.8	283	335.8	SD2030	0.25	0.25	no grid	SS	
88	1	1558	18.00	7.95	0.038	12.8	283	337.1	SD2030	0.25	0.25	no grid	SS	
88	2	1559	0.00	0.00	0.066	22.4	283	339.2	SD2030	0.25	0.25	no grid	SS	
88	2	1560	10.01	4.42	0.066	22.4	283	339.2	SD2030	0.25	0.25	no grid	SS	
88	2	1561	18.00	7.95	0.067	22.5	283	335.4	SD2030	0.25	0.25	no grid	SS	
88	3	1562	0.00	0.00	0.095	32.0	284	336.5	SD2030	0.25	0.25	no grid	SS	
88	3	1563	10.00	4.42	0.095	32.0	284	336.8	SD2030	0.25	0.25	no grid	SS	
88	3	1564	18.01	7.95	0.095	32.1	284	337.7	SD2030	0.25	0.25	no grid	SS	
89	1	1567	0.00	0.00	0.038	12.8	283	336.1	SD2030	0.25	0.25	grid	SS	
89	1	1568	10.01	4.42	0.038	12.8	283	335.8	SD2030	0.25	0.25	grid	SS	
89	1	1569	18.00	7.95	0.038	12.8	283	335.8	SD2030	0.25	0.25	grid	SS	
89	2	1570	0.00	0.00	0.095	32.0	284	336.8	SD2030	0.25	0.25	grid	SS	
89	2	1571	9.99	4.41	0.095	32.0	284	336.7	SD2030	0.25	0.25	grid	SS	
89	2	1572	18.00	7.95	0.095	32.0	284	337.2	SD2030	0.25	0.25	grid	SS	
92	1	1607	0.00	0.00	0.038	12.8	283	336.8	SD2030	0	0	grid	SS	
92	1	1608	5.00	2.21	0.038	12.8	283	337.6	SD2030	0	0	grid	SS	
92	1	1609	10.00	4.42	0.038	12.9	283	338.4	SD2030	0	0	grid	SS	
92	2	1610	0.00	0.00	0.095	32.1	284	337.6	SD2030	0	0	grid	SS	
92	2	1611	5.00	2.21	0.095	32.1	284	337.6	SD2030	0	0	grid	SS	
92	2	1612	10.01	4.42	0.095	32.1	284	337.8	SD2030	0	0	grid	SS	
93	1	1615	0.00	0.00	0.038	12.8	283	337.1	SD2030	0	0	no grid	SS	
93	1	1616	5.00	2.21	0.038	12.8	283	337.1	SD2030	0	0	no grid	SS	
93	1	1617	10.00	4.42	0.038	12.9	283	338.4	SD2030	0	0	no grid	SS	
93	2	1618	0.00	0.00	0.066	22.4	283	339.2	SD2030	0	0	no grid	SS	
93	2	1619	5.00	2.21	0.066	22.4	284	338.8	SD2030	0	0	no grid	SS	
93	2	1620	10.00	4.42	0.066	22.4	284	339.2	SD2030	0	0	no grid	SS	
93	3	1621	0.00	0.00	0.095	32.0	285	336.9	SD2030	0	0	no grid	SS	
93	3	1622	5.01	2.21	0.095	32.0	285	337.1	SD2030	0	0	no grid	SS	
93	3	1623	10.00	4.42	0.095	32.1	285	337.7	SD2030	0	0	no grid	SS	
95	1	1642	0.00	0.00	0.02	6.9	283	346.0	background	0	0	no grid	SS	
95	1	1643	0.00	0.00	0.038	12.8	283	337.1	background	0	0	no grid	SS	
95	1	1644	0.00	0.00	0.066	22.5	284	340.2	background	0	0	no grid	SS	
95	1	1645	0.00	0.00	0.094	31.7	285	337.7	background	0	0	no grid	SS	
95	1	1646	0.00	0.00	0.095	32.0	285	336.8	background	0	0	no grid	SS	
95	1	1647	0.00	0.00	0.117	39.6	286	338.3	background	0	0	no grid	SS	
95	1	1648	0.00	0.00	0.141	48.0	288	340.2	background	0	0	no grid	SS	
95	1	1649	0.00	0.00	0.163	55.6	291	341.2	background	0	0	no grid	SS	
95	1	1650	0.00	0.00	0.186	64.0	295	343.9	background	0	0	no grid	SS	

Run	Polar	DPN	$\alpha$	$\alpha_{eff}$	M	V	Ttot	C	Airfoil	Trip SS	Trip PS	Grid	Array	Info
95	1	1651	0.00	0.00	0.206	71.3	299	346.0	background	0	0	no grid	SS	
96	1	1654	0.00	0.00	0.021	7.0	286	331.9	background	0	0	grid	SS	
96	1	1655	0.00	0.00	0.038	12.8	285	336.1	background	0	0	grid	SS	
96	1	1656	0.00	0.00	0.066	22.4	285	339.5	background	0	0	grid	SS	
96	1	1657	0.00	0.00	0.094	32.0	285	340.3	background	0	0	grid	SS	
96	1	1658	0.00	0.00	0.141	48.0	288	340.1	background	0	0	grid	SS	
96	1	1659	0.00	0.00	0.187	64.0	293	342.0	background	0	0	grid	SS	
97	1	1662	10.01	4.42	0.066	22.4	285	339.1	S834Special	0.5	0.5	no grid	SS	
97	2	1663	10.00	4.42	0.066			340.0	S834Special	0.25/0.25	0.25/0.25	no grid	SS	
97	2	1663	10.00	4.42	0.066	22.4	284	339.8	S834Special	0.25/0.25	0.25/0.25	no grid	SS	
97	3	1664	14.02	6.19	0.066	22.5	284	340.2	S834Special	0.25/0.25	0.25/0.25	no grid	SS	
97	3	1665	10.00	4.42	0.066	22.4	283	340.0	S834Special	0.25	0.25	no grid	SS	
97	3	1666	14.00	6.18	0.067	22.5	284	336.0	S834Special	0.25	0.25	no grid	SS	
97	4	1667	10.00	4.42	0.067	22.5	283	335.4	S834Special	0.25	0.5	no grid	SS	
98	1	1670	0.00	0.00	0.066	22.3	282	338.5	S834Special	0	0.5	no grid	SS	
98	1	1671	10.00	4.42	0.066	22.4	282	338.8	S834Special	0	0.5	no grid	SS	
98	1	1672	14.01	6.19	0.066	22.4	282	338.8	S834Special	0	0.5	no grid	SS	
98	1	1673	18.00	7.95	0.066	22.4	282	339.2	S834Special	0	0.5	no grid	SS	
98	2	1674	0.00	0.00	0.067	22.4	282	334.5	S834Special	0	0.45	no grid	SS	
98	2	1675	10.00	4.42	0.067	22.4	282	334.9	S834Special	0	0.45	no grid	SS	
98	2	1676	14.01	6.19	0.067	22.5	282	335.2	S834Special	0	0.45	no grid	SS	
98	2	1677	18.00	7.95	0.067	22.5	282	335.7	S834Special	0	0.45	no grid	SS	
98	3	1678	0.00	0.00	0.067	22.4	282	334.3	S834Special	0	0.3	no grid	SS	
98	3	1679	10.00	4.42	0.067	22.4	282	334.8	S834Special	0	0.3	no grid	SS	
98	3	1680	14.00	6.18	0.067	22.4	282	334.8	S834Special	0	0.3	no grid	SS	
98	3	1681	18.00	7.95	0.067	22.5	282	335.2	S834Special	0	0.3	no grid	SS	
99	1	1684	0.01	0.00	0.067	22.4	282	334.5	S834Special	0.3	0.3	no grid	SS	
99	1	1685	10.00	4.42	0.067	22.4	282	334.5	S834Special	0.3	0.3	no grid	SS	
99	1	1686	18.01	7.95	0.067	22.5	282	335.4	S834Special	0.3	0.3	no grid	SS	
99	2	1687	0.01	0.00	0.095	32.1	283	337.5	S834Special	0.3	0.3	no grid	SS	
99	2	1688	10.00	4.42	0.095	32.1	283	337.8	S834Special	0.3	0.3	no grid	SS	
99	2	1689	18.00	7.95	0.095	32.2	283	338.4	S834Special	0.3	0.3	no grid	SS	
100	1	1692	4.52	2.00	0.094	31.7	283	337.3	NACA0012	0.25	0.25	no grid	SS	
100	1	1693	9.06	4.00	0.094	31.7	284	337.6	NACA0012	0.25	0.25	no grid	SS	
100	1	1694	12.00	5.30	0.094	31.8	284	338.0	NACA0012	0.25	0.25	no grid	SS	
100	1	1695	16.54	7.30	0.094	31.8	284	338.5	NACA0012	0.25	0.25	no grid	SS	
100	2	1696	4.53	2.00	0.117	39.6	285	338.3	NACA0012	0.25	0.25	no grid	SS	
100	2	1697	9.06	4.00	0.117	39.6	285	338.6	NACA0012	0.25	0.25	no grid	SS	
100	2	1698	11.99	5.29	0.117	39.7	285	339.0	NACA0012	0.25	0.25	no grid	SS	
100	2	1699	16.54	7.30	0.117	39.7	285	339.7	NACA0012	0.25	0.25	no grid	SS	
100	3	1700	4.53	2.00	0.163	55.6	290	340.9	NACA0012	0.25	0.25	no grid	SS	
100	3	1701	9.06	4.00	0.163	55.6	290	341.2	NACA0012	0.25	0.25	no grid	SS	
100	3	1702	12.00	5.30	0.163	55.7	290	341.6	NACA0012	0.25	0.25	no grid	SS	
100	3	1703	16.54	7.30	0.163	55.8	291	342.2	NACA0012	0.25	0.25	no grid	SS	
100	4	1704	4.53	2.00	0.207	71.4	298	344.7	NACA0012	0.25	0.25	no grid	SS	
100	4	1705	9.06	4.00	0.207	71.5	298	345.3	NACA0012	0.25	0.25	no grid	SS	
100	4	1706	11.99	5.29	0.207	71.6	299	345.8	NACA0012	0.25	0.25	no grid	SS	
100	4	1707	16.54	7.30	0.208	71.7	299	344.8	NACA0012	0.25	0.25	no grid	SS	
101	1	1710	4.53	2.00	0.094	31.7	286	337.4	NACA0012	0	0	no grid	SS	
101	1	1711	9.06	4.00	0.094	31.8	286	337.8	NACA0012	0	0	no grid	SS	
101	1	1712	12.00	5.30	0.094	31.8	285	337.8	NACA0012	0	0	no grid	SS	

Run	Polar	DPN	$\alpha$	$\alpha_{eff}$	M	V	Ttot	C	Airfoil	Trip SS	Trip PS	Grid	Array	Info
101	1	1713	16.54	7.30	0.094	31.8	285	338.3	NACA0012	0	0	no grid	SS	
101	2	1714	4.53	2.00	0.117	39.6	286	338.3	NACA0012	0	0	no grid	SS	
101	2	1715	9.06	4.00	0.117	39.6	286	338.5	NACA0012	0	0	no grid	SS	
101	2	1716	12.00	5.30	0.117	39.6	286	338.6	NACA0012	0	0	no grid	SS	
101	2	1717	16.53	7.30	0.117	39.7	286	339.3	NACA0012	0	0	no grid	SS	
101	3	1718	4.53	2.00	0.163	55.5	291	340.7	NACA0012	0	0	no grid	SS	
101	3	1719	9.06	4.00	0.163	55.6	291	341.0	NACA0012	0	0	no grid	SS	
101	3	1720	12.00	5.30	0.163	55.7	291	341.5	NACA0012	0	0	no grid	SS	
101	3	1721	16.53	7.30	0.163	55.8	291	342.1	NACA0012	0	0	no grid	SS	
101	4	1722	4.53	2.00	0.207	71.3	298	344.6	NACA0012	0	0	no grid	SS	
101	4	1723	9.06	4.00	0.207	71.4	299	345.0	NACA0012	0	0	no grid	SS	
101	4	1724	12.00	5.30	0.207	71.6	299	345.8	NACA0012	0	0	no grid	SS	
101	4	1725	16.54	7.30	0.207	71.7	299	346.4	NACA0012	0	0	no grid	SS	
102	1	1728	0.00	0.00	0.066	22.4	284	339.2	SG6043	0.5	0.5	no grid	SS	
102	1	1729	5.01	2.21	0.066	22.4	284	338.8	SG6043	0.5	0.5	no grid	SS	
102	1	1730	9.99	4.41	0.066	22.4	284	339.4	SG6043	0.5	0.5	no grid	SS	
103	1	1733	0.01	0.00	0.066	22.4	284	339.2	SD2030	0.5	0.5	no grid	SS	
103	1	1734	5.00	2.21	0.066	22.4	284	339.7	SD2030	0.5	0.5	no grid	SS	
103	1	1735	10.00	4.42	0.066	22.4	284	339.5	SD2030	0.5	0.5	no grid	SS	
104	1	1738	0.00	0.00	0.066	22.4	283	339.5	S822	0.5	0.5	no grid	SS	
104	1	1739	10.00	4.42	0.066	22.4	283	340.0	S822	0.5	0.5	no grid	SS	
104	1	1740	14.00	6.18	0.066	22.5	283	340.3	S822	0.5	0.5	no grid	SS	
104	1	1741	17.99	7.94	0.067	22.5	283	335.7	S822	0.5	0.5	no grid	SS	
105	1	1744	0.00	0.00	0.066	22.4	283	339.8	FX63-137	0.5	0.5	no grid	SS	
105	1	1745	9.99	4.41	0.066	22.4	283	339.8	FX63-137	0.5	0.5	no grid	SS	
105	1	1746	14.00	6.18	0.067	22.5	283	335.7	FX63-137	0.5	0.5	no grid	SS	
105	1	1747	18.01	7.95	0.067	22.5	283	336.4	FX63-137	0.5	0.5	no grid	SS	
106	1	1750	10.01	4.42	0.066	22.4	283	339.8	FX63-137	0.5	0.5	no grid	SS	+plasticine
106	1	1751	13.99	6.18	0.066	22.4	282	339.5	FX63-137	0.5	0.5	no grid	SS	+plasticine
106	1	1752	18.00	7.95	0.067	22.5	282	335.2	FX63-137	0.5	0.5	no grid	SS	+plasticine
106	2	1753	10.00	4.42	0.095	32.0	282	336.8	FX63-137	0.5	0.5	no grid	SS	+plasticine
106	2	1754	14.00	6.18	0.095	32.0	282	337.1	FX63-137	0.5	0.5	no grid	SS	+plasticine
106	2	1755	18.00	7.95	0.095	32.1	282	337.7	FX63-137	0.5	0.5	no grid	SS	+plasticine
107	1	1758	10.00	4.42	0.066	22.3	282	338.2	FX63-137	0.5	0.5	no grid	SS	+tape teeth
107	1	1759	14.00	6.18	0.066	22.4	282	338.9	FX63-137	0.5	0.5	no grid	SS	+tape teeth
107	1	1760	18.00	7.95	0.066	22.4	281	339.2	FX63-137	0.5	0.5	no grid	SS	+tape teeth
107	2	1761	10.00	4.42	0.095	32.1	282	337.4	FX63-137	0.5	0.5	no grid	SS	+tape teeth
107	2	1762	14.00	6.18	0.095	32.1	282	337.6	FX63-137	0.5	0.5	no grid	SS	+tape teeth
107	2	1763	18.00	7.95	0.095	32.1	282	338.0	FX63-137	0.5	0.5	no grid	SS	+tape teeth
108	1	1766	14.00	6.18	0.067	22.5	282	335.7	FX63-137	0.5	0.5	no grid	SS	+foam
108	2	1767	14.00	6.18	0.095	32.1	282	338.3	FX63-137	0.5	0.5	no grid	SS	+foam
109	1	1770	14.00	6.18	0.066	22.4	282	338.6	FX63-137	0.5	0.5	no grid	SS	+foam +plasticine
109	2	1771	14.00	6.18	0.095	32.0	282	336.9	FX63-137	0.5	0.5	no grid	SS	+foam +plasticine
110	1	1774	0.00	0.00	0.066	22.4	282	338.6	SG6043	0.5	0.25	no grid	SS	
110	1	1775	10.00	4.42	0.066	22.4	282	338.6	SG6043	0.5	0.25	no grid	SS	
110	1	1776	14.00	6.18	0.066	22.4	282	338.6	SG6043	0.5	0.25	no grid	SS	
110	1	1777	18.00	7.95	0.066	22.4	282	339.1	SG6043	0.5	0.25	no grid	SS	
110	2	1778	0.00	0.00	0.066	22.4	282	339.2	SG6043	0.5	0	no grid	SS	
110	2	1779	10.00	4.42	0.066	22.4	282	339.2	SG6043	0.5	0	no grid	SS	

Run	Polar	DPN	$\alpha$	$\alpha_{eff}$	M	V	Ttot	C	Airfoil	Trip SS	Trip PS	Grid	Array	Info
110	2	1780	14.00	6.18	0.067	22.4	282	334.9	SG6043	0.5	0	no grid	SS	
110	2	1781	18.00	7.95	0.067	22.5	282	335.4	SG6043	0.5	0	no grid	SS	
111	1	1784	5.00	2.21	0.066	22.4	282	338.9	SG6043	0.5	0	no grid	SS	
111	2	1785	5.00	2.21	0.066	22.4	282	338.9	SG6043	0.5	0.25	no grid	SS	
112	1	1788	14.00	6.18	0.066	22.4	284	338.8	FX63-137	0.5	0.5	no grid	SS	+foam
112	2	1789	14.00	6.18	0.095	32.0	284	336.9	FX63-137	0.5	0.5	no grid	SS	+foam
113	1	1792	0.00	0.00	0.094	31.9	285	339.8	FX63-137	0	0	no grid	PS	
113	1	1793	10.00	4.42	0.094	32.0	285	340.0	FX63-137	0	0	no grid	PS	
113	1	1794	18.00	7.95	0.095	32.1	285	337.5	FX63-137	0	0	no grid	PS	
114	1	1797	0.00	0.00	0.095	32.0	285	337.2	S822+B1	0.25	0.25	no grid	PS	
114	1	1798	10.00	4.42	0.095	32.1	285	337.6	S822+B1	0.25	0.25	no grid	PS	
114	1	1799	18.00	7.95	0.095	32.2	285	338.8	S822+B1	0.25	0.25	no grid	PS	
114	2	1800	0.01	0.00	0.141	47.9	287	339.7	S822+B1	0.25	0.25	no grid	PS	
114	2	1801	10.00	4.42	0.141	48.0	288	340.4	S822+B1	0.25	0.25	no grid	PS	
114	2	1802	18.00	7.95	0.142	48.2	288	339.3	S822+B1	0.25	0.25	no grid	PS	
114	3	1803	0.00	0.00	0.186	64.0	294	343.8	S822+B1	0.25	0.25	no grid	PS	
114	3	1804	10.00	4.42	0.187	64.1	294	342.6	S822+B1	0.25	0.25	no grid	PS	
114	3	1805	18.00	7.95	0.187	64.4	294	344.1	S822+B1	0.25	0.25	no grid	PS	
115	1	1808	0.00	0.00	0.187	64.0	292	342.2	S822+B1	0.25	0.25	grid	PS	
115	1	1809	10.01	4.42	0.188	64.3	293	342.0	S822+B1	0.25	0.25	grid	PS	
115	1	1810	18.00	7.95	0.188	64.5	294	342.8	S822+B1	0.25	0.25	grid	PS	
116	1	1813	0.00	0.00	0.186	63.9	294	343.4	S822+B4	0.25	0.25	grid	PS	
116	1	1814	10.00	4.42	0.187	64.0	294	342.2	S822+B4	0.25	0.25	grid	PS	
116	1	1815	18.00	7.95	0.187	64.2	294	343.1	S822+B4	0.25	0.25	grid	PS	
117	1	1818	0.00	0.00	0.094	32.0	286	340.2	S822+B4	0.25	0.25	no grid	PS	
117	1	1819	10.00	4.42	0.094	32.0	286	340.4	S822+B4	0.25	0.25	no grid	PS	
117	1	1820	17.99	7.94	0.095	32.1	286	337.8	S822+B4	0.25	0.25	no grid	PS	
117	2	1821	0.00	0.00	0.141	47.9	288	339.7	S822+B4	0.25	0.25	no grid	PS	
117	2	1822	9.99	4.41	0.141	48.0	289	340.1	S822+B4	0.25	0.25	no grid	PS	
117	2	1823	18.01	7.95	0.141	48.2	289	341.5	S822+B4	0.25	0.25	no grid	PS	
117	3	1824	0.00	0.00	0.186	63.9	294	343.8	S822+B4	0.25	0.25	no grid	PS	
117	3	1825	10.01	4.42	0.186	64.0	295	344.3	S822+B4	0.25	0.25	no grid	PS	
117	3	1826	17.99	7.94	0.187	64.3	295	343.6	S822+B4	0.25	0.25	no grid	PS	
118	1	1829	0.00	0.00	0.186	64.0	294	343.9	S822+B2	0.25	0.25	no grid	PS	
118	1	1830	10.01	4.42	0.186	64.1	295	344.4	S822+B2	0.25	0.25	no grid	PS	
118	1	1831	18.01	7.95	0.187	64.3	295	343.7	S822+B2	0.25	0.25	no grid	PS	
119	1	1834	0.00	0.00	0.187	64.1	294	342.6	S822+B3	0.25	0.25	no grid	PS	
119	1	1835	10.00	4.42	0.187	64.2	295	343.5	S822+B3	0.25	0.25	no grid	PS	
119	1	1836	18.01	7.95	0.188	64.6	295	343.4	S822+B3	0.25	0.25	no grid	PS	
120	1	1839	0.01	0.00	0.094	32.0	286	339.9	S822+A1	0.25	0.25	no grid	PS	
120	1	1840	9.99	4.41	0.094	31.9	286	339.7	S822+A1	0.25	0.25	no grid	PS	
120	1	1841	18.00	7.95	0.094	32.0	286	340.6	S822+A1	0.25	0.25	no grid	PS	
120	2	1842	0.00	0.00	0.141	47.9	288	339.9	S822+A1	0.25	0.25	no grid	PS	
120	2	1843	9.99	4.41	0.141	48.0	289	340.3	S822+A1	0.25	0.25	no grid	PS	
120	2	1844	18.01	7.95	0.141	48.1	289	341.3	S822+A1	0.25	0.25	no grid	PS	
120	3	1845	0.00	0.00	0.186	63.9	294	343.7	S822+A1	0.25	0.25	no grid	PS	
120	3	1846	10.00	4.42	0.187	64.1	295	342.6	S822+A1	0.25	0.25	no grid	PS	
120	3	1847	18.00	7.95	0.187	64.3	295	343.8	S822+A1	0.25	0.25	no grid	PS	

Run	Polar	DPN	$\alpha$	$\alpha_{eff}$	M	V	Ttot	C	Airfoil	Trip SS	Trip PS	Grid	Array	Info
121	1	1850	0.00	0.00	0.186	63.9	293	343.5	S822+A1	0.25	0.25	grid	PS	
121	1	1851	10.00	4.42	0.187	64.0	294	342.5	S822+A1	0.25	0.25	grid	PS	
121	1	1852	18.00	7.95	0.187	64.2	294	343.1	S822+A1	0.25	0.25	grid	PS	
122	1	1855	0.00	0.00	0.187	63.9	291	341.9	S822+A4	0.25	0.25	grid	PS	
122	1	1856	10.01	4.42	0.187	64.0	291	342.5	S822+A4	0.25	0.25	grid	PS	
122	1	1857	18.01	7.95	0.188	64.2	292	341.3	S822+A4	0.25	0.25	grid	PS	
123	1	1860	0.00	0.00	0.095	32.0	284	337.2	S822+A4	0.25	0.25	no grid	PS	
123	1	1861	10.00	4.42	0.095	32.1	284	337.4	S822+A4	0.25	0.25	no grid	PS	
123	1	1862	18.00	7.95	0.095	32.2	284	338.6	S822+A4	0.25	0.25	no grid	PS	
123	2	1863	0.00	0.00	0.141	47.8	286	339.1	S822+A4	0.25	0.25	no grid	PS	
123	2	1864	10.00	4.42	0.141	47.9	286	339.6	S822+A4	0.25	0.25	no grid	PS	
123	2	1865	18.00	7.95	0.142	48.0	287	338.1	S822+A4	0.25	0.25	no grid	PS	
123	3	1866	0.00	0.00	0.187	63.9	291	341.6	S822+A4	0.25	0.25	no grid	PS	
123	3	1867	10.00	4.42	0.187	64.0	292	342.1	S822+A4	0.25	0.25	no grid	PS	
123	3	1868	18.01	7.95	0.188	64.2	292	341.4	S822+A4	0.25	0.25	no grid	PS	
124	1	1871	0.00	0.00	0.187	63.9	292	341.9	S822+A2	0.25	0.25	no grid	PS	
124	1	1872	10.00	4.42	0.187	64.0	292	342.5	S822+A2	0.25	0.25	no grid	PS	
124	1	1873	17.99	7.94	0.188	64.3	293	341.8	S822+A2	0.25	0.25	no grid	PS	
125	1	1876	0.00	0.00	0.187	63.9	292	341.7	S822+A3	0.25	0.25	no grid	PS	
125	1	1877	10.00	4.42	0.187	64.0	292	342.4	S822+A3	0.25	0.25	no grid	PS	
125	1	1878	18.01	7.95	0.188	64.3	293	341.8	S822+A3	0.25	0.25	no grid	PS	
126	1	1881	0.00	0.00	0.187	63.9	291	341.9	S822	0.25	0.25	grid	PS	
126	1	1882	10.00	4.42	0.187	64.1	292	342.7	S822	0.25	0.25	grid	PS	
126	1	1883	17.99	7.94	0.188	64.3	292	341.8	S822	0.25	0.25	grid	PS	
127	1	1886	0.00	0.00	0.094	32.0	285	340.2	S822	0.25	0.25	no grid	PS	
127	1	1887	9.99	4.41	0.095	32.0	284	336.6	S822	0.25	0.25	no grid	PS	
127	1	1888	18.01	7.95	0.095	32.1	284	337.4	S822	0.25	0.25	no grid	PS	
127	2	1889	0.00	0.00	0.141	47.9	287	339.8	S822	0.25	0.25	no grid	PS	
127	2	1890	10.01	4.42	0.141	47.9	287	340.0	S822	0.25	0.25	no grid	PS	
127	2	1891	18.00	7.95	0.142	48.1	287	338.4	S822	0.25	0.25	no grid	PS	
127	3	1892	0.00	0.00	0.187	64.0	292	342.0	S822	0.25	0.25	no grid	PS	
127	3	1893	10.00	4.42	0.187	64.0	293	342.4	S822	0.25	0.25	no grid	PS	
127	3	1894	18.00	7.95	0.188	64.2	293	341.6	S822	0.25	0.25	no grid	PS	
128	1	1897	0.00	0.00	0.095	32.0	284	336.7	S822	0	0	no grid	PS	
128	1	1898	10.00	4.42	0.095	32.0	284	337.1	S822	0	0	no grid	PS	
128	1	1899	18.01	7.95	0.095	32.1	284	338.0	S822	0	0	no grid	PS	
128	2	1900	0.00	0.00	0.141	47.9	287	339.8	S822	0	0	no grid	PS	
128	2	1901	10.00	4.42	0.141	47.9	287	339.9	S822	0	0	no grid	PS	
128	2	1902	18.00	7.95	0.142	48.1	287	338.7	S822	0	0	no grid	PS	
129	1	1905	0.00	0.00	0.095	32.0	284	336.7	S834	0	0	no grid	PS	
129	1	1906	9.99	4.41	0.095	32.0	284	336.4	S834	0	0	no grid	PS	
129	1	1907	18.00	7.95	0.095	32.1	284	337.6	S834	0	0	no grid	PS	
130	1	1910	0.00	0.00	0.095	32.0	284	336.3	SG6043	0	0	no grid	PS	
130	1	1911	10.01	4.42	0.095	31.9	284	336.2	SG6043	0	0	no grid	PS	
130	1	1912	18.00	7.95	0.095	32.1	284	337.7	SG6043	0	0	no grid	PS	
131	1	1915	0.00	0.00	0.095	31.9	284	336.2	SH3055	0	0	no grid	PS	
131	1	1916	10.00	4.42	0.095	32.0	284	336.5	SH3055	0	0	no grid	PS	
131	1	1917	18.00	7.95	0.095	32.1	284	337.6	SH3055	0	0	no grid	PS	
132	1	1920	0.00	0.00	0.095	32.0	284	336.3	SD2030	0	0	no grid	PS	

Run	Polar	DPN	$\alpha$	$\alpha_{eff}$	M	V	Ttot	C	Airfoil	Trip SS	Trip PS	Grid	Array	Info
132	1	1921	5.00	2.21	0.094	31.9	284	339.5	SD2030	0	0	no grid	PS	
132	1	1922	10.00	4.42	0.095	32.0	284	336.3	SD2030	0	0	no grid	PS	
133	1	1925	0.00	0.00	0.117	39.6	285	338.5	NACA0012	0.25	0.25	no grid	PS	
133	1	1926	4.53	2.00	0.117	39.6	285	338.5	NACA0012	0.25	0.25	no grid	PS	
133	1	1927	9.06	4.00	0.117	39.6	285	338.6	NACA0012	0.25	0.25	no grid	PS	
133	1	1928	12.00	5.30	0.117	39.7	285	339.1	NACA0012	0.25	0.25	no grid	PS	
133	1	1929	16.54	7.30	0.117	39.8	285	339.7	NACA0012	0.25	0.25	no grid	PS	
133	2	1930	0.00	0.00	0.163	55.5	289	340.7	NACA0012	0.25	0.25	no grid	PS	
133	2	1931	4.54	2.00	0.163	55.6	290	340.9	NACA0012	0.25	0.25	no grid	PS	
133	2	1932	9.06	4.00	0.163	55.6	290	341.2	NACA0012	0.25	0.25	no grid	PS	
133	2	1933	12.00	5.30	0.163	55.7	290	341.4	NACA0012	0.25	0.25	no grid	PS	
133	2	1934	16.54	7.30	0.164	55.8	290	340.3	NACA0012	0.25	0.25	no grid	PS	
133	3	1935	0.00	0.00	0.207	71.3	297	344.4	NACA0012	0.25	0.25	no grid	PS	
133	3	1936	4.53	2.00	0.207	71.3	297	344.6	NACA0012	0.25	0.25	no grid	PS	
133	3	1937	9.06	4.00	0.207	71.5	297	345.2	NACA0012	0.25	0.25	no grid	PS	
133	3	1938	11.99	5.29	0.207	71.5	298	345.5	NACA0012	0.25	0.25	no grid	PS	
133	3	1939	16.54	7.30	0.208	71.7	298	344.6	NACA0012	0.25	0.25	no grid	PS	
134	1	1942	0.00	0.00	0.117	39.6	287	338.4	NACA0012	0	0	no grid	PS	
134	1	1943	4.53	2.00	0.117	39.6	286	338.1	NACA0012	0	0	no grid	PS	
134	1	1944	9.05	4.00	0.117	39.6	286	338.2	NACA0012	0	0	no grid	PS	
134	1	1945	12.00	5.30	0.117	39.6	286	338.2	NACA0012	0	0	no grid	PS	
134	1	1946	16.54	7.30	0.117	39.6	286	338.8	NACA0012	0	0	no grid	PS	
134	2	1947	0.00	0.00	0.163	55.5	290	340.6	NACA0012	0	0	no grid	PS	
134	2	1948	4.53	2.00	0.163	55.5	290	340.5	NACA0012	0	0	no grid	PS	
134	2	1949	9.05	4.00	0.163	55.6	290	340.8	NACA0012	0	0	no grid	PS	
134	2	1950	11.99	5.29	0.163	55.6	290	341.0	NACA0012	0	0	no grid	PS	
134	2	1951	16.54	7.30	0.163	55.7	290	341.5	NACA0012	0	0	no grid	PS	
134	3	1952	0.00	0.00	0.207	71.3	297	344.4	NACA0012	0	0	no grid	PS	
134	3	1953	4.53	2.00	0.207	71.4	297	344.9	NACA0012	0	0	no grid	PS	
134	3	1954	9.06	4.00	0.207	71.5	298	345.2	NACA0012	0	0	no grid	PS	
134	3	1955	12.00	5.30	0.207	71.5	298	345.6	NACA0012	0	0	no grid	PS	
134	3	1956	16.54	7.30	0.208	71.7	298	344.7	NACA0012	0	0	no grid	PS	
151	1	2004	0.00	0.00	0.095	32.0	282	337.2	background	0	0	no grid	PS	
151	1	2005	0.00	0.00	0.118	39.7	283	336.5	background	0	0	no grid	PS	
151	1	2006	0.00	0.00	0.142	48.0	284	337.7	background	0	0	no grid	PS	
151	1	2007	0.00	0.00	0.164	55.7	286	339.5	background	0	0	no grid	PS	
151	1	2008	0.00	0.00	0.189	64.0	288	338.7	background	0	0	no grid	PS	
151	1	2009	0.00	0.00	0.209	71.3	291	341.3	background	0	0	no grid	PS	
152	1	2012	0.00	0.00	0.188	64.0	289	340.6	background	0	0	grid	PS	

# REPORT DOCUMENTATION PAGE

*Form Approved*  
OMB No. 0704-0188

The public reporting burden for this collection of information is estimated to average 1 hour per response, including the time for reviewing instructions, searching existing data sources, gathering and maintaining the data needed, and completing and reviewing the collection of information. Send comments regarding this burden estimate or any other aspect of this collection of information, including suggestions for reducing the burden, to Department of Defense, Executive Services and Communications Directorate (0704-0188). Respondents should be aware that notwithstanding any other provision of law, no person shall be subject to any penalty for failing to comply with a collection of information if it does not display a currently valid OMB control number.

**PLEASE DO NOT RETURN YOUR FORM TO THE ABOVE ORGANIZATION.**

<b>1. REPORT DATE (DD-MM-YYYY)</b> May 2004		<b>2. REPORT TYPE</b> Subcontract Report		<b>3. DATES COVERED (From - To)</b> August 2002--March 2004	
<b>4. TITLE AND SUBTITLE</b> Wind Tunnel Aeroacoustic Tests of Six Airfoils for Use on Small Wind Turbines; Period of Performance: August 23, 2002 through March 31, 2004			<b>5a. CONTRACT NUMBER</b> DE-AC36-99-GO10337		
			<b>5b. GRANT NUMBER</b>		
			<b>5c. PROGRAM ELEMENT NUMBER</b>		
<b>6. AUTHOR(S)</b> Stefan Oerlemans			<b>5d. PROJECT NUMBER</b> NREL/SR-500-35339		
			<b>5e. TASK NUMBER</b> WER43104		
			<b>5f. WORK UNIT NUMBER</b>		
<b>7. PERFORMING ORGANIZATION NAME(S) AND ADDRESS(ES)</b> Nationaal Lucht-en Ruimtevaartlaboratorium National Aerospace Laboratory NLR Emmeloord The Netherlands				<b>8. PERFORMING ORGANIZATION REPORT NUMBER</b> AAM-2-32237-01	
<b>9. SPONSORING/MONITORING AGENCY NAME(S) AND ADDRESS(ES)</b> National Renewable Energy Laboratory 1617 Cole Blvd. Golden, CO 80401-3393				<b>10. SPONSOR/MONITOR'S ACRONYM(S)</b> NREL	
				<b>11. SPONSORING/MONITORING AGENCY REPORT NUMBER</b> NREL/SR-500-35339	
<b>12. DISTRIBUTION AVAILABILITY STATEMENT</b> National Technical Information Service U.S. Department of Commerce 5285 Port Royal Road Springfield, VA 22161					
<b>13. SUPPLEMENTARY NOTES</b> NREL Technical Monitor: P. Migliore					
<b>14. ABSTRACT (Maximum 200 Words)</b> The U.S. Department of Energy, working through the National Renewable Energy Laboratory, is engaged in a comprehensive research effort to improve our understanding of wind turbine aeroacoustics. Quiet wind turbines are an inducement to widespread deployment, so the goal of NREL's aeroacoustic research is to develop tools that the U.S. wind industry can use in developing and deploying highly efficient, quiet wind turbines at low wind speed sites. NREL's National Wind Technology Center is implementing a multifaceted approach that includes wind tunnel tests, field tests, and theoretical analyses in direct support of low wind speed turbine development by its industry partners. To that end, wind tunnel aerodynamic tests and aeroacoustic tests have been performed on six airfoils that are candidates for use on small wind turbines. Results are documented in this report.					
<b>15. SUBJECT TERMS</b> wind turbine aeroacoustics; small wind turbine; aeroacoustic tests; wind energy					
<b>16. SECURITY CLASSIFICATION OF:</b>			<b>17. LIMITATION OF ABSTRACT</b> UL	<b>18. NUMBER OF PAGES</b>	<b>19a. NAME OF RESPONSIBLE PERSON</b>
<b>a. REPORT</b> Unclassified	<b>b. ABSTRACT</b> Unclassified	<b>c. THIS PAGE</b> Unclassified			<b>19b. TELEPHONE NUMBER (Include area code)</b>